Intermediate states in bivalent ion induced shrinking of polyacrylate coils on surfaces and in solution

D I S S E R T A T I O N

zur Erlangung des akademischen Grades

Doktor rerum naturalium

(Dr. rer. nat.)

vorgelegt

am Fachbereich Chemie

der Fakultät Mathematik und Naturwissenschaften

der Technischen Universität Dresden

von

Prashant Sinha

geboren am 14.09.1978 in Lucknow, Indien

Gutachter: Prof. Dr. M. Stamm

Prof. Dr. K.-F. Arndt

Eingereicht am: 20.05.2009

Tag der Verteidigung: 09.07.2009

Acknowledgements

I would like to express my deepest gratitude to Prof. Dr. Manfred Stamm for accepting to guide me during the course of this work. His vast experience and knowledge was something I always banked upon. His invaluable suggestions gave my work a direction which has reached fruition with this thesis report.

It is difficult to overstate my gratefulness to my thesis advisor, Dr. Anton Kiriy. I will always remember our adjacent offices separated by a single door which was never closed. Many a new ideas came up here and were diligently followed up.

I have been lucky to be a part of a collaborative effort involving working groups from Dresden, Paderborn and Düsseldorf. All my meetings, email exchanges and telephonic conversations with Prof. Dr. Klaus Huber (Paderborn), Prof. Dr. Hartmut Löwen (Düsseldorf) and Dr. Rene Messina (Düsseldorf) were very helpful in both professional and personal ways. I also would like to thank Prof. Dr. Peter Müller-Buschbaum (München) for his ideas regarding a new image processing protocol I was trying to develop.

I met Sebastian during scattering experiments at Paderborn and on a number of other occasions. He was my expert when it came to scattering techniques. We remain excellent friends. I also thank Dr. Ralf Schweins (Grenoble), whom I met through Sebastian, for sharing with me his expertise in the field of scattering. I remember vividly the week when me and Sebastian were joined by Dr. Ralf Schweins and Dr. Günter Goerigk (Hamburg) to help us conduct (A)SAXS experiments at HASYLAB/DESY, Hamburg. The long beam times gave us an opportunity to come up with really fruitful discussions which helped me improve my understanding of scattering techniques.

and Jagdeep have since shifted to Michigan, München, Leipzig and Zurich respectively. I will always treasure the time I spent with them.

Most importantly, I wish to thank my parents. They bore me, raised me, supported me, taught me and loved me. They even flew to Europe all the way from India to see for themselves that their son was really happy !!

I have no words to thank my wife, Anjali. She is my best friend and without her, this work could not have been accomplished. Together, we helped each other throughout our stay in Dresden. While I was writing this manuscript, she told me that she was pregnant with our first child. I thank her for never complaining despite the fact that I was not able to give her much time. I am indebted to her for being patient with me and for understanding me, as always. To her and our would be child, I dedicate this thesis.

Abstract

Specifically binding ions induce the transition of anionic polyacrylate coils from extended conformation to collapsed globules passing through a cascade of intermediate states when solution conditions approach the L-type precipitation threshold. It is the conformation of these intermediate states on surfaces and in solution which is at the focus of this thesis. In comparing the surface and solution conformations of intermediate states, we were able to qualitatively and quantitatively underline the effects of sample history. Two types of quantitative comparisons have been emphasized. In real space, the radius of gyration values of adsorbed molecules have been evaluated incorporating fully the x, y and z axes. These values have been compared with radius of gyration values of the very same sample solution obtained using SLS. In reciprocal space, a novel image processing protocol has been used to generate the 2D form factor curve wherein the correlation maxima have been compared with corresponding maxima obtained for the very same sample solution using small angle scattering techniques like the SANS.

The influence of bivalent ions, respectively, Strontium, Lead and Calcium, on the shape of polyacrylate coils is studied. In the last case, temperature has been introduced as a secondary parameter to shed further light on the mechanism by which polyelectrolyte-bivalent ion complexation takes place. Both scattering and AFM experiments reveal formation of necklace-like structures as intermediates for NaPA-Sr^{2+} system. Since the mol. wt. of the NaPA coils used was relatively large in this case, adsorption on mica surfaces was strong. Under such conditions, the molecules undergo a z collapse upon flux drying but do not get altered in x and y directions. The ratio R_g(AFM)/R_g(SLS) was found to be in the range 0.7-0.9. The remaining (insignificant) differences in the R_g

Abstract
_____

values arise due to the fact that AFM gives the square root of number averaged mean squared radius of gyration while SLS gives the square root of z-averaged mean squared radius of gyration. The differences in radius of gyration values observed in solution and on surfaces were more prominent for NaPA-Pb^{2+} system. Again, although both scattering and AFM reveal necklace-like structures as intermediates, the ratio R_g(AFM)/R_g(SLS) was now found to be nearly 0.6. The fact that R_g(AFM) is the square root of number averaged and R_g(SLS) is the square root of z-averaged mean squared radius of gyration, alone cannot explain this low value. Since the mol. wt. of NaPA coils used in this case was quite low, adsorption on mica surfaces was weak. Under such conditions, the molecule does not only undergo a z collapse upon flux drying, but also shrinks in the x and y directions due to capillary forces. Finally, with NaPA-Ca^{2+} system, the picture did not show a one-to-one correspondence between solution and surface conformations at all. In fact, it showed a one-step-ahead correspondence. As already stated, the coil to globule transition was induced by increasing the equilibration temperature from 15°C to 30°C in this case. SANS could not identify any necklace-like intermediates in solution at the equilibration temperature of 15°C while AFM scans at this temperature showed the beginning of formation of pearls. Likewise, at the equilibration temperature of 30°C, SANS could identify necklace-like intermediates in solution with a large majority of dumbbells while AFM scans at this temperature showed a mix of dumbbells, sausage-like structures and globules. Indeed, we were witnessing an accelerated coil to globule transition on surfaces as compared to the situation in solution resulting in a pre-emption in the formation of intermediate states on surfaces. Since the ratio R_g(AFM)/R_g(SLS) (given the square root of number averaged and the square root of z-averaged mean

squared values respectively) at the equilibration temperature of 30°C showed a range of 0.7-0.9 indicating strong adsorption of the relatively high mol. wt. NaPA coil on mica surfaces, our suspect were the substrate-sample interaction forces. The AFM scans were therefore analysed with 2D form factor curves, a better protocol when no assumptions about the shape of adsorbed molecules are made a priori, to trace the effects of sample history.

The thesis establishes the general utility of AFM to capture the essential features of a collapsing coil which the very coil exhibits in solution. The shape of the coil on surface and in solution may not be exactly the same, yet reveal the same characteristics. The comparative advantages and disadvantages of salt pre-treated mica surfaces and chemically modified mica surfaces have been brought out. Finally, a definitive new insight is gained as regards the mechanism of coil collapse induced by specifically binding ions. The entropic nature of the process as well as the visualized shape of the collapsing intermediates does not support a mechanism along an electrostatically driven shrinking with linear, rod-like arrays of pearls as intermediates. On a molecular level, it is the liberation of water molecules and Na^+ ions which promotes binding of bivalent ions to COO^- residues. This binding in turn increases the hydrophobicity of the polyacrylate chains. As a consequence, the chains shrink due to an increased propensity for polymer-polymer contacts (and finally precipitate).

Contents

Contents

Contents

Contents

Contents

Introduction

Less than a century ago, mankind could not comprehend stringing monomers together into a polymer chain. Then one day, Hermann Staudinger changed the way we see things around us by coming up with a revolutionary discovery which has inspired generations of polymer physicists and chemists ever since. We will meet many of our heroes, just as Staudinger remains to us, in the next Chapter but let us sit back for a moment and try to figure out why are polymers so interesting anyway.

Is it not remarkable that nature chose strings rather than cubes or spheres to express herself !! Proteins which give us and the living world its physicality are polymers. The genetic code is encrypted inside a polymer (more appropriately known as the DNA). The food we eat and the polysaccharides it contains are polymers. Polymers are everywhere. In the past one century, we have come a long way. Along that way, we have been smart enough to take our clues from nature. So, we decided to synthesize some of our own gigantic molecules from smaller repeat units. The clothes we wear, the drugs we consume, the shelters we live in, the entire material environment around us- all contain polymers.

The very fact that polymers are omnipresent is itself presenting a huge challenge to us in terms of what directions we would like to take. Too many choices !! The choice one makes is personal but it is always interesting to read what others opine about their own choices in this wonderful world of polymer science.

Pondering over the marvels of nature, it is always fascinating to see the kind of superb control natural processes exhibit, right upto the very last detail. For example, as the reader goes through this paragraph, his/her eyeballs are moving from one corner to another without one single error. The control was equally precise when this paragraph was first put down. At that time, the writer's muscles constantly contracted and

expanded with absolute precision. Delicate dynamics of control necessitate realization of wild conformational changes at the molecular level without a loss of topological integrity. Perhaps that is the reason why nature chose polymers as her theater because which other candidate, but polymers, could accomplish this. But how do polymers change shape that quickly and that perfectly? It would be heart breaking to imagine a child taking a week to exhibit a smile, or worse still, the mother taking another month to respond to it. That is where nature must have decided to create charged polymers (somebody called them polyelectrolytes and we will go along with this term in the rest of the thesis) so that swarms of ions would crowd around these polyelectrolyte molecules and make them far more responsive than they ever would be had they been left alone.

In this humble effort, we have tried to pursue the response of one such polyelectrolyte, one with a fairly simple backbone, towards bivalent ions. The polyelectrolyte was the charged analogue of polyacrylic acid which looks like
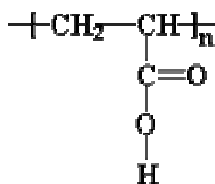
It becomes charged, for example, when dissolved in water due to the loss of H^+ ions and is then called a polyacrylate to underscore its charged status. The physics and chemistry of polyelectrolytes (including, but not limited to, polyacrylates) interacting with bivalent ions is not understood well depite the fact that such an understanding is central to biosciences and nanosciences, both of which are sometimes euphemistically called the "new sciences". As important as the identification of the problem might be, the real challenge is to know what to do with this identification. In other words, how to approach the identified problem in search of a solution?

The approach proposed and followed here is at the level of single molecules, i.e., trying to quantize the response of single polyacrylate molecules towards bivalent ions. The obvious question then is- why single molecules, why not ensembles? Well, the short answer would be that it's a new approach, a new way of thinking, a new philosophy which preaches (rather justifiably) to understand things from downside up, starting from the basic blocks to larger complicated assemblies. Single molecule studies are currently providing a new window into biology and material science. We could not have asked for a better time to follow this approach than today. At no point in history was instrumentation so developed that one could "see" single molecules and play around with them. To understand how single molecules behave in the nearby environment will enhance our grasp of complicated assemblies of molecules which await us out there.

But what kind of "nearby environments" are we really talking about here? Of course, such charged giants cannot stand alone lest they discharge and fall down. They need a suitable environment to showcase their wonders. Two kinds of environments immediately come to mind, solutions and interfaces, in an apparent analogy with nature (again). The problem now begins to further complicate. Not only are the interactions of polyelectrolyte molecules with bivalent ions little understood, the environments in which such interactions take place and how such an environment itself affects the shape of the polyelectrolyte molecules remains an intensely debated area of research.

In a first, this work tries to characterize in solution the shape of single polyacrylate coils which have formed complex bonds with bivalent ions and then "visualize" and quantize the shape of very same coils on surfaces. The reward of following such an approach would be a definite answer to the following questions- Given our current

instrumentation capacity, is such an approach possible? If yes, how much do the shape

of single polyacrylate coils on surfaces reflect the shape of the very same coils in

solution? Can the differences be accounted for in terms of substrate-sample

interactions (polyelectrolyte molecules interacting with the very surface on which

they are adsorbed and imaged)? What is the mechanism by which polyacrylate coils

change their shape while complexing with bivalent ions? We will answer these

questions (and others) as we move along.

The rest of the thesis is organized as follows.

Chapter 2 discusses the theoretical background for the work. It comments upon the

theories developed for both solution behaviour and surface behaviour of

polyelectrolytes and the various parameters which influence their shape. The phase

diagrams of polyacrylic acid are taken up separately (we shall see why they are

relevant). Simulation snapshots have been included wherever available to emphasize

the extent upto which mathematical models explain experimental observations. In

each sub section, there is a write up titled "General comments". These serve an

important purpose in the sense that it is here where the reader can find out how and to

what extent, these theories/simulations apply to the experimental work performed in

this thesis.

Chapter 3 explains the experimental procedures followed while trying to adsorb single

molecules on surfaces. This Chapter also includes the list of materials used.

Chapters 4, 5 and 6 form the results and discussion part of the thesis. The influence of

bivalent ions, respectively, Strontium, Lead and Calcium, on the shape of polyacrylate

coils is studied. In the last Chapter, temperature has been introduced as a secondary

parameter to shed further light on the mechanism by which polyelectrolyte-bivalent

ion complexation takes place. Each Chapter begins by posing a few questions which

had hitherto remained unanswered and the remaining discussion revolves around those questions.

Finally, Chapter 7 provides a summary of the work and an outlook.

A (seemingly) long list of appendices is provided for the interested reader. Appendix A introduces the research techniques used in this work, but not without touching first upon the necessity of using the combined power of both scattering and microscopy. To characterize/probe the shape of single molecules in solution, Static Light Scattering, (Anomalous) Small Angle X-ray Scattering and Small Angle Neutron Scattering were used. Atomic Force Microscopy was used for investigation of single adsorbed molecules on surfaces. The image processing protocols have been discussed. Appendix B provides the MATLAB (our tool of choice) code used for the evaluation of radii of gyration of adsorbed molecules. Appendix C contains some representative AFM scans of polyacrylates as well as polystyrene sulfonates. The latter results were obtained on the side, so to say, but interesting as they were, we decided to go on record by quoting them here.

It is hoped that the thesis presents an interesting reading.

Theoretical background

2.1 Shape of polyelectrolytes in aqueous solutions

In 1938 and 1939, W. Kern,[1-3] a student of Herman Staudinger (whose work "über Polymerization" in 1920 laid the very foundation of polymer science) published a series of articles dealing with solution behavior of polyacrylic acid during its neutralization. They could observe a sharp increase in solution viscosity and a decrease in the ionization constant of the carboxyl groups as the neutralization of polyacrylic acid was increased. In 1948, Kuhn et al.[4-5] began trying to place this behavior of polyelectrolytes on a theoretical basis. On empirical grounds, they predicted the expansion of a randomly coiled molecule as the charge density on it was increased, owing to intramolecular electrostatic forces of repulsion. This explained the increase in viscosity observed by Kern and Staudinger. The decrease in ionization constant of the carboxyl groups could be rationalized by the increasing difficulty in the removal of a H^+ ion from a chain which was getting progressively charged. Further, Kuhn and coworkers rather erroneously assumed that in sufficiently dilute solutions, all counterions could eventually be completely removed from the polyion resulting in a rigid rod like structure. It was later found out that even for a highly extended chain, there will always be some counterions in close proximity to the chain. This could be shown[6-7] by approximating the rigid rod postulation of Kuhn and coworkers to a charged thin cylinder and then obtaining the distribution of electrostatic potential (and hence the distribution of counterions) by solving the Poisson-Boltzmann equation for cylindrical symmetry.

2.1.1 Poisson-Boltzmann equation and its solution for cylindrical symmetry

Consider a charged thin cylinder (representing the polyion) of radius a. Its axis lies along

the axis of a bigger cylinder of radius R which contains all the counterions associated with the polyion. Assume that both the polyion and the cylindrical shell are very long so that end effects can be neglected.

Poisson's equation relates the electrostatic potential $\psi(r)$ of a counterion at a distance r ($a \leq r \leq R$) from the axis of the polyion, to the local space charge density $\rho(r)$ at the same distance via a mean field. It can be written as follows

$$\Delta \psi(r) = -\frac{\rho(r)}{D\varepsilon_0} \qquad (2.1)$$

In eq. 2.1, D is the dielectric constant of the medium (assumed to be continuous) and ε_0, the permittivity of free space. The Laplacian operator in cylindrical space (corresponding to the cylindrical field of counterions constituting the local space charge) is given by Δ where

$$\Delta = \frac{1}{r}\frac{d}{dr}\left[r\frac{d}{dr} \right] \qquad (2.2)$$

If we assume that $\rho(r)$ is governed by the Boltzmann distribution function, then

$$\rho(r) = \rho_0 \exp\left[\frac{e\psi(r)}{kT} \right] \qquad (2.3)$$

In eq. 2.3, k is the well known Boltzmann constant, T is the absolute temperature and e is the electronic charge (we have restricted ourselves to monovalent charges). Further, in writing eq. 2.3, we have assumed the boundary condition that at an infinite distance from the polyion, $\psi(r)$ tends to zero and $\rho(r)$ tends to ρ_0, the space charge density of the bulk. Thus,

$$\rho_0 = -c_0\alpha e \qquad (2.4)$$

where c_0 is the bulk concentration of solution and α is the degree of ionization of the

polyion.

Combining eqs. 2.1-2.4, we get the Poisson-Boltzmann equation for cylindrical symmetry in absence of any added salt.

$$\frac{1}{r}\frac{d}{dr}\left[r\frac{d\psi(r)}{dr}\right]=\left(\frac{1}{D\varepsilon_0}\right)c_0\alpha e\exp\left(\frac{e\psi(r)}{kT}\right)$$

(2.5)

Fortunately, eq. 2.5 can be exactly solved (In fact, it turns out that the Poisson-Boltzmann equation can be exactly solved only for two cases- charged planar surface in the presence of added salts[8-9] and charged thin cylinder in the absence of an added salt.[6-7] The latter case belongs to us). Eq. 2.5 has solution of the form

$$\psi(r)=\frac{1}{B}\left[\ln\left(\frac{2\delta^2}{AB}\right)-2\ln r-2\ln\left[\cos\delta(\ln r+\beta)\right]\right]$$

(2.6)

In eq. 2.6, $A=\frac{1}{D\varepsilon_0}(c_0\alpha e), B=\frac{e}{kT}$ and β, δ are the two constants of integration. The constants of integration can be evaluated from the following two boundary conditions. First, the total charge on all the counterions is equal in magnitude and opposite in sign to the charge on the polyion, i.e.,

$$-\frac{\alpha e}{b}=\int_a^R 2\pi\rho(r)dr$$

(2.7a)

where b is the monomer size.

Second, the electrostatic potential vanishes at the boundary of the cylindrical shell enclosing the counterions of a given polyion due to the time-average cylindrical symmetry of neighboring polyions and their counterions, i.e.,

$$\left(\frac{d\psi(r)}{dr}\right)_{r=R}=0$$

(2.7b)

The integrated numerical solutions of the Poisson-Boltzmann equation for cylindrical symmetry applied to different solution concentrations of half neutralized polyacrylic acid are reproduced in fig. 2.1.
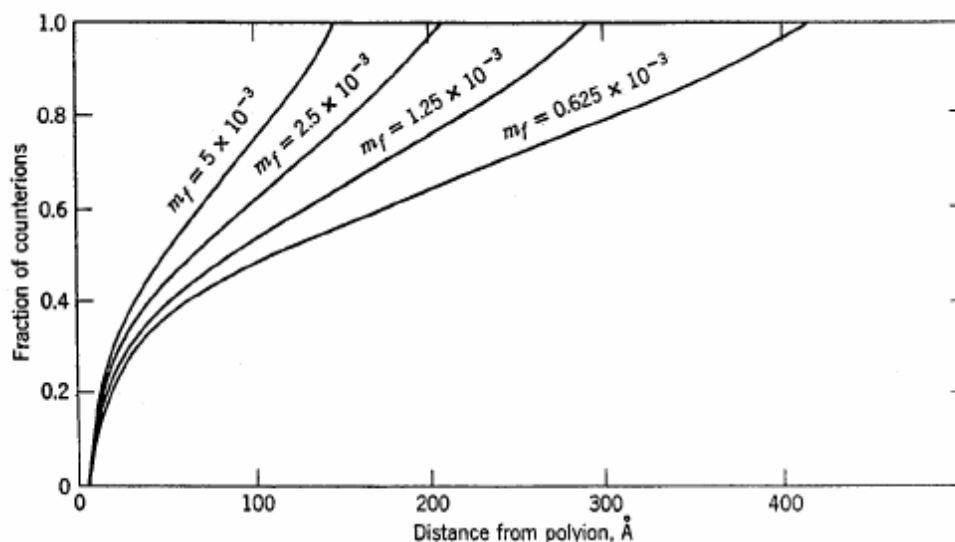
Figure 2.1: Distribution of counterions around a rigid rod like polyacrylic acid molecule carrying a linear charge density of 0.5/nm. Results are shown for different solution concentrations (m_f is in moles/liter). (adopted from ref. [6])

It can be seen that even at fairly high dilutions, a good fraction of counterions are in close proximity to the polyion. This was a significant finding in itself despite the fact that no extra salt addition was considered.

The search for a reason to account for this finding brings us to a phenomenon called "counterion condensation" (justifiably attributed to Imai, Onishi and Oosawa[10-12]). The latter authors in a series of publications propounded the idea that a system formed by a charged rigid rod and its counterions cannot sustain an electrostatic potential, ψ greater than $\dfrac{kT}{e}$ so that at a higher charge density of the rigid rod, some counterions have to

condense back onto the polyion. Sometime later, MacGillivray et al.[13] picked up the problem of solving cylindrically symmetric Poisson-Boltzmann equation for an environment which contained a small quantity of an added monovalent salt. At this point, the phrase "small quantity" should be understood to mean an amount of salt which does not change the very rigid rod like shape of the molecule. Surprisingly (and we shall shortly see why is it surprising), MacGillivray and coworkers found out that a solution of the linearized equation is a good approximation to the solution of the complete equation for all values of electrostatic potential, $\psi < \dfrac{kT}{e}$. The linearization reduces the cylindrically symmetric Poisson-Boltzmann equation derived for an environment containing small quantity of an added monovalent salt, to the famous Debye-Hückel equation.

2.1.2 Debye-Hückel approximation

A widely accepted theory describing the behavior of simple electrolytes in dilute solutions is the Debye-Hückel theory.[14] It however cannot be unambiguously applied to dilute solutions of polyelectrolytes primarily because of two limitations. One, the Debye-Hückel theory treats the test ion in a spherically symmetric cloud of counterions. This is almost never the case with polyelectrolytes. If the rigid rod postulation of Kuhn and coworkers, as described above, is followed, polyelectrolytes, in sufficiently dilute solutions, can be approximated to be charged thin cylinders. The counterions too will then be in a cylindrical space. Two, the Debye-Hückel theory assumes that the electrostatic potential energy of the test ion is much smaller than its thermal energy, *kT*. This assumption is also never valid in a polyelectrolyte solution, even at lowest experimentally measurable solution concentrations. The presence of high charge density

on a polyelectrolyte would imply high concentration of counterions in small volumes. Thus, the electrostatic potential energy of a counterion in the vicinity of such a multiple charge is always many times greater than its thermal energy. Given these limitations, MacGillivray's findings were considered surprising at first.

We begin from the same basic mean field Poisson's equation for cylindrical symmetry, the eqs. 2.1 and 2.2, as cited above. The Boltzmann distribution assumed in eq. 2.3 now has to be written for both positive and negative monovalent ions belonging to the added salt. Thus, we have the following equations.

$$\Delta \psi(r) = -\frac{\rho(r)}{D\varepsilon_0} \tag{2.8}$$

$$\Delta = \frac{1}{r}\frac{d}{dr}\left[r\frac{d}{dr}\right] \tag{2.9}$$

$$\rho(r) = \rho^+(r) + \rho^-(r) = \rho_0 \exp\left(\frac{e\psi(r)}{kT}\right) - \rho_0 \exp\left(-\frac{e\psi(r)}{kT}\right) = 2\rho_0 \sinh\left(\frac{e\psi(r)}{kT}\right) \tag{2.10}$$

Here, ρ_0 is the space charge density of the bulk and is related to the bulk concentration of added monovalent salt, c_0 as

$$\rho_0 = -c_0 e \tag{2.11}$$

Combining eqs. 2.8-2.11, we get the Poisson-Boltzmann equation for cylindrical symmetry in the presence of an added monovalent salt.

$$\frac{1}{r}\frac{d}{dr}\left(r\frac{d\psi(r)}{dr}\right) = \left(\frac{1}{D\varepsilon_0}\right) 2c_0 e \sinh\left(\frac{e\psi(r)}{kT}\right) \tag{2.12}$$

A student of research level mathematics would immediately identify eq. 2.12 as a "singular perturbation problem". This is to say that any asymptotic expansion of the solution is not uniformly valid for all values of r from the surface of charged thin cylinder

to infinity. The principles used to solve such equations were developed by Kaplun, Lagerstrom and Erdelyi.[15-19] What is remarkable however is that the solution of the complete equation (not given in this thesis) is approximately the same as solution of the linearized equation in the limit $\psi < \dfrac{kT}{e}$.

When $\psi < \dfrac{kT}{e}$, eq. 2.12 can be linearized using Taylor expansion.

$$\frac{1}{r}\frac{d}{dr}\left(r\frac{d\psi(r)}{dr}\right)=\left(\frac{1}{D\varepsilon_0}\right)2c_0 e\sum_{n=0}^{\infty}\left(\frac{e\psi(r)}{kT}\right)^{2n+1}/(2n+1)! \tag{2.13}$$

Again since $\psi < \dfrac{kT}{e}$, only $n = 0$ term is included and the remaining terms, considered negligible, are ignored. This reduces eq. 2.13 to

$$\frac{1}{r}\frac{d}{dr}\left(r\frac{d\psi(r)}{dr}\right)=\left(\frac{1}{D\varepsilon_0}\right)2c_0 e\left(\frac{e\psi(r)}{kT}\right) \tag{2.14}$$

On rearranging eq. 2.14, we get

$$\frac{1}{r}\frac{d}{dr}\left(r\frac{d\psi(r)}{dr}\right)=\left(\frac{2c_0 e^2}{D\varepsilon_0 kT}\right)\psi(r)$$

$$=\kappa^2\psi(r) \tag{2.15}$$

where $\lambda_D = \kappa^{-1} = \left(\dfrac{D\varepsilon_0 kT}{2c_0 e^2}\right)^{1/2}$ is called the Debye screening length and is the characteristic decay length of the potential.

Eq. 2.15 is the famous Debye-Hückel equation.

The above findings led Manning[20] to give his "limiting laws" where he treated the counterions present in a polyelectrolyte solution as either uncondensed (or "mobile") if

their potential was less than $\dfrac{kT}{e}$ or condensed if their potential was greater than $\dfrac{kT}{e}$. The

uncondensed ions were treated in the Debye-Hückel approximation. Manning's limiting

laws apply to both salt free solutions of polyelectrolytes as well as to those containing a

small quantity of an added monovalent salt.

2.1.3 Manning's threshold for counterion condensation

The critical nature of the point $\psi = \dfrac{kT}{e}$ was noted by many authors[7,10-13,21-22] right since

the time theoretical investigations began into the behavior of polyelectrolytes in aqueous

solutions. However, a statistical mechanical interpretation from a very fundamental point

of view has to be credited to Manning and Onsager. The latter had observed that the

statistical mechanical phase integral for an infinite line charge model diverges for all

values of line charge density greater than a critical value. This was verified by Manning

as follows.

Consider a polyelectrolyte modeled as an infinite line charge (so that end effects can be

ignored) with line charge density β. If the polyelectrolyte chain bears charged groups of

valence Z_p separated by a distance b (the monomer size), then

$$\beta = \frac{Z_p e}{b} \tag{2.16}$$

where e is the electronic charge.

If r denotes the distance of an uncondensed or mobile ion of valence Z_i from the infinite

line charge, then for sufficiently small values of r (say $r \leq r_0$), the electrostatic energy,

$u_{ip}(r)$ of such a mobile ion is given by the unscreened Coulomb interaction as

$$u_{ip}(r) = -Z_i e \left(\frac{2\beta}{D\varepsilon_0} \right) \ln(r), \, r \leq r_0 \tag{2.17}$$

where D is the dielectric constant of the medium (assumed to be continuous) and ε_0 is the permittivity of free space.

The contribution $A_i(r_0)$ to the phase integral of the region in which the mobile ion i is within a distance r_0 of the infinite line charge, while all other mobile ions are at a distance greater than r_0 thereby contributing a finite factor $f(r_0)$, is given by

$$A_i\left(r_0\right) = f\left(r_0\right)\int_{0}^{r_0} \exp\left(-\frac{u_{ip}\left(r\right)}{kT}\right) 2\pi r\, dr \tag{2.18}$$

where k is the Boltzmann constant and T, the absolute temperature.

Combining eqs. 2.16-2.18, we get

$$A_i\left(r_0\right) = 2\pi f\left(r_0\right)\int_{0}^{r_0} r^{\left(1+2Z_iZ_p\Phi\right)}\, dr \tag{2.19}$$

where

$$\Phi = \frac{e^2}{D\varepsilon_0 kTb} \tag{2.20}$$

It can be seen that if i is a counterion so that $Z_iZ_p < 0$, the integral in eq. 2.19 diverges for all $\Phi \geq \mid Z_iZ_p \mid^{-1}$. If attention is restricted to monovalent charged groups and mobile ions, the limiting condition may be expressed as $\Phi \geq 1$. The condition is known as Manning's threshold and Φ as Manning's charge density parameter.

For dilute solutions of polyelectrolytes with or without a small quantity of an added monovalent salt, if the value of charge density parameter is greater than one, then sufficiently many counterions will condense on the polyion to lower the charge density parameter to the value one. If however the value of charge density parameter is less than one, no condensation takes place and the ions may be treated in the Debye-Hückel

approximation. As we shall see in section 2.3.6, the previous statement is of immense importance to a polymer chemist/physicist. Manning went on to derive formulas for colligative properties of polyelectrolyte solutions based upon this approach.

Meanwhile, we would like to draw the attention of the reader to a striking similarity of eq. 2.20 with the classical statistical thermodynamics of simple electrolyte solutions. It will be recognized that the quantity $\dfrac{e^2}{D\varepsilon_0 kT}$ is the Bjerrum length, the separation at which electrostatic interaction energy between two elementary charges is equal to the thermal energy scale. Thus,

$$\Phi = \frac{\lambda_B}{b} \tag{2.21}$$

where $\lambda_B = \dfrac{e^2}{D\varepsilon_0 kT}$ is the Bjerrum length.[23]

An underlying assertion in the theory discussed so far is that a polyion in aqueous solution is almost rodlike because of the intramolecular electrostatic repulsions. However, this is not entirely true. There are short wavelength fluctuations at very small length scales and at larger length scales, polyelectrolytes too have a persistence length (just like their uncharged analogues). The first calculations regarding, what henceforth came to be known as the electrostatic persistence length, were performed independently in 1970s by Odijk[24] and Skolnick and Fixman[25] (OSF). The OSF perturbation calculations predicted that the electrostatic persistence length is proportional to the square of Debye screening length resulting indeed in a very high induced stiffness. Their approach was to evaluate the energy required to bend a straight charged chain interacting via screened Coulomb potential (also called Yukawa potential). In 1993 however, Barrat

and Joanny[26] demonstrated that the OSF perturbation approach of bending a straight charged chain was unstable to short wavelength fluctuations. Their result was consistent with de Gennes et al.[27] picture of electrostatic blobs, given long back ago, inside which Coulomb repulsion is not sufficient to deform the chain. If the Debye screening length is much larger than these electrostatic blobs, Coulomb repulsion stretches the chain of these blobs into a straight stiff cylinder.[28] Repeating the OSF bending calculations for this straight stiff cylinder of electrostatic blobs interacting via Yukawa potential, Barrat and Joanny found out that there is no qualitative alteration of the original result, i.e., electrostatic persistence length is still proportional to the square of Debye screening length. However, the situation changes when the polyelectrolyte chain is surrounded by a larger number of ions. This can happen when the polyelectrolyte solution is in a semi dilute regime (distance between chains is of the order of size of chains) or contains added salts. In these cases, there is a much stronger screening of the electrostatic repulsion of charges on the chain resulting in much shorter electrostatic persistence lengths. The electrostatic persistence length is now found to be in direct proportionality to Debye screening length. The electrostatic blob model is still valid but an extra correlation length scale has to be introduced. We shall not discuss the concentrated polyelectrolyte solution case. Suffice it shall be to say that the electrostatic blob model cannot be applied at high concentrations as the screening is then governed by polymeric nature of the polyelectrolyte solution.[29-30]

2.1.4 Electrostatic blob model

Let us consider a dilute salt free polyelectrolyte solution of charged flexible chains with a degree of polymerization, N and monomer size, b. Let f be the fraction of charged

monomers. It incorporates any effect of counterion condensation. In a dilute salt free

solution, each polyelectrolyte molecule can be represented as a chain of electrostatic

blobs as shown in fig. 2.2.
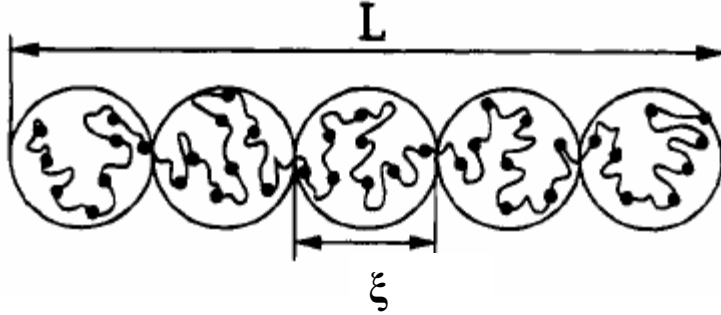
Figure 2.2: Polyelectrolyte chain in a dilute salt free solution. The chain is an extended configuration of electrostatic blobs. L is the extended size of the chain, ξ is the size of an electrostatic blob. Filled circles are charged groups. (adopted from ref. [31])

Let number of monomers inside an electrostatic blob be g so that charges per blob are gf.

The electrostatic interactions among charges contained within an electrostatic blob is

given by $\dfrac{(gf)^2 e^2}{\varepsilon_0 D \xi}$ where e is the electronic charge (we have confined ourselves, as usual,

to monovalencies), ε_0 is the permittivity of free space, D is the dielectric constant of the

solvent (assumed continuous) and ξ is the electrostatic blob size. In a good or θ solvent,

this electrostatic energy is of the order of thermal energy, kT where k is the Boltzmann

constant and T, the absolute temperature.[27-28] In a bad solvent, it is of the order of

polymer-solvent interfacial energy given by $\gamma \xi^2$ where γ is the interfacial tension and is

approximately related to the reduced temperature, $\tau\left(\tau = \dfrac{\theta - T}{\theta}\right)$ as $\gamma \approx \dfrac{\tau^2 kT}{b^2}$.[32] Thus, we

have the following equations for length scales less than the electrostatic blob size.

$$\frac{(gf)^2 e^2}{\varepsilon_0 D \xi} \approx kT, \, T \geq \theta$$

$$\approx \left(\frac{\tau^2 kT}{b^2} \right) \xi^2 , \, T < \theta \tag{2.22}$$

Since the conformation of the polyelectrolyte inside the electrostatic blob is almost unperturbed by the electrostatic interaction and depends upon the quality of the solvent for neutral polymer, the following scaling laws[27,32-33] can be shown to apply

$$\xi \approx b(g/\tau)^{1/3}, \, T < \theta$$

$$\approx bg^{1/2}, \, T = \theta$$

$$\approx bg^{3/5}, \, T \gg \theta \tag{2.23}$$

From eqs. 2.22 and 2.23, we get the electrostatic blob size, ξ as under

$$\xi \approx b(\Phi f^2)^{-1/3} , \, T \leq \theta$$

$$\approx b(\Phi f^2)^{-3/7} , \, T \gg \theta \tag{2.24}$$

where $\Phi = \dfrac{\lambda_B}{b}$, λ_B being the Bjerrum length. We have seen this parameter earlier in eq.

2.21. It is the Manning's charge density parameter.

On length scales larger than the electrostatic blob size, electrostatics dominate and the blobs repel each other to form a fully extended chain of electrostatic blobs of length, L. Again, from eqs. 2.22 and 2.23, it follows that

$$L \approx \xi N/g \approx Nb(\Phi f^2)^{2/3} \tau^{-1}, \, T < \theta$$

$$\approx Nb(\Phi f^2)^{1/3}, \, T = \theta$$

$$\approx Nb(\Phi f^2)^{2/7}, \, T \gg \theta \tag{2.25}$$

Note that in a dilute solution, effect of solvent quality merely changes the electrostatic blob and conformation of the chain is always a rodlike assembly of electrostatic blobs.

The situation however changes, as mentioned earlier, when we consider the semi dilute regime or when the polyelectrolyte solution contains added salts. Consider the semi dilute salt free case first. The major feature in the electrostatic blob model now is the inclusion of a correlation length, r_{corr} as shown in figure 2.3. There are three different length scales to be considered. On a length scale shorter than ξ, thermal energy dominates and conformation is similar to a neutral polymer (collapsed in poor solvent, random walk in θ solvent, self avoiding walk in good solvent). On a length scale between ξ and r_{corr}, electrostatics dominate and chain is a fully extended conformation of electrostatic blobs. Finally, on a length scale larger than r_{corr}, electrostatic interactions are screened and the chain is a random walk of correlation blobs.
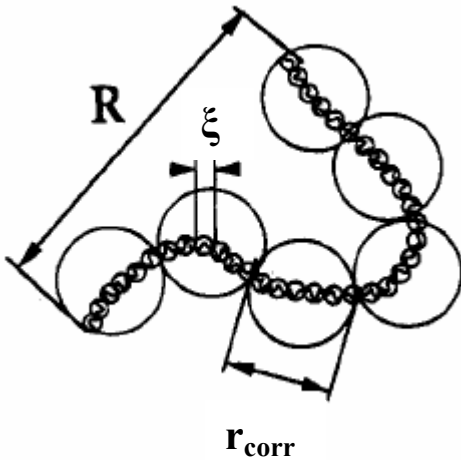
Figure 2.3: Polyelectrolyte chain in semi dilute salt free solution. The chain is a random walk of correlation blobs, each of which is an extended configuration of electrostatic blobs. (adopted from ref. [31])

It can be shown that the following scaling laws[27] apply in the semi dilute salt free case.

$$r_{corr} \approx (B/cb)^{1/2} \tag{2.26}$$

$$g \approx (B/b)^{3/2}c^{-1/2} \quad (g \text{ is the number of monomers in the correlation blob}) \tag{2.27}$$

$$R \approx (b/B)^{1/4}N^{1/2}c^{-1/4} \tag{2.28}$$

where B is the ratio of chain contour length, Nb and extended size, L. It is dependent upon the quality of the solvent and can be extracted from eq. 2.25 as under

$B \approx Nb/L \approx (\Phi f^2)^{-2/3}\tau, \; T < \theta$

$\qquad \approx (\Phi f^2)^{-1/3}, \; T = \theta$

$\qquad \approx (\Phi f^2)^{-2/7}, \; T \gg \theta$ \hfill (2.29)

The quantity B is called the second virial coefficient.

When a small quantity of added monovalent salt is present in a dilute polyelectrolyte solution, the electrostatic persistence length is drastically decreased. There are two interesting cases. When electrostatic persistence length is smaller than distance between two chains but larger than chain size, the situation is analogous to fig. 2.2. On the other hand, if electrostatic persistence length falls below the chain size, we have a picture analogous to fig. 2.3.

Till here, we have assumed, among other things, that the charge distribution along the chain is uniform. Some new non trivial behaviors are theoretically postulated if we change this condition. In fact for a finite partially charged polyelectrolyte chain, the charge distribution can never be uniform.

2.1.5 The role of end effects- Trumpet model

Soon after Manning gave his limiting laws, there was intense activity in the development of theory of polyelectrolytes in aqueous solutions, one very important outcome of which was the recognition of two kinds of polyelectrolytes.[34-35] The charge distribution on a polyelectrolyte chain could either be quenched or annealed. For a quenched polyelectrolyte, the position of charges (ionized sites) along the chain are "frozen". This, for example, is the case with strongly charged polyelectrolytes like polystyrene sulfonate.

On the other hand, for an annealed polyelectrolyte, the position of charges along the chain can move. This is the case with polyacrylic acid (any weak polyacid or polybase for that matter). This means that H^+ ions can freely dissociate and recombine while maintaining the same total number of charges (ionized sites) at a particular pH but nevertheless allowing charges to move along the chain. The question is where will they move to? It has been theoretically established that they would move to the ends of the chain (assuming of course, that there is an end, i.e., the polyelectrolyte chain is finite).

In 1997, Berghold et al.[36] predicted that a finite polyelectrolyte chain in dilute aqueous solution will incur an accumulation of charge at its ends and a slight depletion of charge in its middle. Their model was improved by Castelnovo et al.[37] in the year 2000. The logic behind this predicted end effect is that a charge has lesser neighboring charges at the end of the chain than in its middle. Thus, electrostatic potential energy of a charge is minimized more at the ends. Let us now investigate how can this end effect change the conformation of the chain.

Consider a weakly charged finite chain in a salt free solution. The phrase "weakly charged" is used to make mathematics easier assuming that we are below the Manning threshold. Assume further that a redistribution of charges dictated by minimization of electrostatic potential energy is not allowed and the only way for the molecule to minimize its electrostatic potential energy is to change its conformation. Now, a force balance on each point of the chain along the so called classical path of the polymer (the most probable conformation) can be shown to reduce to

$$\frac{3kT}{b^2}\frac{d^2\mathbf{r}(s)}{ds^2} = -ef\mathbf{E}(s) \tag{2.30}$$

In eq. 2.30, k is the Boltzmann constant, T is the absolute temperature, b is the monomer size, $r(s)$ is the position of charges in space, ds is the infinitesimal distance traversed along the chain, the first derivative $\dfrac{d\mathbf{r}(s)}{ds}$ is the tension along the chain, e is the electronic charge (only monovalencies are considered), f is the fraction of charged monomers and $E(s)$ is the average electric field created by charges of the chain. Eq. 2.30 is valid at every point of the chain except for the end points where the force balance on a section of length ds reads

$$\frac{3kT}{2b^2}\frac{d\mathbf{r}(s)}{ds} = -ef\mathbf{E}(s)ds \tag{2.31}$$

because the chain is only stretched by one side at the end point.

Eq. 2.31 signifies that the tension vanishes on the end point of the chain and we may expect a trumpet like configuration (a chain more stretched in the middle than at the ends) as a result. Henceforth, let us assume a trumpet like configuration and check whether such an assumption leads to self consistent equations coupling the charge distribution and chain conformation. We define our trumpet with a local electrostatic blob size $\xi(z)$ slowly increasing towards the ends of the chain to a final size ξ_M, the parameter z indicating that the chain is spread along the (arbitrarily chosen) z axis. This is shown in fig. 2.4.
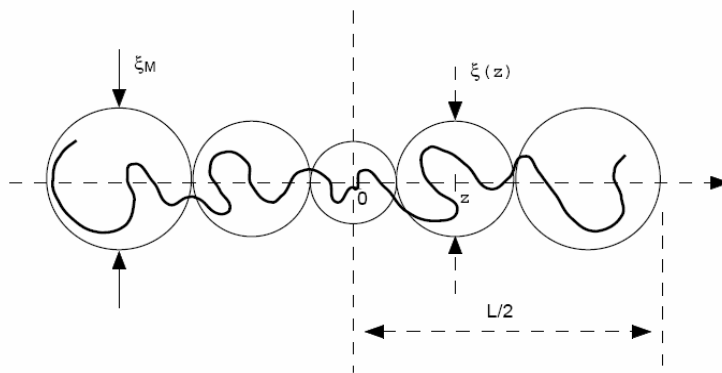
Figure 2.4: Trumpet like configuration: L is the extended length of the chain along the z axis, ξ_M is the maximal blob size, $\xi(z)$ is the size of a local blob centered at z. (adopted from ref. [37])

Since $\xi(z)$ is only slowly varying with z, ξ_M is defined as $\xi_M \equiv \xi(z = L/2 - \xi_M)$ where L is the extended length of the chain along the z axis. It also follows from the definition of electrostatic blobs that the following approximation holds

$$\frac{dz}{ds} \equiv \frac{\xi(z)}{g(z)} = \frac{b^2}{\xi(z)} \tag{2.32}$$

where, as before, $\xi(z)$ is the size of the local electrostatic blob centered at z and $g(z)$, the number of monomers inside the blob.

We have to evaluate the electric field created by the polymer path $r(s)$ in order to get self consistent equations. For evaluating the electric field, we introduce short distance cut-offs to prevent the electric field from diverging. The cut-off length is the size of one electrostatic blob. The electric field is written as a sum over the contributions of all the electrostatic blobs as under

$$E(z) = \frac{f \lambda_B kT}{eb^2} \left[\int_{-L/2}^{z-\xi(z)} \frac{\xi(z_1)}{(z-z_1)^2} dz_1 - \int_{z+\xi(z)}^{L/2} \frac{\xi(z_1)}{(z-z_1)^2} dz_1 \right] \tag{2.33}$$

where λ_B is the Bjerrum length.

In writing eq. 2.33, we have taken the charge contained within one electrostatic blob as

$f\left(\frac{\xi(z)}{b}\right)^2$ (refer eq. 2.23, $T = \theta$ case). Combining eqs. 2.30, 2.32 and 2.33, we can obtain

a simple expression for the blob size.

$$\xi(z) = \frac{\xi_{scaling}}{\left[\ln\left(\frac{(L/2)^2 - z^2}{L\xi_M} \right) + 1 \right]^{1/3}} \tag{2.34}$$

where $\xi_{scaling} = \dfrac{b}{\left[(\lambda_B / b) f^2 \right]^{1/3}}$ is the electrostatic blob size one obtains from scaling

theory (refer eq. 2.24, $T = \theta$ case).

Eq. 2.34 is valid in the range $-\dfrac{L}{2} + \xi_M \leq z \leq \dfrac{L}{2} - \xi_M$.

Finally, we notice that the parameters L and ξ_M can be determined self consistently from

the following equations.

$$Nb^2 = 2 \int_{0}^{L/2 - \xi_M} \xi(z)dz \tag{2.35}$$

where N is the number of monomers carried on the chain and

$$\xi_M = \dfrac{\xi_{scaling}}{\left[\ln \dfrac{L - \xi_M}{L} + 1 \right]^{1/3}} \tag{2.36}$$

Eq. 2.35 ensures the conservation of number of monomers and eq. 2.36 follows from eq.

2.34 from the way maximal blob size has been defined ($\xi_M \equiv \xi(z = L/2 - \xi_M)$).

Hence the main features of a trumpet like configuration can be captured by a set of self

consistent equations. In the derivation above, charges were not allowed to move. Thus,

the only way to minimize the electrostatic potential energy of the molecule was to change

the conformation. With actual annealed polyelectrolytes, we add an extra degree of

freedom and the trumpet effect is less pronounced. Further, upon addition of a small

quantity of monovalent salt, there is a fast decay of charge inhomogeneity along the chain

and the trumpet effect is subdued. Such is the case in solution. But the analysis above

shows that annealed polyelectrolytes might exhibit interesting behaviors where end

effects are known to be important, as for example, adsorption on charged surfaces.

In 2002, Zito and Seidel[38] performed Monte Carlo simulations to study the non uniform equilibrium charge distribution along a single annealed polyelectrolyte chain under θ solvent conditions and with added salt. The simulation results compared well with Castelnovo's prediction. The snapshots are reproduced in fig. 2.5. The end effects are noticeable.

Figure 2.5: Monte Carlo simulation snapshots showing end effect in a partially charged chain ($f = 1/8$) with a fixed degree of polymerization, $N = 1000$ at θ solvent conditions. (a) Less pronounced end effects when Debye screening length, λ_D is of the order of monomer size, b (b) Pronounced end effects when Debye screening length, λ_D is 500 times the monomer size, b (adopted from ref. [38])

2.1.6 General comments

At the time of writing this thesis, no fairly acceptable theory exists which includes specific ion-correlation effects and thermal fluctuations disregarded by the mean field approaches described in sections 2.1.1-2.1.5. The assumption that water acts as a homogenous dielectric medium can be misleading too in the study of aqueous solution behavior of polyelectrolytes. In salt free water, polyelectrolyte dimensions are observed to be highly expanded, although still far from adopting a rigid rod like shape.[39-40] It should also be noted that even for addition of small quantities of monovalent salts, the

situation is not completely defined in the sense that counterions were considered as point charges. For example, site binding to polysulfonic acids is favored by the small size of the hydrated ion (K^+, Na^+ or Li^+)[41-42] whereas with polycarboxylic acids, the opposite sequences are observed, i.e., the binding favors the small size of the dehydrated ion.[43] Finally, only electrostatic screening by salts is considered and not their chemical effects. Chemical effects become increasingly important for salts which are non monovalent, reason enough why it is futile to consider higher valence of salts while describing analytical theory. Nevertheless, the theory presented in section 2.1 lays out broad guidelines for the shape of polyelectrolytes in dilute aqueous solutions in the presence of small quantities of monovalent salts. This is exactly the status of what we shall call "reference samples" in Chapters 4-6.

2.2 Shape of polyelectrolytes in poor solvent media- Coil to globule transitions

It was observed more than half a century ago that polymethacrylic acid (PMA) and polyacrylic acid (PAA) behaved differently when their aqueous solutions were neutralized. Although the viscosity of PAA increased smoothly with increasing neutralization[1-2] (indicating smooth chain expansion), PMA resisted chain expansion upto a critical degree of neutralization.[44] The difference in the behavior is due to the fact that while water is a good solvent for PAA, it is a poor solvent for PMA which has hydrophobic methyl groups. Polyelectrolytes, in poor solvents, tend to minimize unfavorable contact with the solvent and resist chain expansion. Crescenzi et al.[45] could show that the calorimetric titration curve of PMA showed an endothermic peak in the region of neutralization where a local conformational transition takes place. No such peak was visible in the calorimetric titration curve of PAA. This is shown in fig. 2.6.
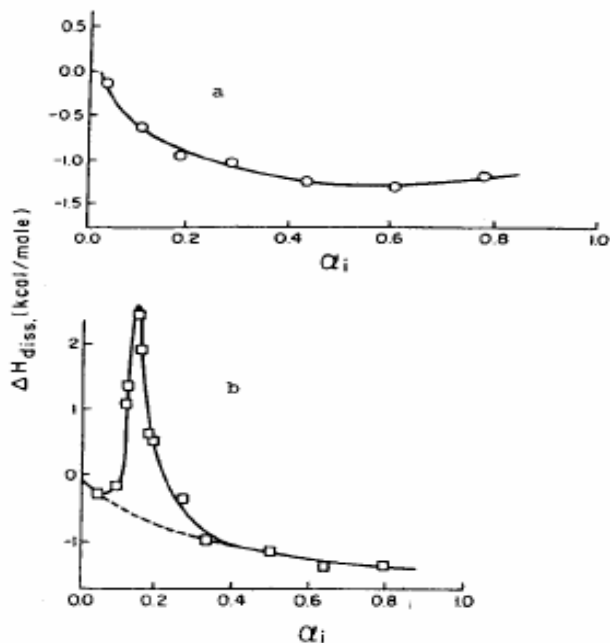
Figure 2.6: Calorimetric titration curve of (a) PAA (b) PMA. The degree of neutralization is represented by α. (adopted from ref. [45])

Some years later, Mandel et al.[46] and Morawetz et al.[47] repeated the viscosity measurements with PMA and PAA respectively upon neutralization, but using methanol as a solvent rather than water. In both cases, the viscosity first increased with increasing degree of neutralization and then sharply declined, as shown in fig. 2.7. It was suggested that an apparent collapse of polyion chains after reaching a critical degree of neutralization was due to an early condensation of counterions on the polyion in a medium of relatively low dielectric constant and the mutual attraction of ion-pair dipoles so formed.
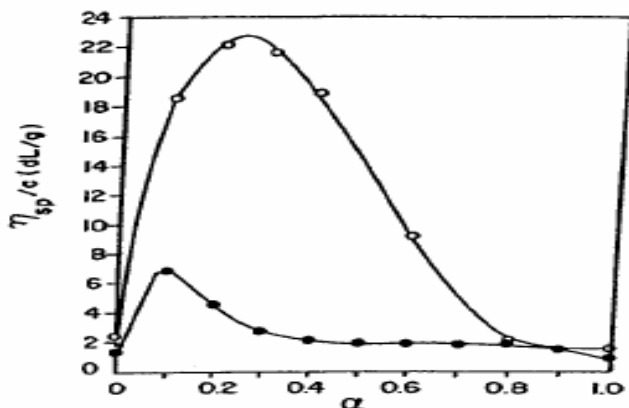
Figure 2.7: Dependance of the solution viscosity of ($\circ$) PAA and ($\bullet$) PMA in methanol solutions on the degree of neutralization with sodium methoxide. (adopted from ref. [47])

The above observations were perhaps the beginning of a rigorous theoretical analysis of coil collapse in poor solvent media. Before we discuss the underlying physics, it should be emphasized that a subtle interplay of many factors can cause this collapse, of which solvent quality is but a part. For example, a coil collapse can occur because of screening of intramolecular electrostatic repulsions by addition of sufficient amount of monovalent salts, complex bond formations with added bivalent salts, change of pH, deterioration of solvent quality or a subtle interplay of all of them. We would pursue this point further in section 2.3 with special reference to polyacrylic acid, a polyelectrolyte thoroughly investigated in this thesis. When any of the aforementioned happens, the standard extended conformation is abandoned and the polyelectrolyte undergoes what is called a coil to globule transition.

Theoretical predictions regarding the structure of intermediate states along the coil to globule transition of polyelectrolytes follow from the concept of shape instability of a charged globule. The problem was considered by Lord Rayleigh more than 100 years ago.[48] In his classical experiments, Rayleigh had shown that a charged droplet would split into smaller droplets if its electrostatic energy (given by $Q^2/D\varepsilon_0 R$) exceeded its surface energy (given by γR^2) where Q is the initial charge on the droplet, R is its radius, D is the dielectric constant of the liquid, γ is the surface tension at the liquid-air interface and ε_0 is the permittivity of free space. Balancing the two energies, the critical charge, Q_{crit} scales with the radius of the charged droplet as $R^{3/2}$. A set of smaller droplets would result if initial charge on the droplet exceeds Q_{crit}. The charge on any of the smaller droplet finally would be smaller than the respective critical charge for that droplet. A charged globule reduces its energy in a very similar fashion when in poor solvent media. It either

elongates into a cylinder or into two smaller globules connected by a narrow string. The state which gives the lowest total free energy (sum of Coulomb and surface energies) is the preferred one. We shall shortly evaluate total free energy for both these predicted states, compare the two energies and conclude which state would be preferred. But there remains one important definition which should be dealt with beforehand. In what follows, the evaluation of surface energy of states shall be achieved with the help of a new parameter. It is called the thermal blob size and abbreviated as ξ_T. The scaling law $\xi_T \approx b/\tau$ applies for poor solvents.[49] Just like at length scales shorter than electrostatic blob size, ξ, the chain is unperturbed by electrostatic interactions, at length scales shorter than thermal blob size, ξ_T, the chain is unperturbed by volume interactions. The structure of the polyelectrolyte chain can be imagined as a dense packing of thermal blobs during surface energy evaluation. The surface tension, γ is of the order of $\dfrac{kT}{\xi_T^2}$ per thermal blob.

In a poor solvent, ξ_T is always less than ξ.

2.2.1 Cylindrical globule model

It was suggested by Khokhlov[32] in 1980 that in order to optimize its energy, the polyelectrolyte chain in poor solvent media takes the shape of an elongated cylindrical globule. The theory got credence from simulation observations, made a decade later, by Hooper et al.[50] and Higgs and Orland[51] incorporating the interplay between long range electrostatic repulsions and short range segment-segment attractions along a polyelectrolyte chain in a poor solvent. Shortly thereafter, the theory of Khokhlov was extended by Raphael and Joanny[52] to the case of annealed polyelectrolytes and by Higgs and Raphael[53] to the case of screening of electrostatic interactions by added salt. In section 2.1.4, we discussed the electrostatic blob model. The cylindrical globule model is

a subset of the electrostatic blob model in the sense that here we are concerned only with

$T < \theta$ case (poor solvent). Let us try to calculate the total free energy of a cylindrical

globule state.

Assume that the cylindrical globule has a length, L_{cyl} and a width, D_{cyl} (where it is

important to note that D_{cyl} is the same as electrostatic blob size, ξ would be in a poor

solvent- refer eq. 2.24, $T < \theta$ case). The surface energy of this cylindrical globule is given

by $F_{sur} \approx \gamma L_{cyl} D_{cyl} \approx \dfrac{kT}{\xi_T^2} L_{cyl} D_{cyl}$ (all prefactors omitted) where k is the Boltzmann constant

and T, the absolute temperature. In writing the surface energy, we have, as mentioned

earlier, imagined the entire cylindrical globule as a dense packing of thermal blobs of

size, ξ_T. The Coulomb energy of the cylindrical globule is given by $F_{coul} \approx \dfrac{e^2 f^2 N^2}{\varepsilon_0 D L_{cyl}}$ (all

prefactors omitted) where e is the electronic charge, f is the fraction of charged

monomers, N is the degree of polymerization, ε_0 is the permittivity of free space and D is

the dielectric constant of the medium. The volume occupied by this cylindrical globular

molecule would be same as if it were an uncharged globule in a poor solvent, i.e., $L_{cyl} D_{cyl}^2$

$\approx b^3 N/\tau$ according to the scaling law[27] where b is the monomer size and τ is the reduced

temperature. The minimization of free energy $F_{cyl} = F_{sur} + F_{coul}$ at constant volume now

leads to the cylinder length

$$L_{cyl} \approx bN\tau^{-1}(\Phi f^2)^{2/3} \tag{2.37}$$

and width

$$D_{cyl} \approx b(\Phi f^2)^{-1/3} \tag{2.38}$$

At these values of L_{cyl} and D_{cyl}, the free energy is given by

$$\frac{F_{cyl}}{kT} \approx \frac{\lambda_B f^2 N^2}{L_{cyl}} \approx \tau(\Phi f^2)^{1/3} N \tag{2.39}$$

where $\Phi = \frac{\lambda_B}{b}$, λ_B being the Bjerrum length.

In a poor solvent, $\tau > (\Phi f^2)^{1/3}$ (corresponding to $\xi_T \approx b/\tau < \xi$). However, it is shown below that eq. 2.39 does not represent the free energy minima of the polyelectrolyte chain under these conditions.

2.2.2 Necklace globule model

The cylindrical globule mentioned above is unstable to capillary wave fluctuations similar to the ones that result in the splitting of a charged liquid droplet. It was suggested by Kantor and Kardar[54-55] that a polyelectrolyte with long range repulsions and short range attractions may form a necklace with compact beads joined by narrow strings-a necklace globule. The idea was extended by Rubinstein et al.[56] a year later. They could show that in a poor solvent, the free energy of a necklace globule is lower than that of a cylindrical globule. Similar results were obtained by Solis and Cruz[57] and Migliorini et al.[58] using variational approach, and by Pickett and Balazs[59] using Self Consistent Field calculations. Consider a necklace globule, as shown in fig. 2.8, with N_{bead} beads of size d_{bead} (where again d_{bead} is the same as electrostatic blob size, ξ would be in a poor solvent- refer eq. 2.24, $T < \theta$ case) joined by N_{bead}-1 strings of length l_{str} and width d_{str}. Let m_{bead} and m_{str} be the number of monomers in one bead and one string respectively. Let L_{nec} be the total length of the necklace globule. Without considering any prefactors, the free energy of such a necklace globule is

$$\frac{F_{nec}}{kT} \approx N_{bead}\left[\frac{\lambda_B f^2 m_{bead}^2}{d_{bead}} + \frac{d_{bead}^2}{\xi_T^2}\right] + (N_{bead}-1)\left[\frac{\lambda_B f^2 m_{str}^2}{l_{str}} + \frac{l_{str} d_{str}}{\xi_T^2}\right] + \frac{\lambda_B f^2 N^2}{L_{nec}} \tag{2.40}$$

where k, T, λ_B, f, N and ξ_T are respectively, the Boltzmann constant, the absolute temperature, the Bjerrum length, the charge fraction, the number of monomers and the thermal blob size.

The pair of terms in the first square brackets in eq. 2.40 represent the electrostatic and surface energy of beads respectively. The pair of terms in the second square brackets represent the same values respectively for strings. While writing surface energies, as mentioned earlier, the entire necklace globule has been imagined as a dense packing of thermal blobs of size, ξ_T. The last term represents electrostatic repulsions between different beads and strings.
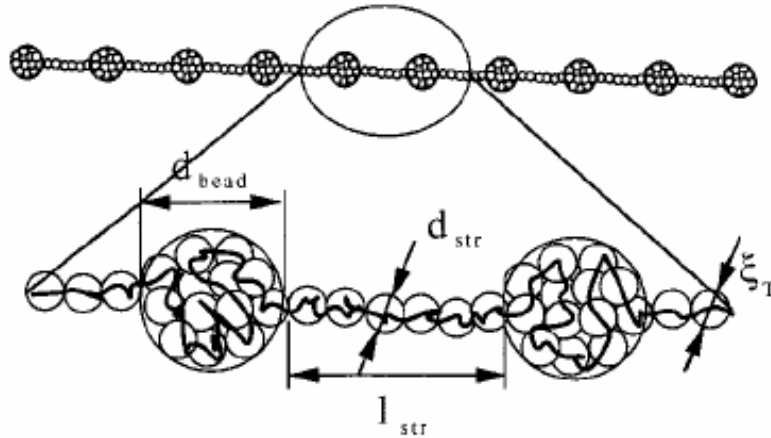
Figure 2.8: A necklace globule with N_{bead} beads (10 shown) of size d_{bead} joined by N_{bead}-1 strings of length l_{str} and width d_{str}. For evaluation of its surface energy, imagine the entire necklace globule as a dense packing of thermal blobs of size, ξ_T. (adopted from ref. [56])

In eq. 2.40, the following scaling laws[56] can be shown to apply.

$$d_{bead} \approx b\tau^{-1/3}m_{bead}^{1/3} \qquad (2.41)$$

$$m_{str} \approx \tau l_{str}d_{str}^{2}/b^{3} \qquad (2.42)$$

where τ and b are respectively, the reduced temperature and the monomer length.

Further, the total length of the necklace can be written as

$$L_{nec} = (N_{bead}\text{-}1)l_{str} + N_{bead}d_{bead} \tag{2.43}$$

Since the total number of monomers in all strings and beads should be equal to the degree of polymerization, N of the chain, we can write

$$N_{bead}m_{bead} + M_{str} = N \tag{2.44}$$

where $M_{str} = (N_{bead}\text{-}1)m_{str}$ equals the total number of monomers in all the strings.

Combining eqs. 2.40-2.44 and minimizing the free energy in the limits $l_{str} \gg d_{bead}$ and $d_{str} \ll d_{bead}$, we get

$$\frac{F_{nec}}{kT} \approx Nf\tau\left(\frac{\Phi d_{str}}{b}\right)^{1/2} \quad \text{for } d_{str} > \xi_T \tag{2.45a}$$

and

$$\frac{F_{nec}}{kT} \approx Nf\left(\frac{\Phi b}{d_{str}}\right)^{1/2} \quad \text{for } d_{str} < \xi_T \tag{2.45b}$$

where $\Phi = \dfrac{\lambda_B}{b}$, λ_B being the Bjerrum length.

From eqs. 2.45a-b, it is clear that the free energy of the necklace globule decreases with decreasing d_{str} till the point d_{str} is of the same length scale as ξ_T and then starts increasing. Thus, the optimal configuration is represented when $d_{str} \approx \xi_T$. At this optimal configuration,

$$\frac{F_{nec}}{kT} \approx \tau^{1/2}\left(\Phi f^2\right)^{1/2} N \tag{2.46}$$

In a poor solvent, $\tau > (\Phi f^2)^{1/3}$ (corresponding to $\xi_T \approx b/\tau < \xi$) and thus, free energy of the necklace globule (eq. 2.46) will be lower than that of cylindrical globule (eq. 2.39). The necklace globule is then the energetically preferable state for the polyelectrolyte chain in poor solvent media.

Following this work, the necklace globule state has been thoroughly investigated theoretically and through simulations over the last decade. Since the characterization of this necklace globule state in solutions and its direct visualization on surfaces lies at the core of this thesis, we shall now present some important characteristics of this state. Both the strongly charged (quenched) and weakly charged (annealed) polyelectrolytes would be taken up. Simulation snapshots would be included wherever available.

2.2.2.1 Effect of charge

With respect to the free energy minima at the optimal configuration of the necklace globule represented by eq. 2.46, we can evaluate simple expressions for important chain parameters in terms of charge fraction, f.

$$L_{nec} \approx b(\Phi/\tau)^{1/2}fN \tag{2.47}$$

$$d_{bead} \approx b(\Phi f^2)^{-1/3} \tag{2.48}$$

$$l_{str} \approx b(\tau/\Phi f^2)^{1/2} \tag{2.49}$$

where symbols have their usual meanings.

Importantly, eqs 2.47-2.49 show that as charge fraction on a chain is decreased while maintaining the same solvent quality, the length of the necklace globule decreases and so does the length of the strings but the size of the beads increases.

Finally the charge fraction, f can be evaluated in terms of the number of beads, N_{bead}.

$$f \approx (\tau N_{bead}/\Phi N)^{1/2} \tag{2.50}$$

where symbols have their usual meanings.

Eq. 2.50 shows that the number of beads would decrease as the chain discharges at a particular solvent quality. The reason for mentioning this equation separately is that it defines a kind of a boundary for the charge fractions a necklace globule can and cannot

incur. This follows from the fact that the variable N_{bead} can take only integral values. Thus the necklace globule represents a cascade of intermediate states with different number of beads.

Rubinstein et al.[56] also preformed Monte Carlo simulations of a freely jointed uniformly charged chain in a poor solvent interacting via unscreened Coulomb (long range repulsive) and Lennard-Jones (short range monomer-monomer attractive) potentials. The simulations showed that the critical charge, Q_{crit} (refer Rayleigh's experiment mentioned earlier) at which a charged globule becomes unstable scales as $N^{1/2}$ where N is the degree of polymerization. At a fixed degree of polymerization, when the charge is made slightly more than the critical charge, Q_{crit} the charged globule adopts the shape of a dumbbell. On further increasing the charge, the dumbbell splits into a necklace with three beads joined by two strings. This is shown in fig. 2.9.
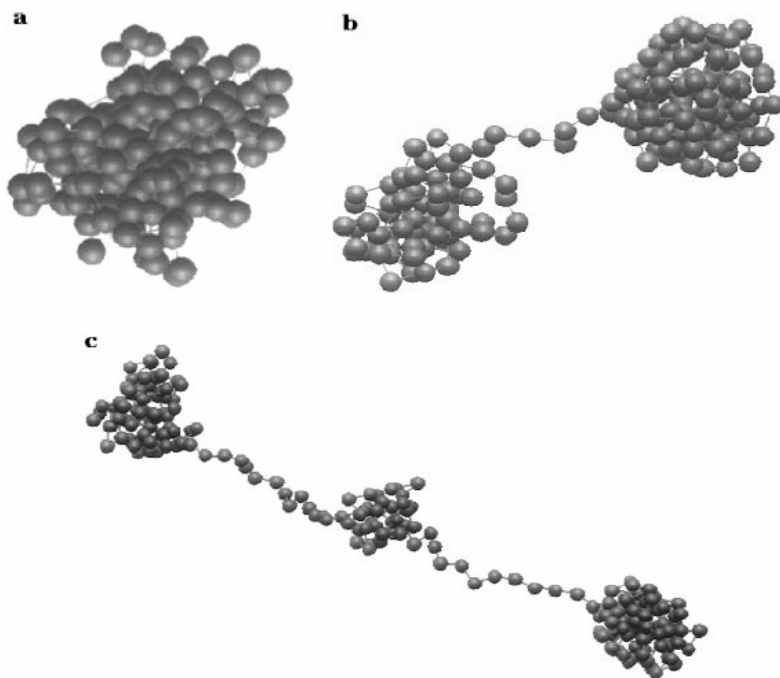
Figure 2.9: Monte Carlo simulation snapshots of a freely jointed uniformly charged chain in a poor solvent.The simulated chain has a fixed degree of polymerization, $N = 200$ monomers. (a) spherical globule at $f = 0$ (b) dumbbell at $f = 0.125$ (c) necklace with three beads and two strings at $f = 0.15$ (adopted from ref [56])

The conformational changes induced by varying charge in the case of annealed polyelectrolytes under poor solvent conditions[60] as well as close to θ solvent conditions[61] were investigated through Monte Carlo and (semi-)grand canonical Monte Carlo simulations respectively by Uyaver and Seidel. The chain interactions were simulated via screened Coulomb (Yukawa) repulsions and a modified Lennard-Jones potential which included both monomer-monomer short range attractive and monomer-solvent interactions. Their approach was to progressively increase the charge on the polyelectrolyte by increasing the solution pH (and hence the chemical potential, μ). As already mentioned in section 2.1.5, annealed polyelectrolytes carry charge inhomogeneities resulting in a slight depletion of charge in the middle and its concentration towards the ends of the chain. Under poor solvent conditions, this charge inhomogeneity results in a first order discontinuous transition from a collapsed globule to an extended chain. Necklace globule, if at all existent, is unstable in such a case. This is shown in fig 2.10.

Figure 2.10: Monte Carlo simulation snapshots of an annealed polyelectrolyte in a poor solvent. i) collapsed globule at μ = 4.0 ii) extended chain at μ = 9.0. The intermediate states are unstable. Charged monomers are colored black. The chain has a fixed degree of polymerization, $N = 256$. (adopted from ref. [60])
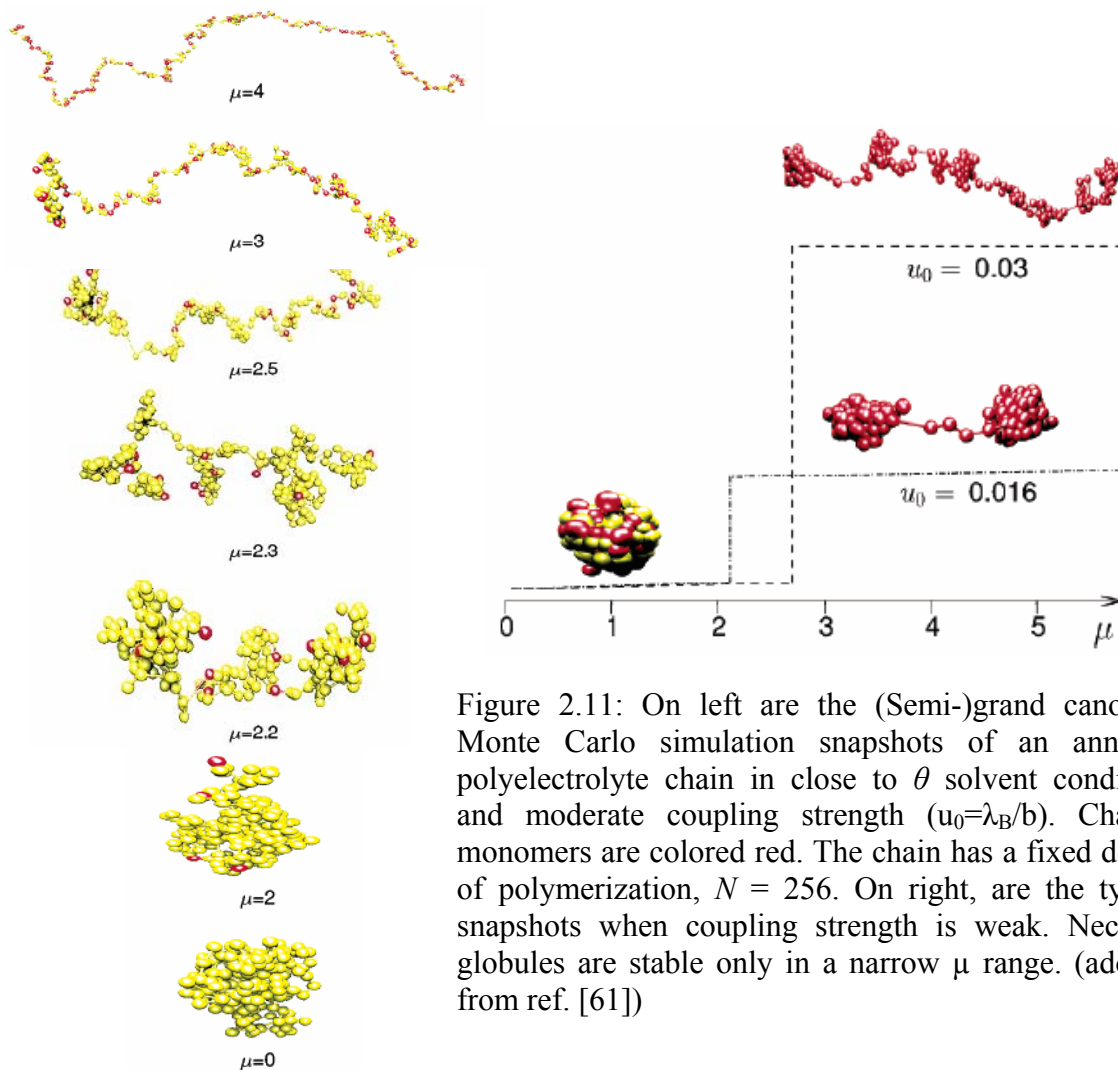
Figure 2.11: On left are the (Semi-)grand canonical Monte Carlo simulation snapshots of an annealed polyelectrolyte chain in close to θ solvent conditions and moderate coupling strength ($u_0 = \lambda_B/b$). Charged monomers are colored red. The chain has a fixed degree of polymerization, $N = 256$. On right, are the typical snapshots when coupling strength is weak. Necklace globules are stable only in a narrow μ range. (adopted from ref. [61])

Under close to θ solvent conditions however, the charge inhomogeneity decays and a cascade of intermediate states become stable. Note that even in the latter case, the necklace globule forms in a very narrow range of chemical potentials (or pH). This is shown in fig. 2.11.

In both figs. 2.9 and 2.11, the necklace globule shows a large fluctuation in bead size and number, as predicted by theory (eq. 2.50) (snapshots not shown).

2.2.2.2 Effect of added salt

Effect of an added monovalent salt at different solvent qualities on the conformation of a strongly charged polyelectrolyte chain was later investigated by Molecular Dynamics

simulations[62] as well as by Monte Carlo simulations.[63] In these simulations, the effect of added salt was taken into account through the Yukawa potential (screened Coulomb potential). The effect of solvent quality (short range monomer-monomer attractions arising due to hydrophobicity) was included using Lennard-Jones potential. We shall summarize here the interesting findings of Chodanowski and Stoll[63] who analyzed the full domain of stability of necklace globule structures along the coil to globule transition. The Monte Carlo simulation snapshots obtained by them are reproduced in fig. 2.12. Due to lack of space, extended chains which exhibit large dimensions have been reduced in size and subsequently appear smaller than they really are. The following text should be read with fig. 2.12 in perspective.

Region *A*- In the limit of weak hydrophobic interaction (0-2 *kT*) and when the ionic strength of the solution is less than 0.1M, long range electrostatic repulsions dominate and the chain is largely stretched. However, when ionic strength increases beyond 0.1M, the electrostatic repulsions are increasingly screened causing the chains to adopt a self avoiding walk conformation. At even higher ionic strengths, a random walk conformation is achieved.

Region *B*- When we consider hydrophobic interactions of the order of 3-6 *kT*, the competition between monomer-monomer attraction and repulsive Coulomb interactions results in a system of beads and strings. At low ionic strengths of the solution, first a dumbbell (two globules at the end of a long chain) is formed which further splits, with increased screening, into a set of small globules connected by rigid strings. It is not surprising that the globules always start forming first at the ends of the chain. This is an end effect, we discussed in section 2.1.5. Since near the extremities of the chain, the

electrostatic energy of the charges is lower, conformational entropy now becomes

deciding.
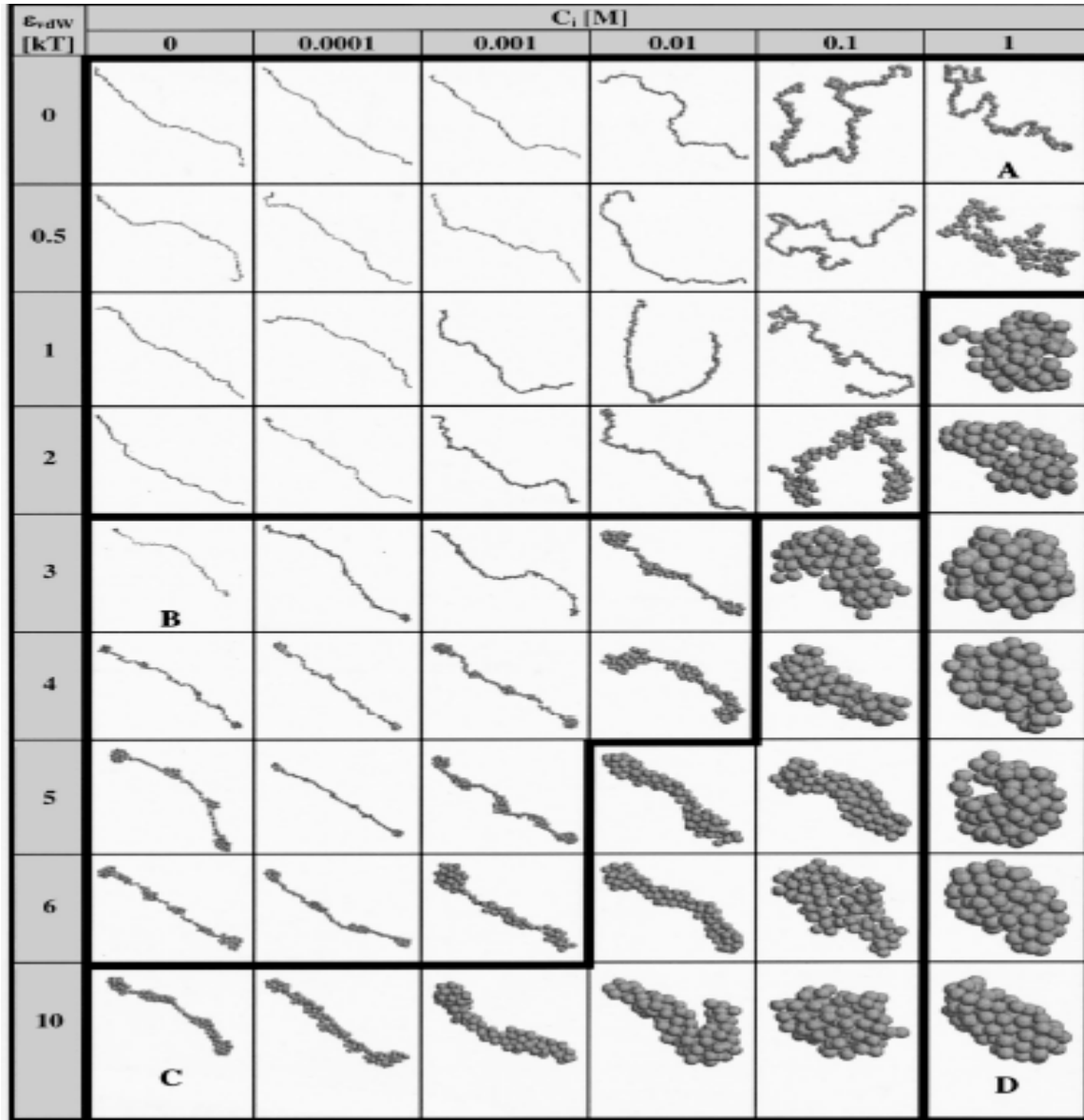
Figure 2.12: Monte Carlo simulation snapshots of a strongly charged polyelectrolyte chain. The symbol ε_{vdw} is used to denote solvent quality (kT). The symbol C_i denotes the ionic strength of solution (M). The polyelectrolyte chain has a fixed degree of polymerization, $N = 100$. Note the four regions-A, B, C and D. Refer text for details. (adopted from ref. [63])

Region *C*- At certain combinations of hydrophobic interactions (3-10 *kT*) and charge screening (ionic strengths upto 0.1M), another exotic intermediate state is identified. Strong short range hydrophobic attractive interactions forcing the monomers to collapse into a cylinder while the concomitant presence of long range electrostatic repulsive interactions forcing chain extension results in a cigar shaped structure

Region *D*- Finally when the charges are highly screened (at ionic strengths of 1M), even when hydrophobic interactions are comprised at the range 1 to 10 *kT*, the polyelectrolyte adopts a spherical globule shape.

Ulrich et al.[64] have recently performed a similar Monte Carlo simulation study on weakly charged polyelectrolyte chains interacting via screened Coulomb potential (Yukawa potential) and Lennard-Jones (short range monomer-monomer attractions due to hydrophobicity) potential. The influence of solution pH, ionic strength and hydrophobic interactions between the polyelectrolyte backbone and the solvent have been systematically investigated. Their findings were similar to those of Chodanowski and Stoll that a subtle interplay of monomer-monomer attraction (arising due to hydrophobicity) and repulsive Coulomb interactions result in a necklace globule. Fig. 2.13 shows a diagram of states for possible intermediates along the coil to globule transition of a weakly charged polyelectrolyte over the full range of solution pH and solvent quality at an ionic strength of 0.001 M.

In both figs. 2.12 and 2.13, the necklace globule shows a large fluctuation in bead size and number, as predicted by theory (eq. 2.50) (snapshots not shown). However, it must be noted that both strong and weak polyelectrolytes show another stable intermediate state which is quite different from a necklace globule (including a dumbbell). This is the cigar-
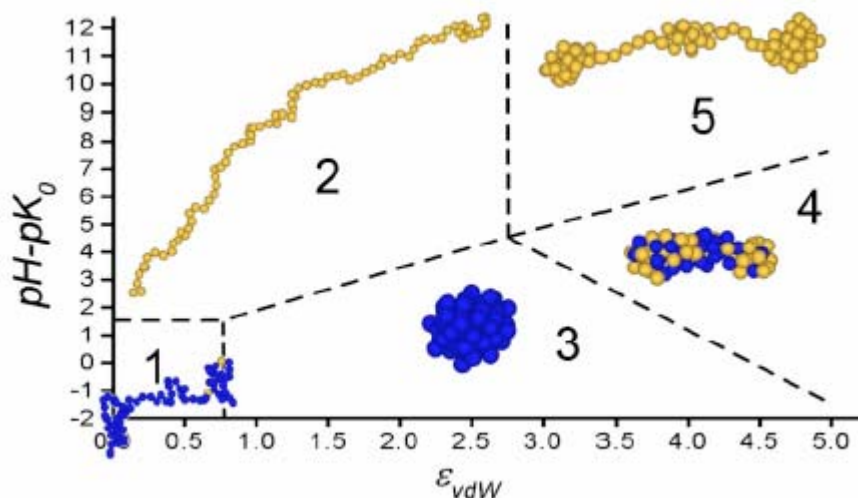
Figure 2.13: Monte Carlo simulation snapshots of a weakly charged polyelectrolyte chain. The symbol ε_{vdw} is used to denote solvent quality (kT). The Y axis represents the value pH-pK_0 where pK_0 represents the intrinsic dissociation constant of an isolated monomer. Charged monomers are colored yellow. The chain has a fixed degree of polymerization, $N = 80$. 1) self avoiding walk 2) extended 3) collapsed 4) cigar-shaped 5) necklace globule (adopted from ref. [64])

shaped state which occupies atleast an equal area in figs. 2.12 and 2.13 as the necklace globule itself. The similarity with Khokhlov's original idea of cylindrical globule[32] given at a time when computer simulations were non existent, and which was subsequently challenged, is striking.

The study of Ulrich et al.[64] should not be treated as a reference study for end effects. The phrase "weakly charged" is used in this study to ignore any counterion condensation but does not include any end effects that may have risen due to weak charging. The study of Uyaver and Seidel[60-61] mentioned in section 2.2.2.1 incorporates end effects in weakly charged polyelectrolytes but does not include the effects of added salts. Thus, the latter authors keep the value of the Debye screening length, λ_D constant throughout. The

presence of a salt can substantially reduce this value and thus can have an effect on stabilities of some of the intermediate states or even give rise to a new intermediate state.

2.2.2.3 Effect of concentration of polyelectrolyte

The existence of different length scales (chain size, string length, bead size) for a necklace globule structure manifests itself in the unique scaling laws in semi dilute solutions. These laws were developed by Dobrynin and Rubinstein.[65-65] Recall the notion of correlation blobs we discussed in section 2.1.4 for semi dilute regime of polyelectrolyte chains in aqueous solution. We shall use the same notion here, albeit for a necklace globule in a poor solvent. There are two very interesting regimes called the string controlled regime and the bead controlled regime. The former refers to semi dilute solutions in which the correlation blob size, r_{corr} is larger than string length, l_{str}. This is shown in fig. 2.14a. The latter refers to semi dilute solutions in which the correlation blob size, r_{corr} is of the order of string length, l_{str}. This is shown in fig. 2.14b. The correlation blob size, r_{corr} is defined as the length scale below which the necklace globule behaves the way it would have behaved in a dilute solution.
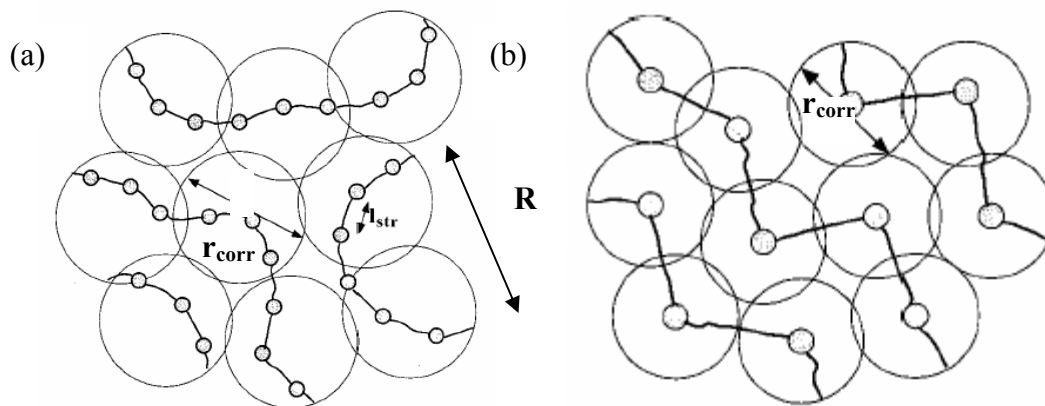
Figure 2.14: (a) string controlled semi dilute solution (b) bead controlled semi dilute solution. The correlation blob size is represented by r_{corr}, length of the string by l_{str} and the end to end distance of the necklace globule by R. (adopted from ref. [65])

Dobrynin and Rubinstein[65-66] found out that for the string controlled regime, scaling laws are similar to the ones obtained by de Gennes[27] for polyelectrolyte chains in aqueous solution. Thus, the correlation blob size, r_{corr} scales as $c^{-1/2}$ and the end to end distance, R scales as $c^{-1/4}$. Refer the similarity with eqs. 2.26 and 2.28 respectively. The necklace globule in this regime can be viewed as a random walk of correlation blobs. However, in the bead controlled regime, both r_{corr} and R show a much stronger concentration dependence, scaling approximately as $c^{-1/3}$. The solution containing necklace globules can now be envisioned as a dilute solution of beads. We shall not go into the details of concentrated regime but just mention that the necklace globule expands in this regime reaching the size of Gaussian coils. This nonmonotonic concentration dependence of necklace globule size in semi dilute poor solvent media is one of its characteristic traits.

A beginning can be considered to have been made for developing scaling laws specific to the case of annealed polyelectrolytes by following the work of Löwen et al.[67] They have taken a different approach altogether while modeling polyelectrolyte inter chain interactions. They begin by proving that weakly charged polyelectrolytes in salt free conditions (below Manning threshold) can be described as soft colloids. More precisely, this line of interpretation would mean that each polyelectrolyte chain can be envisioned as a Gaussian profile of monomers and counterions around its center of mass. Next, the inter chain interactions can be evaluated using the concept of interactions between centers of mass of two soft colloids, thereby making it easier to include not only electrostatic effects but also effects of excluded volume and entropic contribution from counterion distribution. This is shown in fig. 2.15. The calculated interchain potential based upon the above theory gave good agreements with the results of Molecular Dynamics simulations.

In principle, this approach can be used to investigate scaling laws for weakly charged polyelectrolytes (with associated end effects) in concentrated solutions (where Gaussian profile assumption is more likely to hold) but a follow up study is awaited.
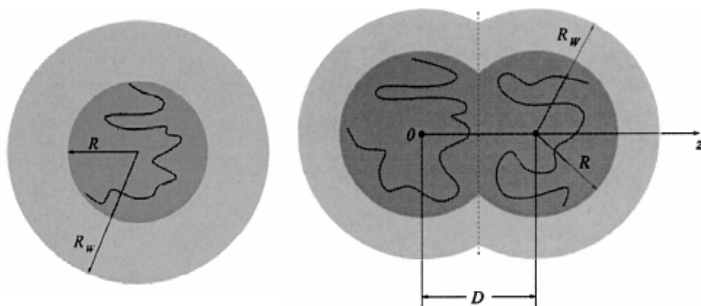
Figure 2.15: A weakly charged polyelectrolyte under salt free conditions can be modeled as a soft colloid according to Löwen et al. The interaction between two soft colloids can then be studied to arrive at novel scaling laws for annealed polyelectrolytes. Here R is the typical spatial extent of the soft colloid (predicted to be half of end to end distance by Löwen et al.) and R_w is the radius of surrounding counterion sphere. D is the distance between centres of mass of two soft colloids. (adopted from ref. [67])

2.2.2.4 Effect of counterion condensation

Theoretically, modeling of partially charged polyelectrolytes with explicit counterions in poor solvent conditions is an uphill task. Lets begin by describing the work Rubinstein et al.[66,68-70] in this direction made through analytical theory and Molecular Dynamics simulations. In their approach, counterion condensation is due to a fine interplay between the reduction of electrostatic repulsion between uncompensated charges and the loss of translational entropy by condensed counterions due to their localization in the vicinity of the polyelectrolyte backbone. In a dilute polyelectrolyte solution, the entropic penalty for counterion localization is very high, and almost all counterions leave the polyelectrolyte chain and stay in solution. However, as polyelectrolyte concentration increases, the entropic penalty for counterion localization decreases, resulting in an increase in the

number of condensed counterions. This model predicts that beads grow in size with increasing polyelectrolyte concentration, while their number per chain decreases and polyelectrolyte chain shrinks. However, it is difficult to resist the conclusion that such a model, as mentioned above, grossly underestimates the role of counterion condensation on polyelectrolyte conformations.

Comprehensive Molecular Dynamics simulations performed by Holm et al.[71-76] shed further light on the exact role of counterion condensation. They have found that polyelectrolyte chains adopt necklace globule conformation only in a narrow range of the interaction parameters. The width of this window in which necklace globule structures are stable is strongly influenced by counterion condensation. All these simulation results indicate a much stronger collapse of polyelectrolyte chain in the presence of counterions than predicted by analytical theory.

What can generate these additional attractive interactions? One source might be the formation of permanent (or relatively long lived) ionic pairs between condensed counterions and oppositely charged monomers. In this case, dipole-dipole interactions between ion pairs result in additional attraction between monomers. We are reminded of earlier studies made by Schiessel and Pincus[77] and by Schiessel[78] where the effect of counterion condensation on the chain conformations in different temperature regimes was presented. The authors could note that the extra attractive forces generated due to permanent dipole-dipole interactions resulted in a decrease of second virial coefficient, shifting the position of the θ temperature. The shift of the θ temperature in case of strongly charged polyelectrolytes could be significant leading to a stronger chain collapse. However, the existence of permanent dipoles is not supported by simulations. In

fact, counterions are highly mobile even when they are localized near the polyelectrolyte backbone.

Another effect which can give rise to attractive interactions is the correlation-induced attraction between condensed counterions and charged monomers. These interactions are due to electrostatic attraction of a condensed counterion to a surrounding charged background consisting of charged monomers and other condensed counterions. This was the basis of the theoretical extension made by Rubinstein et al.[79] in 2006 to account for findings of simulation results of Holm et al.[71-76] mentioned earlier.

We shall now describe the Molecular Dynamics simulations of Holm et al. to give the theory a pictorial background. As usual, there are two interaction potentials in the simulation model. All particles in the simulation box, be them charges on the chain or counterions present in the solution interact via an unscreened Coulomb potential. This means no assumptions are made regarding screening of charges on the chain by the counterions. Instead, any charge on the chain or any counterion in the solution is exposed to full Coulomb potential of all other charges and counterions. This is a new development to what we have seen till here. The other potential is the modified Lennard-Jones potential which includes monomer-monomer, monomer-solvent and counterion-counterion interactions. The last term can be identified as a new addition. The cut offs of the modified Lennard-Jones potential are so chosen that monomer-monomer and monomer-solvent interactions are in a narrow short range attractive regime while counterion-counterion interactions fall in the purely repulsive regime. To summarize the findings, we shall once again take recourse to the diagram of states similar to fig. 2.13. Fig. 2.16 shows the various stable intermediate states along the coil to globule transition.
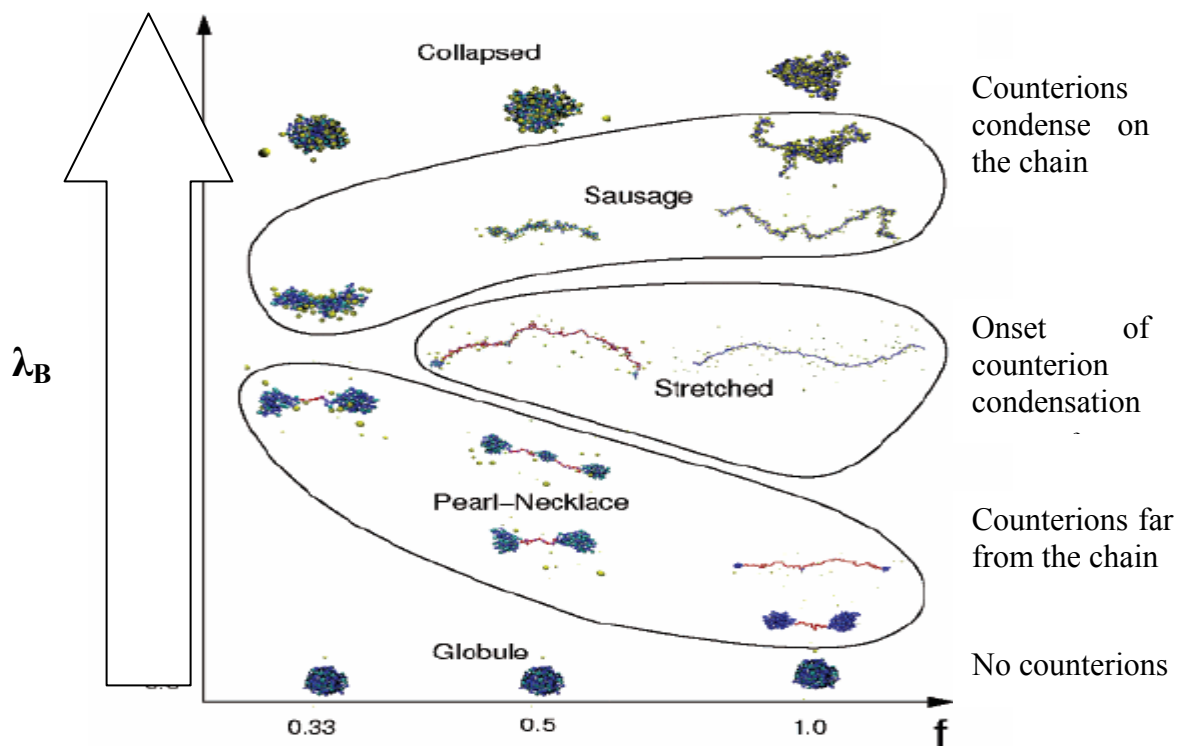
Figure 2.16: Molecular dynamics simulation snapshots of a strongly charged polyelectrolyte chain with explicit counterions in a dilute poor solvent. The chain has a fixed degree of polymerization, $N = 199$. (adopted from ref. [75])

In fig. 2.16, the Bjerrum length, λ_B has been used as a measure of counterion condensation. With increasing λ_B, the chain becomes more charged and counterion condensation increases. Manning's parameter, $\Phi \left(= \dfrac{\lambda_B}{b} \right) = 1$, indicates the onset of counterion condensation, the point where λ_B becomes equal to monomer size, b. The simulations are performed at three different charge fractions, $f = 1/3$, $1/2$ and 1, of the chain.

When λ_B is zero, the chain is not charged at all. The hydrophobic interactions in the poor solvent force the neutral polymer into a globular shape. With increasing λ_B, the globule gets progressively charged till at some point, we observe the Rayleigh's instability

condition setting in. The point at which Rayleigh's instability condition occurs is the same for all charge fractions since the counterions do not play a significant role here. When λ_B is further increased, the three charge fractions behave very differently. Whereas the series with $f = 1/2$ and $f = 1$ show a cascade of Rayleigh's instabilities budding more beads (with decreasing bead size and increasing distances between them) until they reach stretched conformation, the series with $f = 1/3$ has dumbbell conformation at its maximum extension. The maximum extension itself is reached at different values of λ_B. For $f = 1$ series, the maximum extension is probably more restricted by chain entropy than that is determined by the interplay between repulsive and attractive interactions. The chains then slowly shrink and enter the sausage regime. It results because of screening of charges on the chain induced by counterion condensation in a way that beads begin to coalesce. Still at the same value of λ_B, the chains with $f = 1$ are much longer than the chains with $f = 1/2$ or $f = 1/3$. Finally, the collapsed conformation is reached roughly at the same value of λ_B. Note that the transition back to globule is not a first order discontinuous transition, instead a smooth continuous process, passing through a sausage state.

In accordance with eq. 2.50, strong fluctuations in the number, size and position of beads is observed at a particular f and λ_B (snapshots not shown). Moreover, when the same study is done with varying concentration, it is observed that beads grow in size while their number per chain decreases with increasing polyelectrolyte concentration. Since counterion condensation takes place preferably on beads and is directly responsible for increasing bead sizes, it appears that counterion condensation increases with increasing polyelectrolyte concentration.

The same results are observed in a good solvent, except for the fact that transition is more pronounced in a poor solvent.

2.2.3 General comments

More or less the same lacunae exist in theories developed for coil to globule transitions as for theories regarding extended shape of polyelectrolytes in aqueous solutions, namely, solvent is treated as homogenous, thermal fluctuations are not taken into account, ions are considered as monovalent point charges and chemical effects of ions are ignored. Moreover, along the coil to globule transitions, we have not bothered about precipitation effects. But in the real world, precipitation and collapse transitions compete. We shall bring up these factors in the next section with reference to polyacrylic acid. Nevertheless, the simulation snapshots provided are expected to act as references for the AFM images produced in Chapters 4-6 representing samples along the coil to globule transition.

2.3 The case of Polyacrylic acid

Polyacrylic acid is an example of a weakly charged or annealed polyelectrolyte for which water acts as a good solvent. Lets keep the technical details of a good solvent aside for a moment bearing in mind only this: the term good solvent is based on a scaling law which says that radius of gyration, R_g scales with molecular weight of the polyion, M as $R_g \approx M^v$ where v is 0.6. The value of v is less than 0.6 for a θ solvent. When dissolved in water, polyacrylic acid adopts the shape of a coiled chain. An increase of the pH to 9 transforms the coiled chain to a highly extended chain (refer fig. 2.11, $\mu \approx 10$, to have a visual impression).

If an alkaline salt like NaCl or NaBr is now added, the strong electrostatic interactions are increasingly screened, the chain's hydrophobicity increases and the extended chain starts

to shrink. If the amount of added alkaline salt is high enough, the shrinking process leads to unperturbed or θ dimensions describable by a random walk[80-82] This situation can be verified, for example, with 1.5 M NaBr solution of polyacrylic acid at pH 9 (all measurements being made at 15°C).[83-84] Beyond this alkaline salt level, phase separation usually sets in.[85-87] The latter is denoted as H-type precipitation because the amount of added salt is high irrespective of polyacrylate concentration. Such salts are denoted as inert salts.

If salts of bivalent cations are used instead of inert salts, coil shrinking and precipitation is observed at much lower salt concentrations.[87-89] In this case, phase separation is denoted as L-type precipitation. The amount of bivalent cations required for precipitation increases with increasing polyacrylate content (in sharp contrast to law of mass action) being roughly equimolar to the carboxylate residues. Obviously, bivalent cations are chemical entities that form complex bonds with the anionic carboxylate residues along the polyacrylate backbone, thus interacting more specifically than alkaline cations do.

Interestingly, it has been established through experiments that the most drastic shrinking of coil dimensions of polyacrylates in the presence of bivalent cations occurs just before the L-type precipitation threshold.[87,89-91] Any intermediate state along the coil to globule transition should therefore also logically be found just before the precipitation threshold. (We have dropped the prefix L-type. Until otherwise stated, the word "precipitation threshold" in this thesis should be construed to mean "L-type precipitation threshold"). To access these intermediate states experimentally is however quite challenging. The speed at which coil to globule transition takes place coupled with the fact that all

intermediate states lie extremely close to the precipitation threshold either makes them inaccessible[92-95] or unstable[96], depending upon the experimental technique.

In 1993, Huber[90] gave a powerful method to gradually approach the precipitation threshold in a highly systematic way. Huber observed that presence of an inert salt is essential to study collapse behavior of polyelectrolytes by bivalent salts. This may seem contrary to intuition at first. But the presence of an inert salt, say NaL (*L* stands for the ligand of the inert salt), can be used to fix the salt concentration of the polyelectrolyte solution a priori. Lets say it is fixed at M_0 moles/liter. Then the bivalent salt, say MCl_2 (*M* stands for the specific cation of the bivalent salt), can be slowly added to the solution while keeping the overall concentration of positive charges constant, i.e., $[Na^+] + 2[M^{2+}]$ = M_0. This replacement of Na^+ by M^{2+} at constant concentration of positive charges allows the isolation of specific interactions with bivalent salts exceeding the regular screening effects of the inert salt. Schweins and Huber[97-103] have successively established phase diagrams for collapse behavior of polyacrylates in the presence of various bivalent cations based upon this approach, using static and dynamic light scattering to identify progressive coil collapse and eventual aggregation (precipitation). They have also investigated the shifts of phase boundary in terms of molecular weight of polyacrylate[90], initial concentration of inert salt[97], change of solvent from H_2O to D_2O[99], increase of size of bivalent cation[101] and increase of temperature from 15°C to 30°C.[103]

Let us say that at the phase boundary, the concentration of bivalent cations is represented by *Cs** and the corresponding polyacrylate concentration as *Cp**. It was found that as long as the initial concentration of the inert salt, [NaL] = M_0, is low and the solution is dilute, the phase boundary follows a straight line representable by

$Cs* (Y) = m + r_0 Cp*(X)$ (2.51)

In eq. 2.51, m is the minimum amount of bivalent cations required to generate phase separation at infinite dilution and r_0 could be interpreted as the amount of bivalent cations bound per COO⁻ group of the polyacrylate. Eq. 2.51 is in line with theoretical predictions of Michaeli[89], Narh and Kellar[104], Cruz et al.[105] and Wittmer et al.[106]

Experimentally, such a phase boundary can be approached using two routes. Route 1 is an approach parallel to the X axis keeping the total positive ion concentration and pH constant while slowly increasing the bivalent cation / polyacrylate ratio by decreasing the polyacrylate concentration. Route 2 is an approach parallel to the Y axis keeping again the total positive ion concentration and pH constant while increasing the bivalent cation / polyacrylate ratio by increasing the bivalent cation concentration. We should be cautious regarding two things. One, no matter which route we take to approach the phase boundary, all samples prepared along that route should lie in single phase region. This means that care must be taken that we are always below the critical concentration of bivalent cation required to precipitate the polyacrylate. Two, the initial inert salt concentration should be so chosen that water acts as a good solvent (recall the scaling law mentioned earlier in this section) for polyacrylate chain at the experimental pH. At a pH of 9, this is true upto an initial inert salt concentration of 1.5M. At initial inert salt concentrations of 1.5M or above while at pH 9, water starts to behave as a θ solvent for polyacrylates. This can give rise to another phase boundary occurring even without any bivalent cation.

We shall now reproduce some phase diagrams for polyacrylates as these hold special relevance for Chapters 4-6. Recall that intermediate states along the coil to globule

transition of polyacrylates induced by bivalent cations are found very close to the

precipitation threshold. Hence, an idea of the phase boundaries and their shifts depending

upon various parameters is essential.

2.3.1 Phase boundary of polyacrylates- Dependence on molecular weight

Fig. 2.17 shows the phase boundary for CaPA (PA for polyacrylate) at an initial inert salt

concentration of 0.1 M where the solution pH was kept constant at 9. Phase boundary was

established by measuring samples through SLS and DLS along route 1. The molecular

weights of NaPA coils were 793 KDa and 1250 KDa respectively.
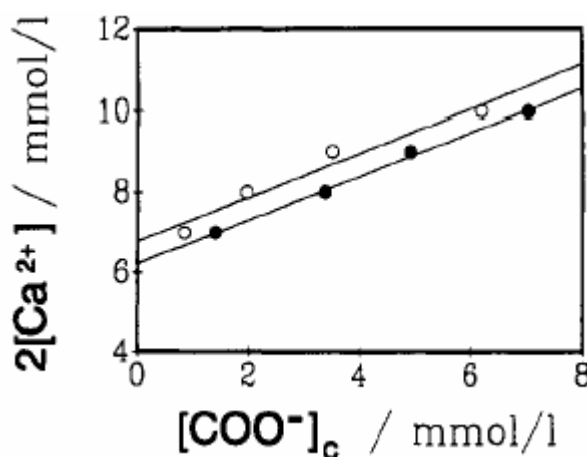
Figure 2.17: CaPA phase boundary in 0.1 M NaCl solution at pH 9 (○) Mol. Wt. of NaPA = 793 KDa (●) Mol. Wt. of NaPA = 1250 KDa. The straight lines indicate fits according to eq. 2.51. (adopted from ref. [90])

With reference to eq. 2.51, we can notice that the slope r_0 is approximately the same in

both cases indicating same number of Ca^{2+} ions are bound per COO^- group. The value r_0

= 0.5 indicates that coil collapse concentration $[COO^-]_c$ will be shifted by an increment

which is 4 times as large as the corresponding increase in the Ca^{2+} concentration,

irrespective of the molecular weight of NaPA. This points to the stoichiometric nature of

coil collapse, i.e., stoichiometric amounts of Ca^{2+} can cause drastic changes in NaPA coil

shape. The second parameter m is slightly less for higher molecular weight of NaPA (m =

6.23 mM) than for lower molecular weights (m = 6.8 mM). The situation is specific to

this case only and should not be treated as a benchmark. This is because precipitation is a two step process. In the first step Na^+ ions are replaced by Ca^{2+} ions which interact with COO^- groups of the polyacrylate backbone much more strongly than Na^+ does. This makes the charges much more screened and the polyacrylate backbone much more hydrophobic causing it to shrink There is also a complex bonding between Ca^{2+} and COO^- groups including the possibility of intramolecular COO^--Ca^{2+}-COO^- bridges causing a fast coil collapse. Meanwhile, an increase in hydrophobicity of the chains means that they can easily interact with each other causing them to precipitate in the second step.

2.3.2 Phase boundary of polyacrylates- Dependence on initial inert salt concentration

Fig. 2.18 shows phase boundaries for CaPA at three different initial inert salt concentrations- 0.01 M, 0.1 M and 1.5 M. The molecular weight of NaPA was 2300 KDa (polyacrylic acid measured in 0.1 M NaCl). Apart, an additional phase boundary is shown for CaPA at initial inert salt concentration of 0.1 M. Here the molecular weight of NaPA was 660 KDa. All solutions were at pH 9. All phase boundaries were established by measuring samples through SLS and DLS along route 1 except for samples containing 1.5 M of initial inert salt concentration where route 2 was followed. It is because in the latter case, water acts as a θ solvent and r_0 (eq. 2.51) is zero by definition. The full symbols indicate the samples which showed the most drastic coil collapse at the precipitation threshold. It highlights how samples were selected in this thesis for probing the structure of intermediate states along the coil to globule transition.
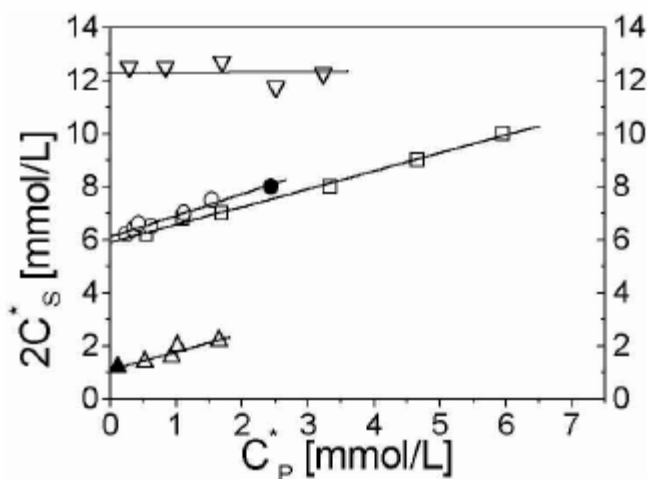
Figure 2.18: CaPA phase boundaries in (Δ) 0.01 M ($\circ$) 0.1 M ($\triangledown$) 1.5 M NaCl solution at pH 9. Mol. Wt. of NaPA = 2300 KDa when measured in 0.1 M NaCl. An additional CaPA phase boundary is shown for NaPA = 660 KDa measured in 0.1 M NaCl at pH 9 ($\square$). Full symbols indicate samples which showed the most drastic coil collapse at the precipitation threshold. The straight lines indicate fits according to eq. 2.51. (adopted from ref. [97])

It can be seen that an increase of initial inert salt content shifts the phase boundary to larger values of Ca^{2+} causing the two-phase region to recede. This can be explained by the tendency of Na^+ ions to resist displacement by stronger Ca^{2+} ions. The greater the number of Na^+ ions initially, the stronger is this resistance and larger the number of Ca^{2+} ions required to overcome it. It is important to note that with increasing Ca^{2+} concentration, another one-phase region can be expected. The NaPA chains are getting electrically charged once again due to extensive binding with Ca^{2+} ions. At a distinct initial inert salt content, a regime can be expected where both phase boundaries meet each other at low values of Cp, thereby connecting the two one-phase regions. As suggested by fig. 2.18, the initial inert salt content in this regime must be larger than 0.1 M but smaller than 1.5 M because the latter content behaves as a θ solvent and can give rise to a phase boundary even without any Ca^{2+}.

On the other hand, starting from any particular sample on the precipitation threshold (say those shown by full symbols in fig. 2.18), if NaCl is added while keeping the total

number of positive charges constant, Na^+ ions start displacing Ca^{2+} ions. Since Na^+ is only weakly interacting compared to Ca^{2+}, the collapsed coil begins to expand- an NaCl induced expansion of CaPA!

2.3.3 Phase boundary of polyacrylates- Change of solvent from H_2O to D_2O

It has been shown for various charged macromolecules that more energy would be required to break a D_2O solvent cage than a H_2O solvent cage. Hence, hydrophobic (or deuterophobic, as they are sometimes euphemistically called) interactions are stronger in D_2O than in H_2O. Since an increase in hydrophobicity means that chains can interact more easily with each other, we can predict that precipitation is likely to be faster in D_2O, all other factors remaining the same. This is shown in fig. 2.19. The NaPA sample had a molecular weight of 950 KDa. The initial inert salt concentration was set to 0.01 M and the solution was maintained at pH 9. The CaPA phase boundary was established by measuring samples through SLS and DLS along route 1. The full symbols indicate data in H_2O while the open symbol stands for data collected in D_2O.
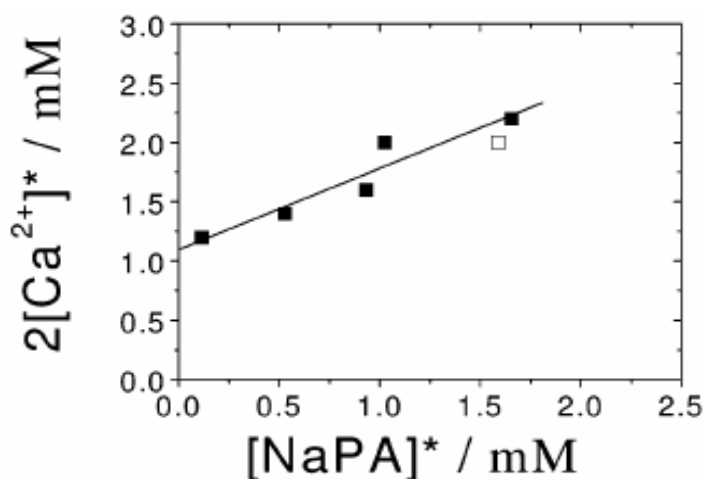
Figure 2.19: CaPA phase boundary in 0.01 M NaCl solution at pH 9 (■) Data in H_2O (□) Data in D_2O. Mol. Wt. of NaPA = 950 KDa. The straight lines indicate fits according to eq. 2.51. (adopted from ref. [99])

2.3.4 Phase boundary of polyacrylates- Dependence on size of bivalent cation

A relevant study for Ca^{2+}, Sr^{2+} and Ba^{2+} ions (in order of increasing size) is reproduced in fig. 2.20. All samples are at pH 9 with an initial inert salt concentration of 0.01 M. The phase boundaries are established by measuring samples through SLS and DLS along route 1. The NaPA had a molecular weight of 3300 KDa.
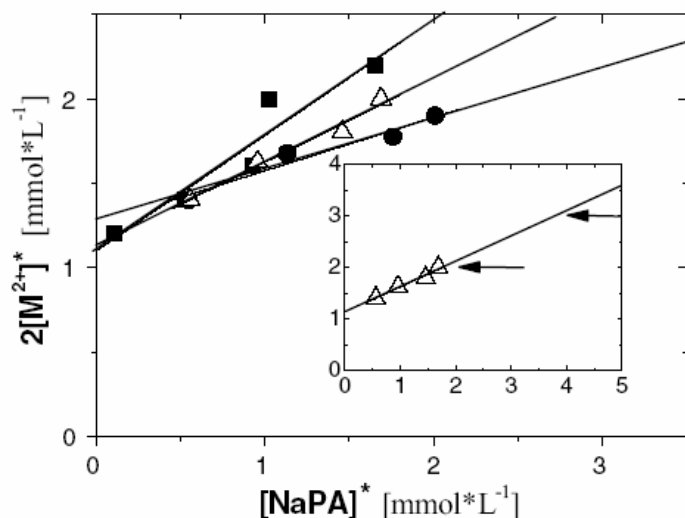
Figure 2.20: (■) CaPA phase boundary (Δ) SrPA phase boundary (●) BaPA phase boundary in 0.01 M NaCl solution at pH 9. Mol. Wt. of NaPA = 3300 KDa. For better clarity, the phase boundary of SrPA is shown by itself in the inset. The arrows just indicate approach along route 1. The straight lines indicate fits according to eq. 2.51. (adopted from ref. [101])

From fig. 2.20, it becomes clear that larger the bivalent cation, smaller is its stoichiometric amount required to precipitate NaPA. The exact reason for this behavior is unknown but must be strongly correlated with the chemical nature of the bivalent cation.

2.3.5 Phase boundary of polyacrylates- Increase of temperature from 15°C to 30°C

Fig. 2.21 shows CaPA phase boundaries as they shift with an increase of temperature. All samples are at pH 9 with an initial inert salt concentration of 0.01 M. The phase boundaries are established by measuring samples through SLS and DLS along route 1. The NaPA had a molecular weight of 650 KDa. Fig. 2.21 shows clearly that one-phase region is narrowed if the temperature is increased. Thus, we can have a temperature

induced precipitation and hence also anticipate a temperature induced coil collapse. We shall comment upon the exact reasons in Chapter 6.
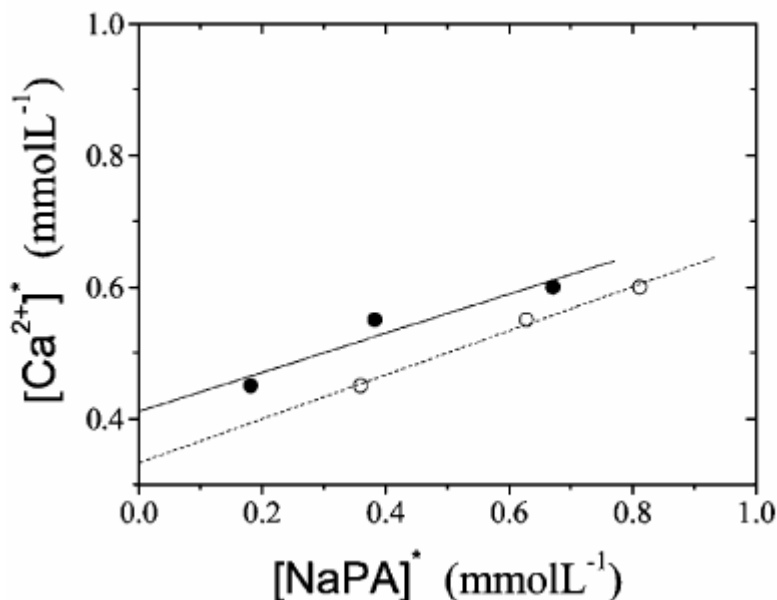
Figure 2.21: CaPA phase boundary in 0.01 M NaCl solution at pH 9 (●) Data at 15°C (○) Data at 30°C Mol. Wt. of NaPA = 650 KDa. The straight lines indicate fits according to eq. 2.51. (adopted from ref. [103])

2.3.6 General comments

All experiments in this thesis were done at a pH of 9 using initial inert salt concentration of 0.1 M with one exception (discussed in the next paragraph). In Chapters 4 and 5, we investigate respectively Sr^{2+} and Pb^{2+} induced collapse transition of NaPA through AFM on surfaces and compare the surface behavior with SLS/SAXS/ASAXS results obtained for solution. Keeping the initial inert salt level at 0.1 M gave us a fairly large one-phase playing field while still maintaining the solvent quality good (refer fig. 2.18). It also makes detection of signals easier during SLS/SAXS/ASAXS measurements.

In Chapter 6, we investigate temperature induced collapse transition of NaPA in the presence of Ca^{2+} ions through AFM on surfaces through AFM on surfaces and compare the surface behavior with SLS/SANS results obtained for solution.. However here the initial inert salt concentration was chosen to be 0.01 M at constant pH 9. This is because

NaPA shows the most drastic coil shrinking in the presence of Ca^{2+} ions when initial inert salt concentration is an order of a magnitude lesser than the 0.1 M applicable to Sr^{2+} and Pb^{2+}. The reasons for this may be diverse including, but not limited to, the chemical nature of the bivalent cations. Since single chain structures in solution and on surfaces are probed though SLS/SANS and AFM respectively, this requires a knowledge of phase boundaries in D_2O rather than H_2O (refer fig. 2.19). Finally, in Chapter 6, a temperature increase from 15°C to 30°C was used to induce a collapse of CaPA at the precipitation threshold (refer fig. 2.21).

Meanwhile, it is noteworthy that at either 0.01 M or 0.1 M initial inert salt concentration and at a pH of 9, we are always below the Manning threshold for counterion condensation. Thus, results can be interpreted without the necessity to invoke counterion condensation.

2.4 From solution to surfaces

As already remarked, the thesis focuses on characterization of intermediate states along the coil to globule transition of polyelectrolytes in solution and subsequently their direct visualization on charged surfaces. When a molecule moves from solution to surface, it is inevitably affected by what is known as "sample history". The term "sample history" is a rather all encompassing phrase often used in literature while trying to qualitatively or quantitatively explain the changes in conformation of a single polyelectrolyte chain as it moves from solution to surface. Our discussion should therefore understandably begin from a description of this very term.

2.4.1 Sample history

We shall divide the term "sample history" into three parts, just for the sake of convenience. In actuality, there need not be any water tight compartmentalization of the three parts described below. The boundaries are blurred and the parts frequently encroach upon each other.

2.4.1.1 Deposition

During the deposition of molecules from surface to solution, the fraction of molecules close to the surface at any time, t is approximately given by[107]

$$\frac{n_{surf}(t)}{n_{sol}(0)} \approx \sqrt{\frac{4D'}{\pi}} t^{1/2} \tag{2.52}$$

where $n_{surf}(t)$ is the number of molecules close to the surface at time, t (molecules per cm²), $n_{sol}(0)$ is the total number of molecules in solution initially, i.e., at time $t = 0$ (molecules per cm³) and D' is the diffusion coefficient.

Eq. 2.52 is valid only if the following conditions are met

(i) The deposition is irreversible

(ii) The deposition is solely governed by diffusion and convection currents do not contribute to the transport of molecules

(iii) The top layer of deposition drop is not significantly depleted of molecules during the time of deposition

(iv) The molecules being deposited are very long (length much greater than thickness)

When either condition (i) or (ii) is not true, $\dfrac{n_{surf}(t)}{n_{sol}(0)}$ is proportional to t rather than $t^{1/2}$.

2.4.1.2 Thermodynamic or kinetic adsorption

There are two driving forces for adsorption: solvent quality[108-110] and substrate-sample interactions. The latter become more important when solvent quality is good, i.e., when solvent does not promote adsorption (which is indeed the case for all experiments in this thesis). These substrate-sample interactions might be purely physical in nature (physi-sorption) or may have a chemical component (chemi-sorption). In the case of physi-sorption, the substrate-sample interactions have electrostatic and van der Waals contributions (van der Waals forces include permanent dipole-permanent dipole, permanent dipole-induced dipole and induced dipole-induced dipole forces. The last term is often called London dispersion forces). In the case of chemi-sorption, covalent bonds play the dominant role in binding the molecule to the substrate. In principle, two extreme cases can be described irrespective of the nature of adsorption.

(i) Thermodynamic adsorption is said to have occurred when the molecules freely equilibrate on the surface before they are captured in a particular conformation. The molecules on the surface represent an ensemble of the lowest energy conformations of molecules existing in a 2D space.

(ii) Kinetic adsorption is said to have occurred when the molecules adhere without having equilibrated on the substrate, and the resulting conformation resembles a projection of the actual 3D conformation onto the surface.

2.4.1.3 Solvent evaporation

After adsorption of the molecules on the surface, the solvent is removed for conducting AFM imaging. In our case this was done using a N_2 flux. The flux instantaneously removes the solvent but also generates two powerful forces. The first one is shear which

acts in the direction of flux. It tends to align the adsorbed molecules in the direction of flux. The second one is a kind of capillary force which results from evaporation of the solvent. It tends to shrink the adsorbed molecules. Both these forces become increasingly important when interactions between the molecules and the substrate are weak.

Having described the powerful forces acting at the substrate-sample interface under the term "sample history", we must mention that "sample history", though quite dominant, is not the sole criterion governing the shape of polyelectrolytes on surfaces.

2.4.2 The role of entropy

The loss of one degree of freedom as the molecule moves from 3D solution to 2D surface drastically reduces the number of configurations that the molecule can access within the range of the thermal energy. It implies that the adsorption process is entropically disfavored. For weakly charged (flexible) chains, this repulsive entropic contribution comes from the inherent chain elasticity. On the other hand, for strongly charged (semi-rigid) chains, the repulsive entropic contribution comes from bending fluctuations. Balancing the repulsive entropic contributions and the attractive electrostatic contributions (attractive assuming the surface is oppositely charged to the molecule) and minimizing the adsorbed chain free energy, we can get the thickness of the adsorbed chain (see fig. 2.22). Ofcourse, in doing so, we are also assuming that electrostatic forces dominate over van der Waals and other forces.
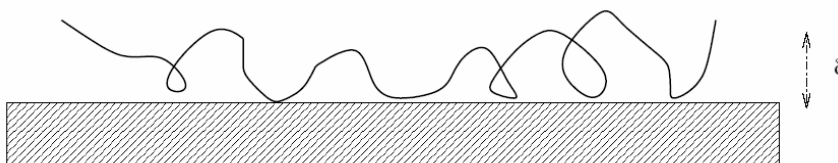
Figure 2.22: The thickness of an adsorbed polyelectrolyte chain (adopted from ref. [111])

For flexible chains, the thickness of adsorbed chain is given by[112]

$$\delta = \left(\frac{b^2}{f \sigma \lambda_B} \right)^{1/3} \tag{2.53}$$

where δ is the thickness of the adsorbed chain, b is the monomer size, f is the fraction of charged monomers, σ is the surface charge density and λ_B is the Bjerrum length.

When salt is added to the aqueous solution, the electrostatic interaction close to the surface is screened. The conformation of the adsorbed chain does not change as long as the Debye screening length, λ_D is larger than the thickness, δ. If the Debye screening length becomes shorter than the thickness, the chain no longer adsorbs.[113] This gives the criterion for adsorption[112]

$$\sigma > \left(\frac{b^2}{f \sigma \lambda_B} \right) \frac{1}{\lambda_D^3} \tag{2.54}$$

In line with eq. 2.53, for semi-rigid chains, the thickness of adsorbed chain is given by[114]

$$\delta = \left[\left(\frac{f \sigma \lambda_B}{b} \right) l_{eff}^{1/3} \right]^{-3/5} \tag{2.55}$$

In eq. 2.55, we have introduced a new term called effective persistence length, l_{eff}. This is different from electrostatic persistence length mentioned in the prologue to section 2.1.4 in the context of OSF perturbation calculations. The effective persistence length includes both electrostatic and bare bending contributions.

When salt is added, a semi-rigid chain also desorbs when the Debye screening length is of the order of chain thickness[113] and this gives the criterion for adsorption[114]

$$\sigma > \left(\frac{b}{f \lambda_B l_{eff}^{1/3}} \right) \frac{1}{\lambda_D^{5/3}} \tag{2.56}$$

Finally, a word of caution. Entropic contributions need not be always repulsive. Release of condensed counterions back into the solution can result in substantial translational entropic gain for the counterions. The corresponding free energy gain can be as large as the direct electrostatic interaction and thus, is a major driving force for the adsorption.

2.4.3 The role of dielectric discontinuity

In section 2.4.2, electrostatic interactions were simply assumed to be attractive. However, in most experimental situations, despite the fact that polyelectrolyte is adsorbed on an oppositely charged surface, the electrostatic interactions, though still attractive on the whole, are found to be drastically reduced than one would predict. This is due to the presence of a competing repulsive electrostatic interaction whenever dielectric constant of the substrate is less than dielectric constant of the solvent. It turns out that dielectric constant of the substrate is less than dielectric constant of the solvent for any experiment in which adsorption of polyelectrolytes from aqueous solutions onto mica, silicon or glass substrates has been carried out. Indeed, this is the case for all experiments in this thesis. This repulsive electrostatic interaction between a polyelectrolyte and an oppositely charged surface of a lower dielectric constant can be of the order of adsorbed chain self energy. (There are no competing interactions when dielectric constant of the substrate is more than dielectric constant of the solvent. This, for example, is the case of adsorption of polyelectrolytes from aqueous solutions onto metallic substrates. But we shall not discuss this case because of its irrelevance for this thesis).

Let $D1$ be the dielectric constant of the substrate and D be the dielectric constant of the solvent such that $D1 < D$. When the polyelectrolyte chain while still in solvent comes very close to the substrate, it "sees" three types of electrostatic forces. A precise

evaluation of electrostatic forces acting at a dielectrically discontinuous interface requires

the invoking of the concept of "image" charge. This is depicted in fig. 2.23. Accordingly,

the first type of electrostatic force is the attraction between the polyelectrolyte chain and

the oppositely charged substrate plus an exactly equal attractive force between the

"image" of the polyelectrolyte chain and the oppositely charged substrate. The second

type of electrostatic force is the repulsion between the polyelectrolyte chain and the

already adsorbed polyelectrolyte chains plus an exactly equal repulsive force between the

"image" of the polyelectrolyte chain and the already adsorbed polyelectrolyte chains. The

third type of electrostatic force is again a repulsion arising due to interactions between the

polyelectrolyte chain and its "image". It is this third type of electrostatic force which

drastically reduces the net electrostatic attraction between the polyelectrolyte chain

adsorbed from solution and the substrate with lower dielectric constant.
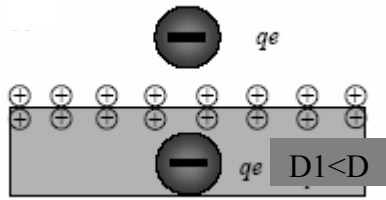
Figure 2.23: Schematic representation of a test charge qe near a charged substrate with dielectric constant $D1 < D$. (adopted from ref. [115])

The electrostatic energy of an adsorbed 2D cell containing a single chain taking into

account all three contributions can be written as[115]

$$\frac{U_{cell}}{kT} \approx S\lambda_B\lambda_D fN\left[\frac{2fN}{R^4}\exp\left(-\frac{R}{\lambda_D}\right) - \frac{2\sigma}{R^2}\right] + \frac{S\lambda_B f^2 N^2}{R_e R^2} \tag{2.57}$$

In writing eq. 2.57, we have used the cell model for polyelectrolyte adsorption from dilute solution containing an added salt. The cell model in dilute regime as well as the meaning of eq. 2.57 is described below.

In the cell model for dilute regime, each adsorbed polyelectrolyte chain of size R_e (end to end distance) is contained within a circular 2D cell of radius, R ($R >> R_e$). The distance between chains on surface is then given by R. The total area of the adsorbed layer, S is the sum of all the 2D cell areas. U_{cell} represents the energy of one such 2D cell. A single 2D cell is shown in fig. 2.24.
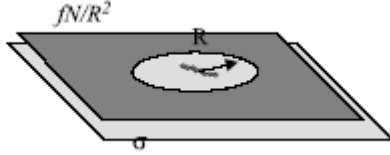
Figure 2.24: Schematic representation of an adsorbed 2D cell in dilute regime (adopted from ref. [115])

The electrostatic repulsion between the polyelectrolyte chain or its "image" and the already adsorbed polyelectrolyte chains is due to effective charge density of the adsorbed layer, efN/R^2 where f is the fraction of charged monomers and N is the degree of polymerization of the chain. The electrostatic attraction between the polyelectrolyte chain or its "image" and the oppositely charged substrate is due to surface charge density, σ of the substrate. In eq. 2.57, the first and the second terms within the square brackets represent these two contributions respectively. The term outside the square bracket represents the electrostatic repulsion between the polyelectrolyte chain and its "image".

U_{cell} given by eq. 2.57 can be minimized with respect to R, the inter chain separation on surface. This gives us

$$\frac{fN}{R^2}\exp\left(-\frac{R}{\lambda_D}\right)\left(1+\frac{R}{4\lambda_D}\right) \approx \sigma - \left(\frac{f}{U_{cell}}\right)^{1/3}\left(\frac{1}{2b\lambda_D}\right) \qquad (2.58)$$

When the amount of salt in the solvent is low, $R/\lambda_D << 1$ in which case $\exp(-R/\lambda_D) \approx 1$.

Thus, for low salt limit, we can evaluate σ from eq. 2.58 and put it in eq. 2.57 to obtain

$$\frac{U_{cell}}{kT} \approx -\frac{\lambda_B f^2 N^2}{2R} \tag{2.59}$$

The negative sign in eq. 2.59 shows net attraction, but nevertheless, made much lesser because of strong repulsions between the polyelectrolyte chain and its "image".

Also note that the substrate is always undercharged in such cases as is shown below. The net charge on the substrate is given by the difference

$$\Delta\sigma \approx \sigma - \frac{fN}{R^2} \approx \frac{1}{b\lambda_D}\left(\frac{f}{U_{cell}}\right)^{1/3} \tag{2.60}$$

In eq. 2.60, since U_{cell} is negative (as shown by eq. 2.59), $\Delta\sigma$ is also negative which means undercharging.

2.4.4 Conformation in solution vs. conformation on surface

It has always been tempting to compare solution and surface conformations of adsorbed molecules in a bid to quantize the effects of sample history. We may classify two limiting cases based upon whether adsorption is strong or weak.

The first limiting case provides a scenario when adsorption of the molecules on surfaces is rather strong. A case in point is one of the previous studies by Stamm et al.[116] regarding the formation of intermediate states along the coil to globule transition of poly(methacryloyloxyethyl dimethylbenzylammonium chloride) (PMB) in pH 3 aqueous solution induced by additions of Na_3PO_4 salt. The intermediate states were visualized by adsorbing them on mica surfaces. PMB is a strong cationic polyelectrolyte with a sufficiently bulky backbone for which water acts as a poor solvent. Thus, it adsorbs strongly on mica surfaces. All experiments could be conducted at pH 3 (near isoelectric

point of mica) so that charge density of mica surfaces did not play any role. It could be speculated by the authors that the polyelectrolyte undergoes a z collapse but does not get noticeably altered in the x and y directions, even after flux drying. In fact, they reported a nearly 1:1 correlation between end to end distances in solution and on surfaces. Later, Minko et al.[117] used this very system to provide the first qualitative glance into how sample history may affect surface conformations. The latter authors found that AFM scans produced under a fluid cell and those produced in air (flux dried) were substantially different. The response of the polyelectrolyte coil towards formation of an intermediate state was a bit delayed under fluid cell environment.
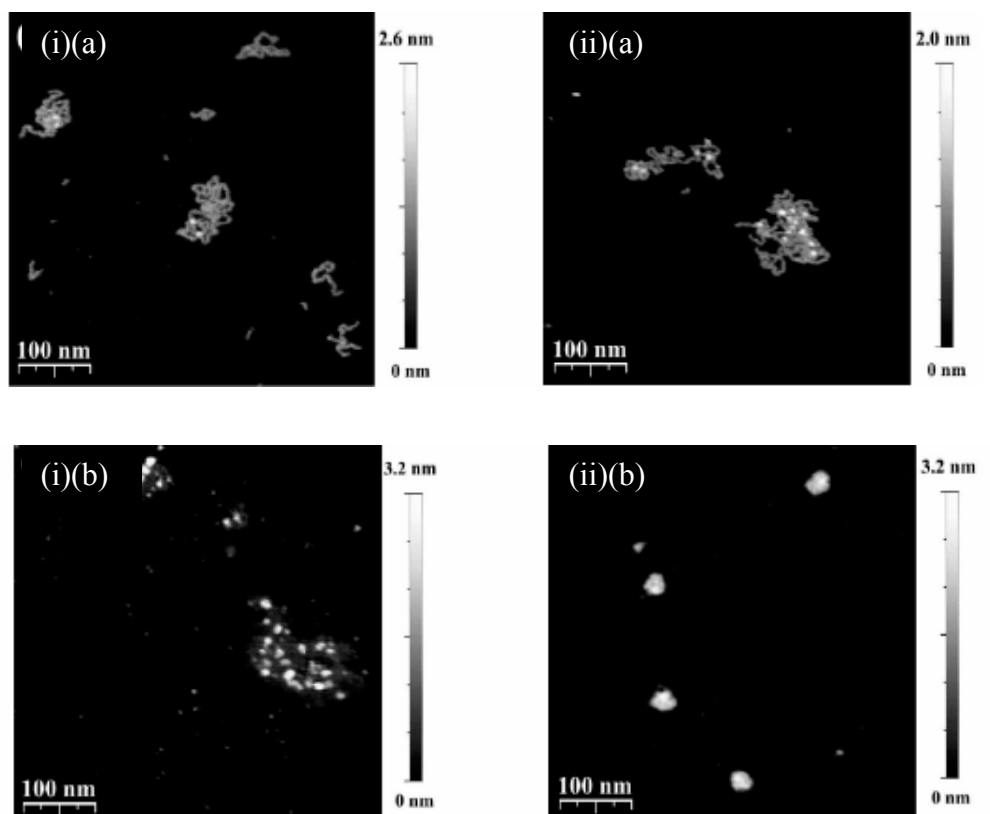
Figure 2.25: AFM images of single PMB molecules adsorbed from 5 x 10^{-4} g/L aqueous solution at pH 3 containing (i) 8mM Na_3PO_4 salt- (a) AFM images under fluid cell (b) AFM images after solvent was removed using N_2 flux (ii) 24mM Na_3PO_4 salt- (a) AFM images under fluid cell (b) AFM images after solvent was removed using N_2 flux. (adopted from ref. [117])

At 8 mM Na_3PO_4 concentration, for example, AFM scans under a fluid cell showed little to no signs of pearl growth with most of the molecules being random coils while those produced in air showed a highly compact pearl necklace morphology. Similarly, at 24 mM Na_3PO_4 concentration, AFM scans under a fluid cell showed a pearl necklace morphology while those produced in air showed a non resolvable compact globule like morphology. The authors speculated that van der Waals interactions associated with the substrate-sample interface stabilize the polyelectrolyte coil in the fluid cell environment. Fig. 2.25 reproduces their findings

A second example of strong adsorption may be cited. Rivetti, Guthold and Bustamante[118] studied DNA adsorption on glow discharged or H^+ exchanged mica. They observed that the square of end to end distances on surfaces for long chain DNA segments were nearly two-thirds of the square of end to end distance in solution, i.e.,

$$\langle R^2 \rangle_{proj} = \frac{2}{3} \langle R^2 \rangle_{3D} \tag{2.61}$$

where $\langle R^2 \rangle_{proj}$ is the mean square end to end distance on surface and $\langle R^2 \rangle_{3D}$ is the mean square end to end distance in solution.

The second limiting case provides a scenario when adsorption of the molecules on surfaces is weak. To cite an example, Borkovec et al.[119] observed necklace like intermediates with poly(vinylamine). In the latter experiment a direct discharge of the respective poly(vinylammonium) salt was achieved by decreasing the pH. A low molecular weight of poly(vinylamine), a weak cationic polyelectrolyte, was chosen for imaging on mica surfaces, in a marked departure from preceding works.[116-118] Although the authors do mention the role of sample history, they stop short of comparisons with solution conformations of the same coils.

2.4.5 General comments

In this thesis, the structure of intermediate states on surfaces have been compared quantitatively to those in solution for all the experiments. The polyelectrolyte used is a *non bulky*, *low molecular weight* (Chapter 4- 1.13 Million g/mole as measured by SLS in the presence of 0.1M NaCl as an inert electrolyte, Chapter 5- 456,000 g/mole as measured by SLS in the presence of 0.1M $NaNO_3$ as an inert electrolyte, Chapter 6- 783,000 g/mole as measured by SLS in the presence of 0.01M NaCl as an inert electrolyte), *weakly charged*, *anionic* polyacrylate coil for which water acts as a *good solvent*. The reader must recognize by now that we are essentially trying to emphasize the anticipated weak adsorption on (negative) mica surfaces where sample history plays a major role. To quantize the effects of sample history, we have used radius of gyration, apart from several other chain statistics, for direct comparison with light scattering data of the very same sample solutions. The radius of gyration evaluated for surface features is a kind of 3D shape parameter for the adsorbed molecules. We will have more to say on that in Appendix A. In chapter 6, a thorough analysis in reciprocal space, apart from radius of gyration, has been carried out for AFM images to give an alternative quantification method of the changes in conformations of intermediate states on surfaces as compared to those in solutions.

Throughout, it has been our effort to trap molecules kinetically on the surface. For this, modified mica surfaces (recharged using $LaCl_3$) were generally used. In Chapter 5, chemical modification of mica surfaces (using 3 aminopropyl dimethyl ethoxy silane) was carried out successfully. In Chapter 6, both chemically modified and salt-treated mica surfaces have been used.

Experimental procedures

3.1 Materials

The sodium polyacrylates were purchased from Polysciences GmbH (Eppelheim, Germany) and were characterized in-house for weight averaged molecular weight and z-averaged radius of gyration determination using SLS. Inert salts, NaCl (Chapter 4 and Chapter 6) and $NaNO_3$ (Chapter 5) were of analytical grade and purchased from Sigma-Aldrich (Taufkirchen, Germany). Specifically binding salts, dry $SrCl_2$ (Chapter 4), dry $Pb(NO_3)_2$ (Chapter 5) and dry $CaCl_2$ (Chapter 6) of analytical grade were purchased from Sigma-Aldrich (Taufkirchen, Germany). The pH of all samples was set to 9 using NaOH (Chapter 4 and Chapter 5) and NaOD (40% w/w in D_2O) (Chapter 6) purchased from Sigma-Aldrich (Taufkirchen, Germany). D_2O was purchased from Deutero GmbH (Kastellaun, Germany) and was used without further purification.

For modification of mica surfaces, dry $LaCl_3$ of analytical grade was purchased from Sigma-Aldrich (Taufkirchen, Germany). Chemical modification of mica surfaces was carried out using 3 aminopropyl dimethyl ethoxy silane (97% purity) from ABCR GmbH (Karlsruhe, Germany). Toluene and sodium (>99% purity in terms of trace metals) were of analytical grade and purchased from Arcos Organics (New Jersey, USA) and Merck Schuchardt OHG (Hohenbrunn, Germany) respectively. PTFE filters (0.2 µm) were used to remove any dust particles in solutions and were purchased from Carl Roth GmbH (Karlsruhe, Germany). Temperature of the samples and substrates was set to desired values using a standard Type E 200 water thermostat from Lauda-Dr. R. Wobser GmbH (Königshofen, Germany).

3.2 Trapping of intermediate states on mica surfaces

In Chapter 2, section 2.4.1.2, we commented upon two extreme cases of polymer adsorption on surfaces. Thermodynamic adsorption is said to have taken place when molecules freely equilibrate on the surface before being trapped in a particular conformation. On the other hand, kinetic adsorption refers to a condition when the molecule is trapped before it gets a chance to laterally equilibrate on the surface. It is however fully justified to ask whether the conformation on surface represents a completely relaxed state or not. Notwithstanding, any study (including this one) which aims at comparing surface conformations with solution conformations tries to achieve kinetic trapping of molecules. Instantaneous trapping of negatively charged polyelectrolytes (polyacrylates in this case) on (negatively charged) mica surfaces can be a tricky process and requires careful surface modification procedures. On one hand, the adsorption should be strong enough so as to exclude the possibility of shear fields during drying procedures. On the other hand, a very strong adsorption force might change the surface conformation of adsorbed molecules. Two modification methods of freshly cleaved mica surfaces have been widely used, with salts and with silanes. Each technique has a few advantages as well as disadvantages. Depending upon the objective of the experiment, we have tried both.

3.2.1 Modification of mica surfaces using salts

Modification of freshly cleaved mica surfaces using salts has been earlier tried for adsorption of biomolecules like DNA.[120-126] Most probably, such salt pretreatment leads to a recharging of mica surface eventually preparing the surface for instantaneous trapping of negatively charged polyelectrolytes. We use the term "most probably" to

indicate that the physical chemistry behind such modifications is far for being clearly understood.[127-129] In a series of experiments, different salt solutions were used to treat freshly cleaved mica surfaces. Different concentrations of the same salt solution were tried and the exposure time of mica surfaces to such salt solutions was also varied. All these variables affect the adsorption force between the polyacrylate and the mica surface. In each case, AFM scans of adsorbed polyacrylates were studied.

We found out that in our case, the best results were obtained when freshly cleaved mica surfaces were treated with an aqueous solution of 0.01 g/L $LaCl_3$ for 1 minute after which the salt solution was blown off using N_2 flux. The sample solution was then adsorbed on this pretreated mica surface for 2-3 seconds and again blown off using N_2 flux.

3.2.2 Modification of mica surfaces using aminosilanes

Chemical modification of freshly cleaved mica surfaces has been cited as a fairly established surface modification technique for adsorption of biomolecules like DNA.[130-132] The technique was used to study structures of intermediate states on surfaces in Chapter 5 and with partial success (as an alternate procedure to salt pretreatment) in Chapter 6. Humidity control is extremely important during silanization (the most common of chemical modifications) of mica surfaces as silanized surfaces degrade quickly, even under atmospheric humidity. The silanes customarily used for such chemical modifications have been both monofunctional like 3-glycidoxypropyl dimethyl ethoxy silane[119] and multifunctional like 3-glycidoxypropyl trimethoxy silane[119] or 3-aminopropyl triethoxy silane.[130-131] In our case, chemical modification was carried out using 3-aminopropyl dimethyl ethoxy silane (APDMES). It is an example of a monofunctional amino silane. The quality of mica surfaces chemically modified with

multifunctional silanes has been reported to be quite sensitive to ambient humidity.[131]

Depending upon the exact chemical modification procedure followed, AFM scans of

mica surfaces modified with multifunctional silanes have shown formation of large

aggregates.[130] These aggregates are speculated to be condensation products resulting from

the silanization process itself.[119] In the latter case, it becomes quite difficult to

differentiate between condensation products formed on the surface of mica as a result of

silanization and actual aggregates from the polyelectrolyte specie under investigation.[119]
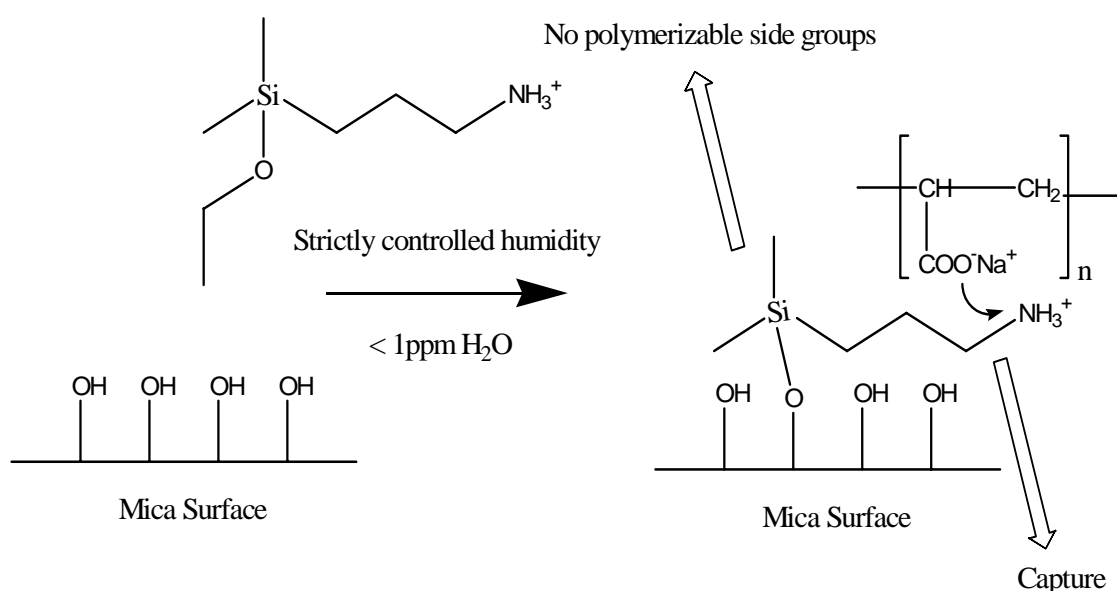
Figure 3.1: Schematic showing the probable binding of polyacrylate to APDMES modified mica. APDMES lacks reactive side groups for condensation reactions.

APDMES was a suitable choice because it lacks reactive side groups which reduce the

chances of side condensation reactions. We expected APDMES to chemically bond with

hydroxyl groups of mica on one end and capture the negatively charged polyacrylate on

the other using its hydrolysable ethoxy and amino groups respectively. The schematic is

shown in fig. 3.1. We were indeed successful in producing a lot of representative AFM

images using mica surfaces modified with APDMES. 20 µl of 0.01 % (V/V) APDMES-

Toluene solution was dropped on freshly cleaved mica and allowed to evaporate under glove box conditions (Oxygen < 1 ppm, Water < 1 ppm). The surface was washed several times under laboratory hood conditions using dry (refluxed over Na) Toluene filtered previously through a filter of pore size 200 nm. The sample solution was then adsorbed on this pretreated mica surface for 2-3 seconds and again blown off using N_2 flux.
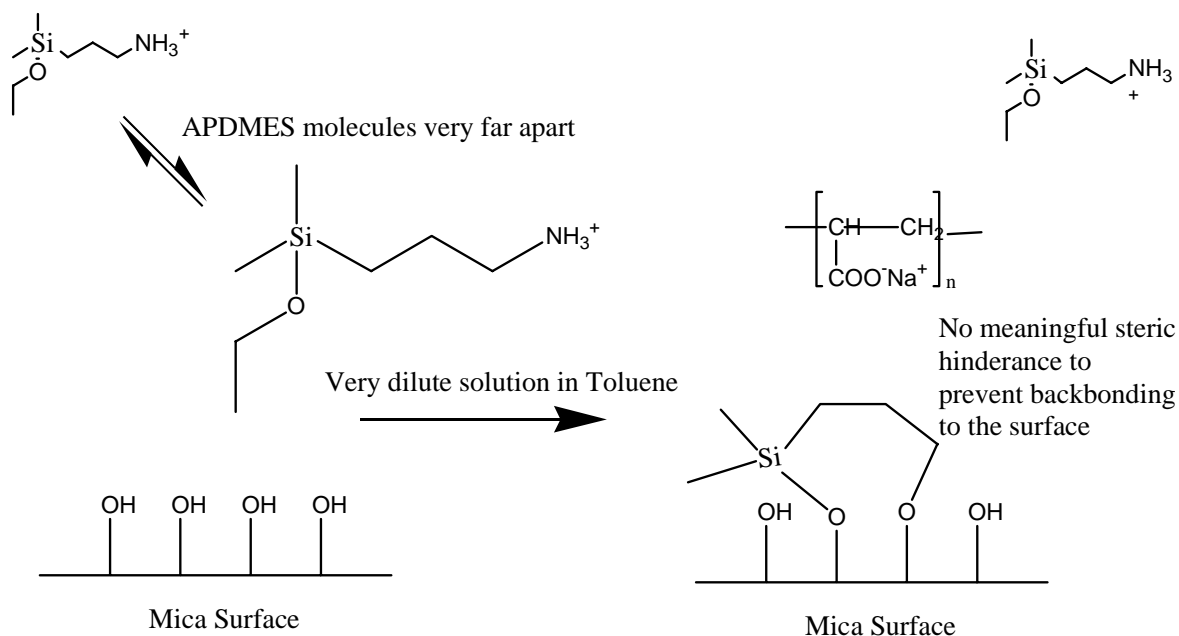
Figure 3.2a: Schematic showing the preferential backbonding of APDMES to the mica surface at "critically" low APDMES-Toluene concentrations.
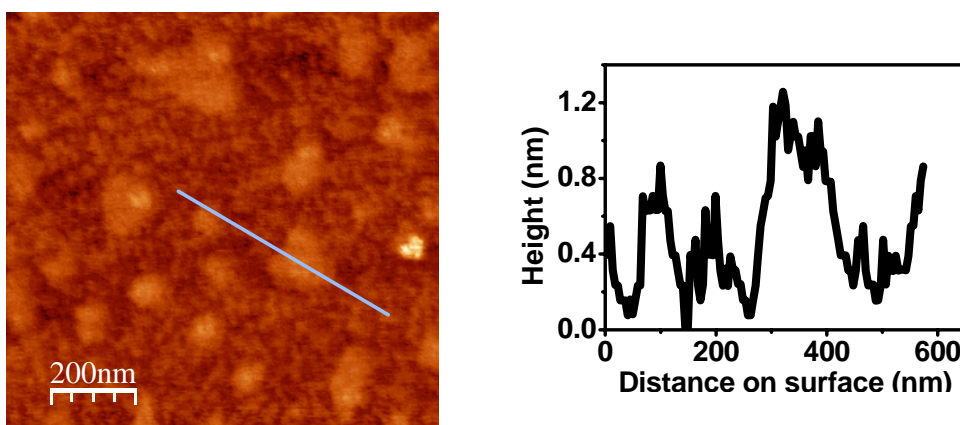
Figure 3.2b: An exemplary AFM scan where a suspected backbonding has occurred. On the right is shown the lateral height profile taken along a line on the surface. The volume ratio of APDMES-Toluene was 0.001 % V/V. No polyacrylate gets adsorbed.

The concentration mix of APDMES-Toluene (0.01 % V/V) was carefully chosen. At lower concentrations, APDMES showed a tendency to backbond to the mica surface instead of binding to the polyacrylate. The schematic is shown in fig. 3.2a and an exemplary AFM scan along with the height profile in fig 3.2b.

At the same time, higher concentrations of APDMES-Toluene led to the overcrowding of mica surface with adsorbed polyacrylates and loss of single molecular resolution.

3.2.3 Kinetic trapping of molecules equilibrated at a particular temperature

In Chapter 6, we have analysed temperature induced collapse of NaPA-Ca^{2+} system both in solution and on surfaces. Molecules from the solution equilibrated at a particular temperature were adsorbed on to pretreated mica surfaces equilibrated at the same temperature. For this purpose, a hollow aluminium tubelet was designed through which water from a thermostat could flow. The mica surfaces pretreated with LaCl$_3$ as well as with APDMES were glued to the outer part of the hollow aluminium tubelet. The thermostat was set to the desired temperature. The sample solutions to be adsorbed were also equilibrated at the same temperature independently. After equilibration of both the sample solution and the pretreated mica surface had been achieved at a particular temperature, a drop of sample solution was adsorbed on the pretreated mica surface for 2-3 seconds and successively removed using N$_2$ flux.

3.3 AFM imaging

AFM-TM experiments were performed in dry state with an AFM instrument Multimode (Digital Instruments, Santa Barbara, USA). The Multimode was operated with amplitude feedback and in a "light" tapping mode configuration. The amplitude setpoint was set to the maximum possible value. Silicon tips with a spring constant of 0.3 N/m and a

resonance frequency of 250-300 KHz were used after calibration with gold nanoparticles

(of diameter 5.22 nm) to evaluate the tip radius. The tips with radius 14.9 +/- 1.9 nm were

used for most measurements.

Single phase behavior of sodium polyacrylate in presence of strontium

4.1 Introduction

In this Chapter, we investigate the on-surface collapse behavior of NaPA induced by Sr^{2+} as specifically binding ions and compare it with the corresponding behavior in solution. A complete picture for the single phase region has been drawn as shall be shortly outlined. The substrates for AFM were prepared using $LaCl_3$ as discussed in Chapter 3, section 3.2.1. The reference sample (A), i.e., the sample without any Sr^{2+} ions contained 0.1M of inert salt, NaCl. Its weight averaged molecular weight was found to be 1.13 million g/mole by means of SLS. The concentration of NaPA used was 0.1 g/L. The phase boundary was gradually approached by replacing Na^+ ions with stoichiometric amounts of Sr^{2+} ions while keeping the total concentration of positive charges constant. The advantages of this methodology have been discussed in length in Chapter 2, section 2.3. Along this route (identifiable as route 2 mentioned in Chapter 2, section 2.3) two samples (B and C) were prepared with the same concentration of NaPA as the reference sample but with progressively increasing Sr^{2+} concentration. At the phase boundary, we were able to identify two more samples (D and E) which showed a very drastic decrease in coil dimensions (investigated by combined SLS and DLS) upon subtle variations in Sr^{2+} ion concentration. These two samples represented intermediate states along the coil to globule transition of NaPA induced by Sr^{2+} ions. Hence they were analysed in detail using SLS and SAXS in solution and AFM on surfaces. Finally, two more samples (F and G) were prepared which represented a departure from the phase boundary along route 1 (refer again Chapter 2, section 2.3). The pH of all samples was set to 9. The schematic is shown in fig. 4.1.
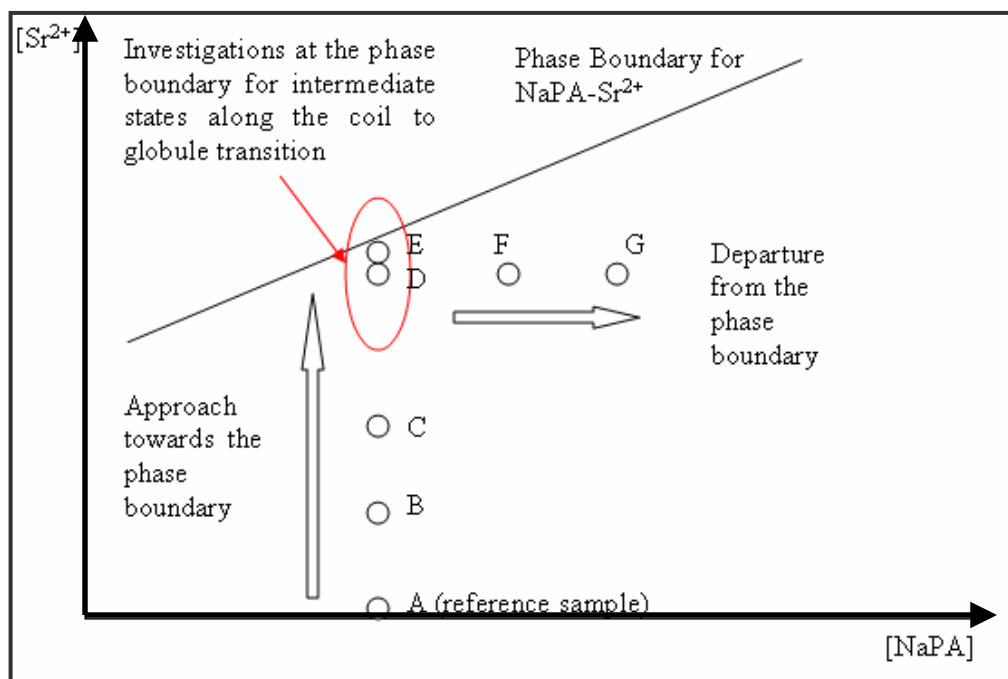
Figure 4.1: Schematic showing the working plan in Chapter 5. Refer text for details of the samples A-G.

AFM supplements scattering experiments in an almost ideal way. It is superior upon any scattering experiment as it presents a direct view of adsorbed polymer coils. Yet, its disadvantage lies in the inevitable effects of sample history, especially in case of weak polyelectrolytes. With these aspects in mind, we will look at the whole single phase region of NaPA-Sr^{2+} system and add information to an important question: How much do the AFM images succeed in evaluating essential features of polyelectrolyte coils on surfaces which the very coils exhibit in solution?

Sample	A	B	C	D	E	F	G
[NaPA] g/L	0.1	0.1	0.1	0.1	0.1	0.3	0.5
[Sr^{2+}] mM	0.00	1.00	2.00	3.40	3.54	3.40	3.40

Table 4.1 : The concentrations of NaPA and Sr^{2+} ions in samples A-G. The position of various samples relative to the phase boundary are given in fig. 4.1.

The concentrations of NaPA and Sr^{2+} ions in samples A-G are tabulated in Table 4.1. The total positive ion concentration was the same in all the samples, at 0.1 M.

4.2 Solution behavior analysed by scattering

Samples other than those at the precipitation threshold (phase boundary) show a marked contrast compared to samples at the precipitation threshold. Combined SLS and DLS experiments did not reveal any kind of sectional collapse associated with the samples A, B, C, F and G. In the reference sample, A, which did not contain any specifically binding ion Sr^{2+}, the coils were largely extended. For samples D and E which were close to the phase boundary, combined SLS and DLS revealed a drastic reduction in coil dimensions. Thus, further SAXS analysis was carried out on these samples. Unfortunately, the separation of the scattering contribution of the condensing Sr^{2+} cations in the ASAXS experiment could not be achieved. Yet, the results indicated presence of partially collapsed coils with sub-domains. The radii of gyration values for samples D and E (evaluated by SLS) are mentioned in Table 4.2.

Sample	[NaPA] g/L	[Sr^{2+}] mM	R_g (SLS) nm
D	0.1	3.40	37.2
E	0.1	3.54	40.1

Table 4.2: The radius of gyration values in samples D and E as evaluated by SLS (courtesy of Lages, S. and Huber, K). These samples were very close to the phase boundary and were investigated for intermediate states along the coil to globule transition.

4.3 Surface behavior analysed by AFM

We shall divide this section into four parts. The first, second and fourth parts, sections 4.3.1, 4.3.2 and 4.3.4, will describe respectively AFM images of the reference sample, the

approach towards the phase boundary and the departure from the phase boundary. It is the third part, section 4.3.3, which is at the core of this Chapter. It deals with AFM images of samples at the phase boundary.

4.3.1 Surface behavior of reference samples without any strontium

The sample A poses the maximum difficulty not only in adsorption but also in achieving molecular resolution. Fig.4.2a shows an exemplary AFM scan. The presence of randomly coiled molecules alongside a few isolated molecules can be seen. Rarely can the randomly coiled molecules be further resolved. It was observed that the lack of a specifically binding ion in the sample inhibits strong adsorption of the (negatively charged) polyacrylate coils on (negative) mica surfaces. We suspect that even after treating mica surfaces with 0.01 g/L $LaCl_3$ solution, the surface is slightly undercharged for strong trapping of the reference samples. Such a scenario does not exclude the possibility of shear fields created during drying procedures making visualization of isolated single molecules difficult. The scan also shows some smaller globule like structures. A volume check verifies that the volume of these structures is significantly less than the single molecular volume of 3000 nm^3 expected for a coil of 1.13 million g/mole assuming its dry state density to be 1g/cc (Appendix A, section A2.3.1.1). Under all probabilities, these small structures are sections of an extended coil, a larger part of which remained invisible to the AFM scan considering the noise levels at which scanning was performed. Fig 4.2b-c show respectively, exemplary height profiles of the molecules trapped as random coils and that of an isolated molecule on the surface. The height profiles fluctuate around the 1 nm mark for either of these cases.
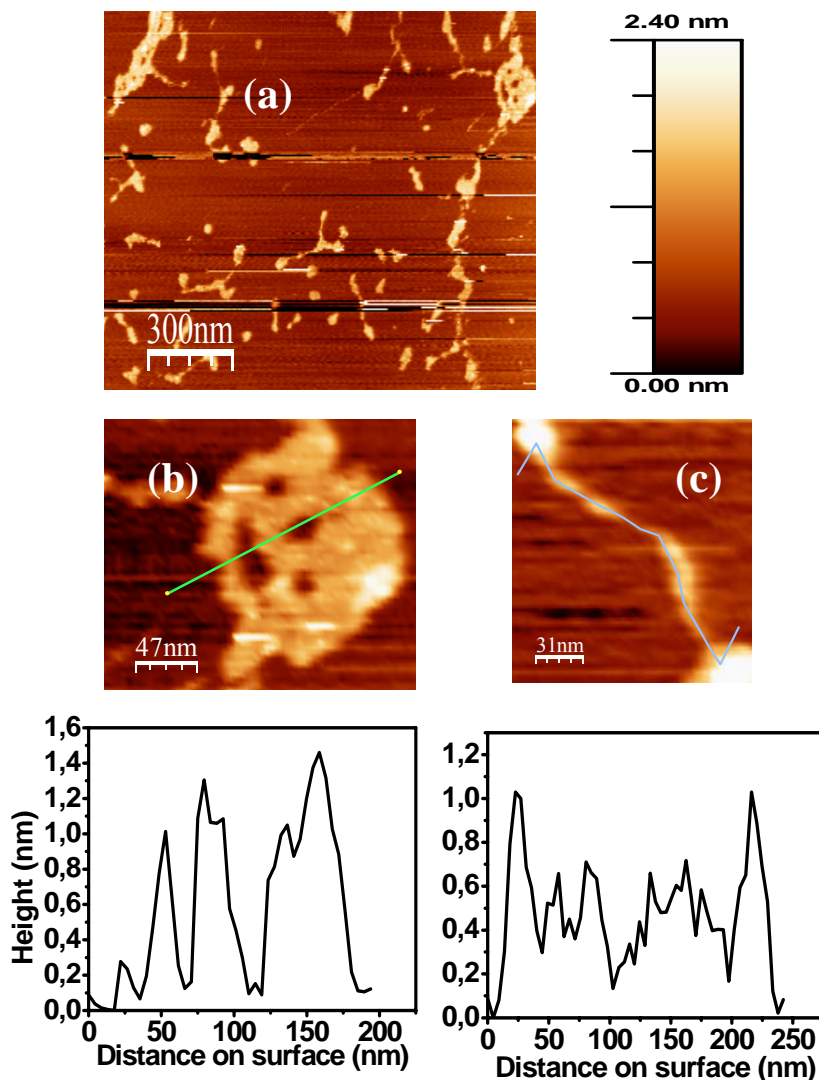
Figure 4.2: (a) An exemplary AFM scan of the reference sample chosen for NaPA-Sr^{2+} system. The sample is 0.1 g/L in NaPA and contains 0.1 M NaCl as an inert salt but no Sr^{2+}. There is no distinct pearl formation along the molecular contour. (b) A zoomed out image of randomly coiled molecules show height profile fluctuating around 1 nm (c) A zoomed out image of an isolated single molecule along with the height profile.

Although AFM scans like the one shown in fig.4.2a are not suitable for statistical analysis, they drive an important point home. The molecules do not show any pearl like structures along the contour. This, as we shall see, is a major difference between surface conformations of NaPA containing sufficient Sr^{2+} and those without any Sr^{2+}, very much in line with what is observed in solution. This is despite the fact that 0.1 M NaCl is present as an inert salt in the reference sample.

Many cases of isolated molecules do show pearl like structures towards the end of the chains. A case in point is fig. 4.2c. The molecule is extended in the middle section but

relaxes towards the end. This is an end effect we discussed in Chapter 2, section 2.1.5. The charges on the chain tend to accumulate towards its end and interact more strongly with (recharged) mica substrates than the middle section. Hence, appearance of pearl like structures towards the end of the chains, with no pearls along the contour, is an indication of an end effect rather than any marked contrast between solution and surface behaviour of the polyacrylates.

4.3.2 Approach toward the phase boundary at constant polyacrylate concentration

Samples, B and C represent the approach towards the phase boundary. Exemplary AFM scans along with the relevant height profiles for sample B are shown in fig. 4.3a-c.

Figure 4.3: (a)An exemplary AFM scan of a sample which is 0.1 g/L in NaPA and contains 1.00 mM Sr^{2+} at a total positive ion concentration of 0.1M. There are no marked differences with respect to the reference sample. (b) A zoomed out image of randomly coiled molecules along with the height profile (c) A zoomed out image of a single molecule along with its height profile

Sample B shows the same behaviour as the reference sample. The surface has non resolvable random molecular coils as well as cases of isolated chains, with at least some chains being partly buried under noise. As with the reference sample, the height profiles fluctuate around the 1 nm mark. The molecules do not show any pearl like structures along the contour but for the presence of end effects. The absence of pearl like structures is completely in line with scattering experiments. Thus, at 1.00 mM Sr^{2+} concentration, the polyacrylate has still not entered the coil to globule transition phase either in solution or on the surface.

The scans of sample C were different. The chains begin noticeably shrinking in size, as also observed in solution. The presence of 2.00 mM Sr^{2+} ions makes adsorption strong. However, random coiling is still observed. We would not unarguably say whether molecules show any sectional collapse at this stage or not due to our inability to visualize single molecules. Very small structures do not represent collapsed molecules, rather sections of a shrinking chain buried under noise. This could again be verified by a volume check. Fig. 4.4 shows an exemplary AFM scan of sample C.
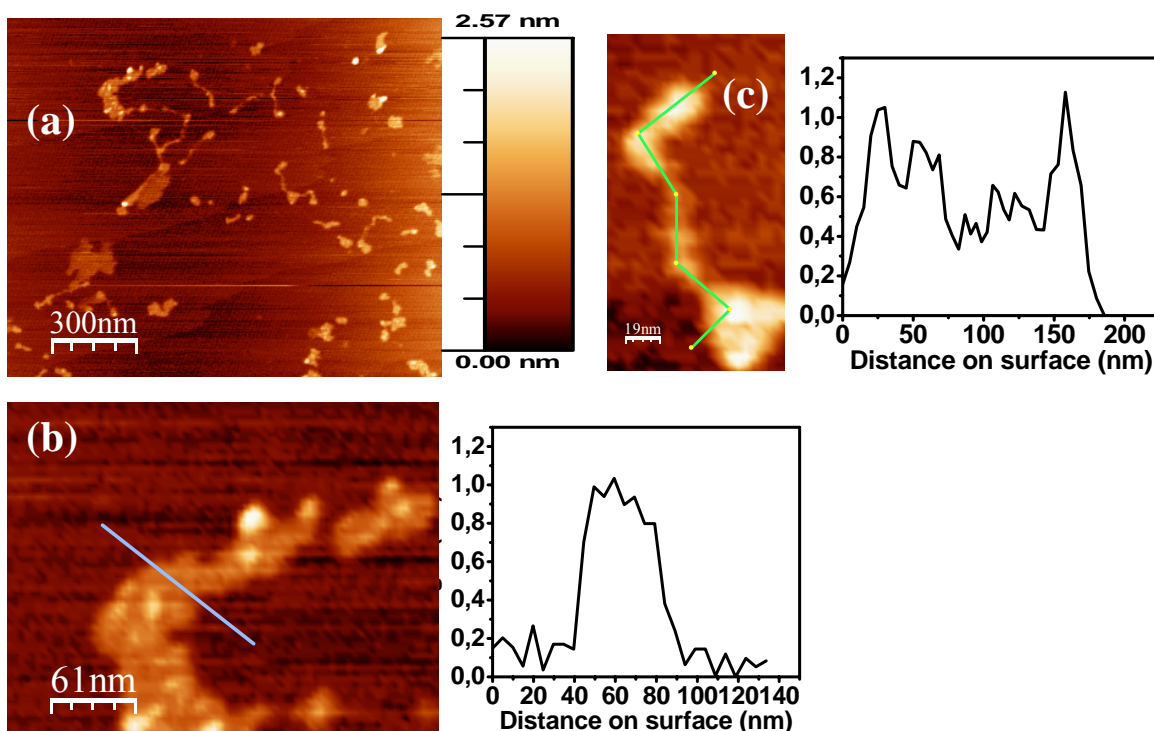

Figure 4.4: An exemplary AFM scan of a sample which is 0.1 g/L in NaPA and contains 2.00 mM Sr^{2+} at a total positive ion concentration of 0.1M. Coils noticeably shrink in size. Adsorption is strong but random coiling still observed.

4.3.3 Investigations at the phase boundary

The situation at the phase boundary is represented by the samples D and E. Combined

SLS and DLS data reveals a drastic collapse of coils in these samples. Hence these represent the intermediate states in solution along the coil to globule transition of polyacrylate coils. The very same samples were adsorbed on mica substrates and subdued to AFM imaging. At 3.40 mM and 3.54 mM of Sr^{2+} respectively, samples D and E strongly adsorb on recharged mica surfaces ensuring an absence of shear fields. This makes collection of data for a statistically significant number of single molecules possible. As we shall see, sectional collapse begins in these samples. Pearl formation in these samples on surfaces is completely in agreement with scattering data for solution behavior. Our aim was to highlight the essential features of these intermediate states on the surface and evolve a parameter which can be directly compared with a corresponding parameter obtained from scattering data of the solution. In line with the first goal, a detailed analysis of AFM images has been carried out. Firstly, all AFM scans of these samples were checked for absence of shear forces and inter-particle correlations using reciprocal space analysis (Appendix A, section A2.3.2.1). These were found to be absent. The situation for both the samples on the surface was similar to the one described by fig. A7 in Appendix A, section A2.3.2.1. Any statistical treatment was done after confirming that molecules adsorbed on the surface were single molecules and not clusters. Thus, volume histograms were the first to be evaluated (Appendix A, section A2.3.1.1). The theoretically predicted volume of a single molecule of molecular weight 1.5 million g/mole (approx.) assuming the dry state density as 1g/cc comes out to be 4000 nm³. Within statistical error, the mean volumes shown by our histograms are slightly higher. Deconvolution to account for the geometry of the tip should bring the experimental values close to the ones theoretically anticipated. Subsequently, various histograms have

been produced representing different characteristics of these intermediate states. The mean values from these histograms have been tabulated. Finally, proceeding along our second goal mentioned above, a 3D shape parameter on the surface, R_g(AFM), is evaluated for both the samples (Appendix A, section A2.3.1.2). It is this parameter which is directly compared to R_g(SLS) and conclusions have been drawn.

Fig. 4.5a-h shows, respectively, an exemplary AFM scan of the sample D along with histograms for single molecular volume, single molecular radius of gyration squared, contour length, number of pearl like structures present per molecule, height of these pearls, height of the molecular contour between two pearls and separation between two pearls. Fig. 4.6a-h shows the same characteristics in the same order for sample E. Finally, Table 4.3 puts all these characteristics in comparison.
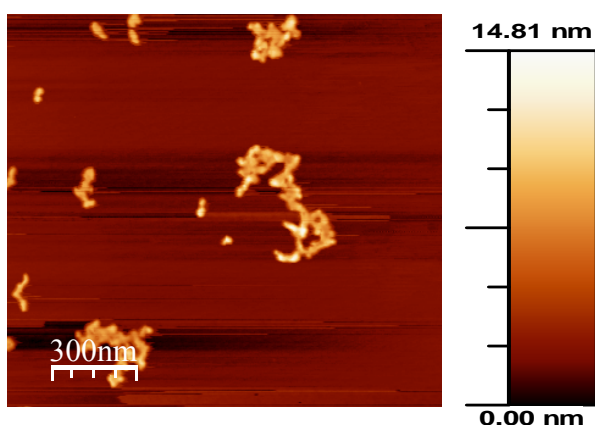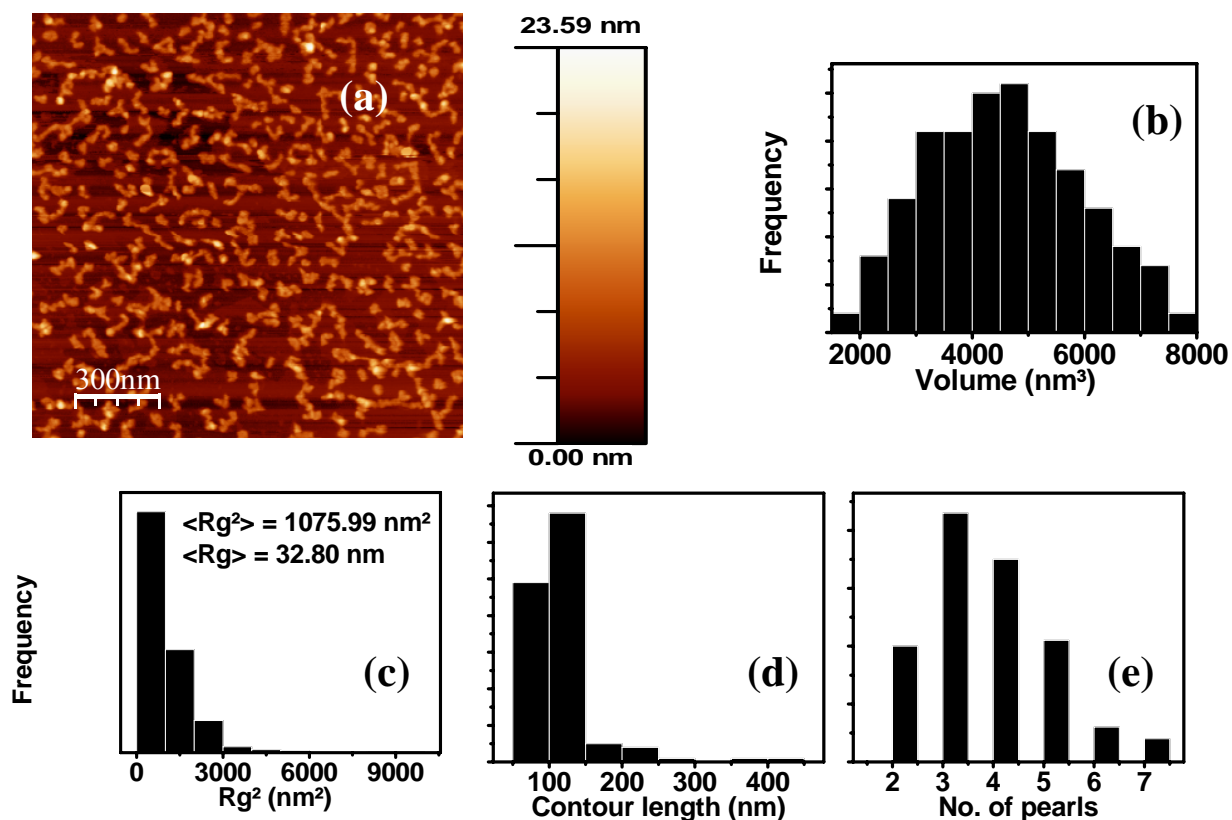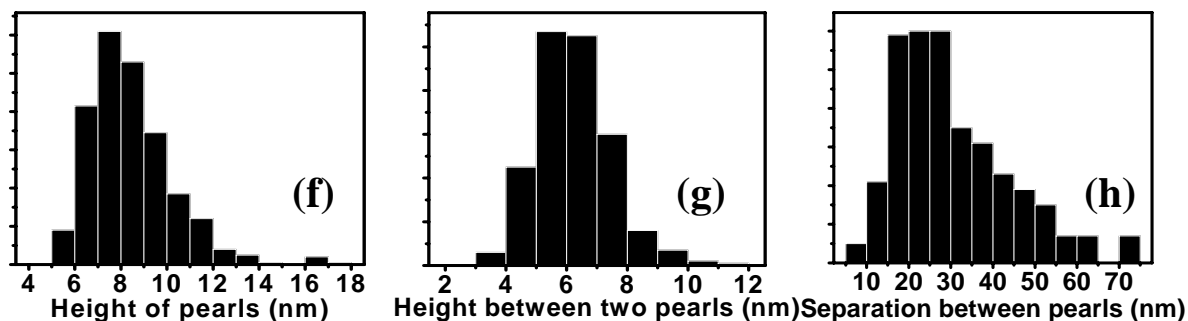
Figure 4.5: (a) An exemplary AFM scan of a sample which is 0.1 g/L in NaPA and contains 3.40 mM Sr^{2+} at a total positive ion concentration of 0.1M. (b) Histogram for single molecular volume (for original scan, not deconvoluted to account for geometry of the tip) (c) Histogram for single molecular radius of gyration squared (d) Histogram for contour length (d) Histogram for number of pearl like structures present per molecule (e) Histogram for height of the pearls (f) Histogram for height of the molecular contour between two pearls (g) Histogram for separation between two pearls.
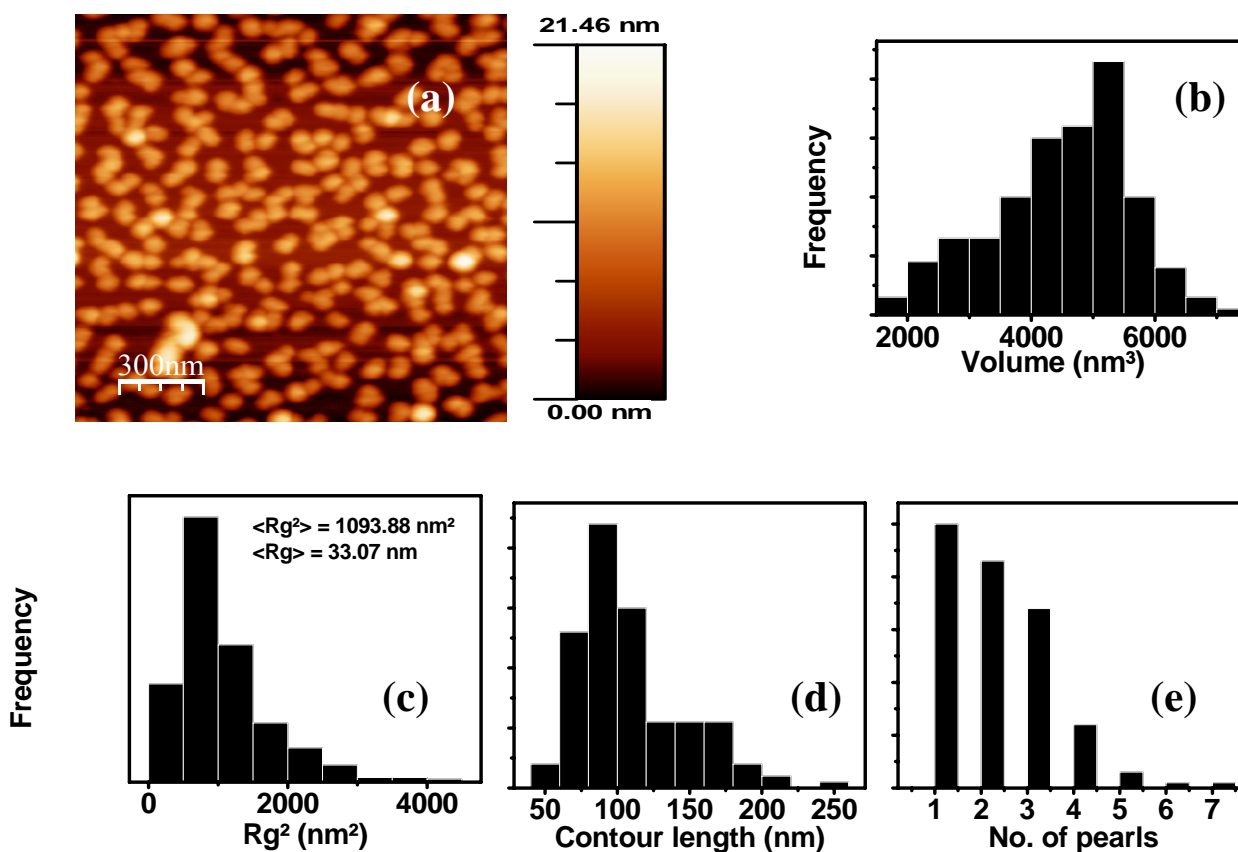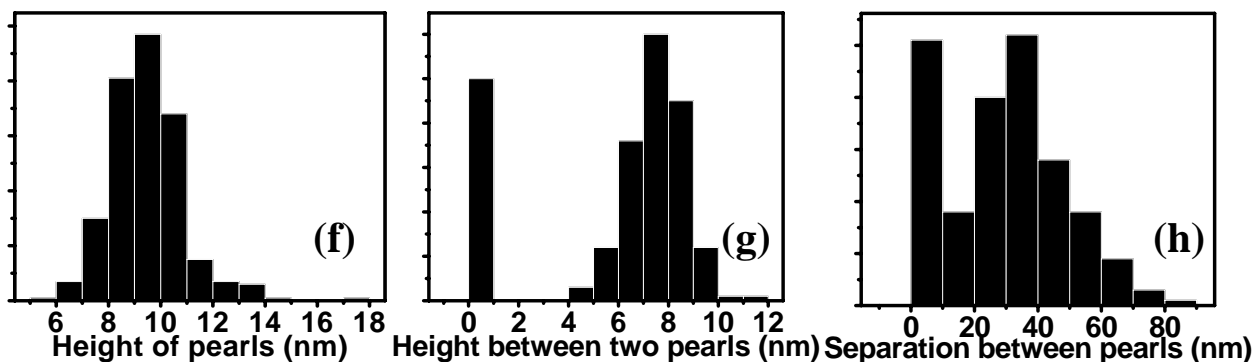
Figure 4.6: (a) An exemplary AFM scan of a sample which is 0.1 g/L in NaPA and contains 3.54 mM Sr^{2+} at a total positive ion concentration of 0.1M. (b) Histogram for single molecular volume (for original scan, not deconvoluted to account for geometry of the tip) (c) Histogram for single molecular radius of gyration squared (d) Histogram for contour length (d) Histogram for number of pearl like structures present per molecule (e) Histogram for height of the pearls (f) Histogram for height of the molecular contour between two pearls (Note that if the molecule was globular, the height was put at zero. Only non zero values were included during evaluation of mean values) (g) Histogram for separation between two pearls (Note that if the molecule was globular, the separation was put at zero. Only non zero values were included during evaluation of mean values)

Let us now put the evaluated characteristics in a comparison table.

Characteristic	D	E
[NaPA] (g/L)	0.1	0.1
[Sr^{2+}] (mM)	3.40	3.54
Volume (nm³)	4570	4478
R_g(AFM) (nm)	32.80	33.07
Contour length (nm)	118.37	108.63
No. of pearls per molecule	4	2
Height of pearls (nm)	8.44	9.46
Height of the molecule between two pearls (nm)	6.25	7.53
Separation between pearls (nm)	30.38	36.78

Table 4.3: Comparison table for the surface characteristics of two samples very near to the NaPA-Sr^{2+} phase boundary. The samples are named D and E. The mean values as evaluated from the histograms are listed. Note that for sample E, only non zero values have been included in the evaluation of the mean for the characteristics "height of the molecule between two pearls" and "separation between pearls".

A look at Table 4.3 brings out the essential features which the intermediate states exhibit on the surface. Next, we come to one of the most important evaluated parameters, the radius of gyration on the surface. As mentioned before, R_g(AFM) is a 3D shape parameter for the molecules adsorbed on surface which is compared with R_g(SLS) evaluated in solution. As shown in Table 4.4, the quantity R_g^2(AFM)/R_g^2(SLS) is nearly 0.7-0.8 in samples D and E.

Sample	R_g(AFM) (nm)	R_g^2(AFM) (nm²)	R_g(SLS) (nm)	R_g^2(SLS) (nm²)	R_g^2(AFM)/ R_g^2(SLS)
D	32.80	1075.99	37.2	1383.8	0.77
E	33.07	1093..88	40.1	1608.0	0.68

Table 4.4: The radii of gyration evaluated by AFM and SLS show the same trend. More importantly the ratio R_g^2(AFM)/R_g^2(SLS) approaches a constant value of 2/3. The samples D and E are both 0.1 g/L in NaPA and have a total positive ion concentration of 0.1 M. The concentration of Sr^{2+} ions however is respectively, 3.40 mM and 3.54 mM.

The fact that the ratio R_g^2(AFM)/R_g^2(SLS) approaches a value of 2/3 in both the samples indicate that we have been successful in the kinetic trapping of molecules. Refer eq. 2.61 in Chapter 2, section 2.4.4 and the ref. 118 cited therein. The remaining (insignificant) differences can be explained on the basis that while AFM evaluates the square root of number averaged mean squared radius of gyration, SLS evaluates the square root of z-averaged mean squared radius of gyration. However, it is relevant here to mention the drawbacks of over rating the observed ratio. The R_g^2(AFM)/R_g^2(SLS) ratio of 2/3 (or more simply, the R_g(AFM)/R_g(SLS) ratio of 0.8) indicates that adsorption forces are strong and molecules have adopted a rather flat conformation on the surface. Strong

adsorption forces minimize the effects of sample history so that while the molecule may undergo a z collapse upon flux drying, it does not get altered in the x and y directions. In Chapter 5, we will encounter polyacrylate coils of much smaller molecular weights. Adsorption forces would be substantially weakened. Sample history then plays a significant role and this ratio is less than the 0.7-0.9 limit, as we shall find out.

Before we leave this section, it is interesting to make comparisons with existing theoretical and simulation models as well. First, we must emphasize that we are dealing with a specific chemical entity, a NaPA-Sr^{2+} complex formed very near to the precipitation threshold. We have already commented upon this aspect in Chapter 2, section 2.3. We then must be extremely cautious while extending results developed for monovalent charges to complex chemical bonds, as stated in Chapter 2, section 2.2.3. Finally, it is noteworthy that ours is an example of an annealed polyelectrolyte which is predicted to show charge inhomogeneities, especially during adsorption on surfaces, a point clearly stated in Chapter 2, section 2.1.5. Keeping these aspects in mind, we carry out a qualitative comparison of our results with the simulation results of Uyaver and Seidel (refs. 60 and 61) cited in Chapter 2, section 2.2.2.1.

We do not observe a first order phase transition between a collapsed globule and an extended chain (refer fig. 2.10), either by AFM or by scattering. Hence, we may rule out the possibility of the polyacrylate chain being enough hydrophobic, even when decorated with stoichiometric amounts of Sr^{2+} ions, so that water starts to act as a poor solvent at constant pH of 9. Instead, our situation is more similar to close to θ solvent conditions where necklace-like intermediate states are predicted to be stable, albeit in a narrow window (refer fig. 2.11). In the simulation model proposed by Uyaver and Seidel,[61] the θ

conditions are reached either by reducing the coupling strength ($u=\lambda_B/b$) or by reducing the reduced temperature ($\tau=(\theta-T)/\theta$). While under θ conditions, the coupling strength (the strength with which monomers along the chain interact with each other) is a very important parameter. The coupling strength decides the number of pearls in the intermediate stable state. The very low number of pearls in the AFM scans of samples D and E indicate that coupling strength is very low. This may be due to the large size of Sr^{2+} ion.

Below, we produce typical configurations of necklace-like intermediate states carved out of the AFM scans of samples D and E and put them alongside typical simulation snapshots obtained by Uyaver and Seidel[61] for an annealed polyelectrolyte close to θ conditions and interacting with weak coupling strength.
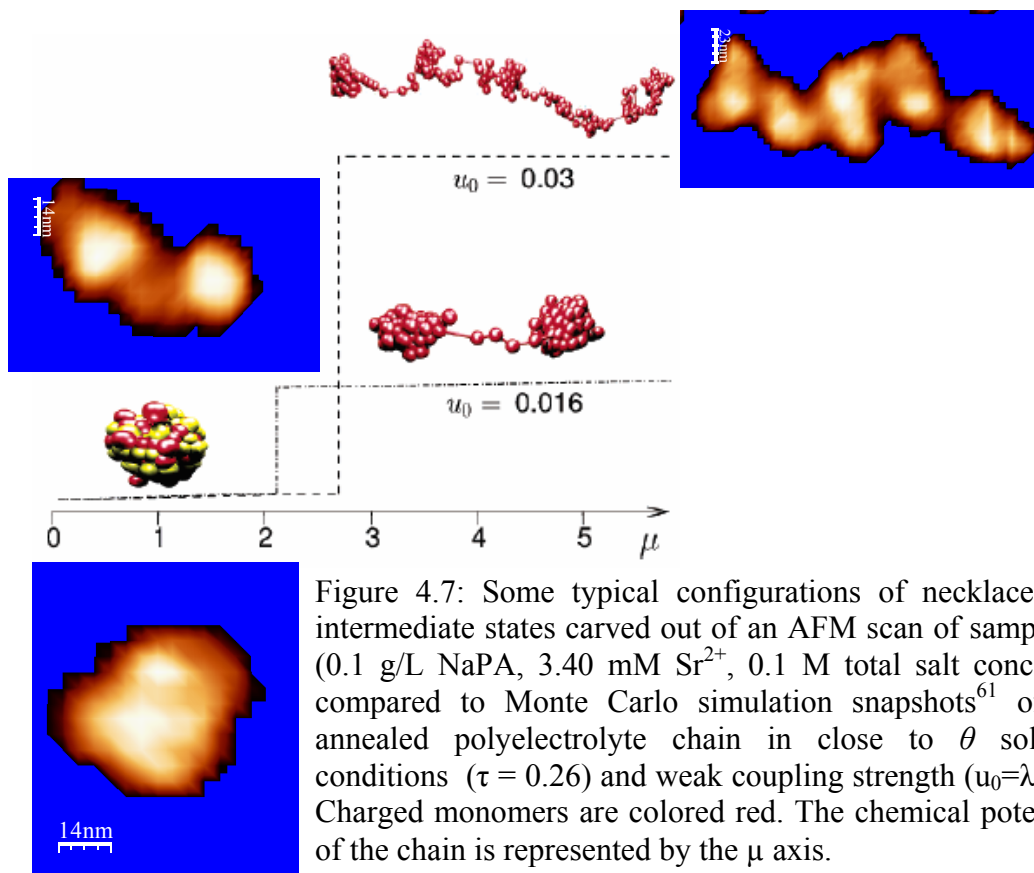
Figure 4.7: Some typical configurations of necklace-like intermediate states carved out of an AFM scan of sample D (0.1 g/L NaPA, 3.40 mM Sr^{2+}, 0.1 M total salt conc.) as compared to Monte Carlo simulation snapshots[61] of an annealed polyelectrolyte chain in close to θ solvent conditions ($\tau = 0.26$) and weak coupling strength ($u_0=\lambda_B/b$). Charged monomers are colored red. The chemical potential of the chain is represented by the μ axis.

Figure 4.8: Some typical configurations of necklace-like intermediate states carved out of an AFM scan of sample E (0.1 g/L NaPA, 3.54 mM Sr^{2+}, 0.1 M total salt conc.) as compared to Monte Carlo simulation snapshots[61] of an annealed polyelectrolyte chain in close to θ solvent conditions ($\tau = 0.26$) and weak coupling strength ($u_0 = \lambda_B/b$). Charged monomers are colored red. The chemical potential of the chain is represented by the μ axis.
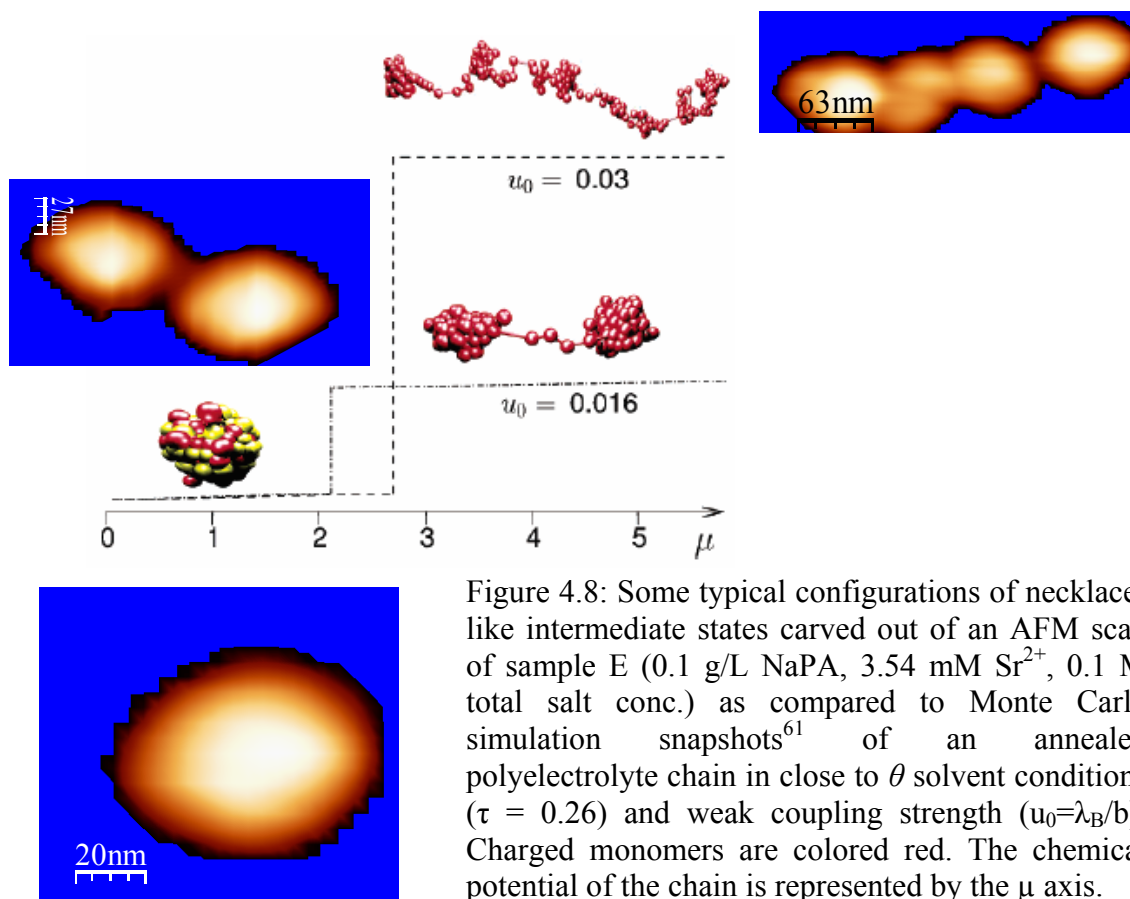
It must be recognized that the specifically binding cation for discharging the polyelectrolyte chain is unarguably H^+ ion in the study of Uyaver and Seidel cited above. In our case, the specifically binding ion is Sr^{2+} which is much larger and may therefore be assumed to decouple the charges more strongly. Besides, an extra inert salt, NaCl, is present in the solution which also screens the charges as outlined in Chapter 2, section 2.3 and ref. 90 cited therein. Thus, we anticipate, at best, only a qualitative match with the quoted simulation results. Even in doing so, we are ignoring the (very important) chemical effects of Sr^{2+} ions. However, the simulation study cited above is still relevant in the sense that it pertains to annealed polyelectrolytes under θ conditions. More representative AFM scans can be found in Appendix C1.

4.3.4 Departure from the phase boundary at constant strontium concentration

Samples, F and G represent the departure from the phase boundary parallel to the X axis (fig. 4.1). The situation is similar to the approach parallel to Y axis (fig. 4.1) represented by samples B and C. The difference between AFM scans shown in fig. 4.3a (sample B) and fig. 4.4 (sample C) with those of samples F and G in fig. 4.9a and fig. 4.10a respectively is that the latter are free of random coils. This is expected due to a high concentration of Sr^{2+} ions. The bivalent ions play an important role in generating stronger adsorption and hence resisting the shear forces responsible for random coiling on the surface.

Samples F and G are, respectively, 0.3 g/L and 0.5 g/L in NaPA and contain 3.40 mM Sr^{2+} ion concentration each at a constant total positive ion concentration of 0.1 M. These concentrations of polyacrylates are too high for any meaningful single molecular surface study.
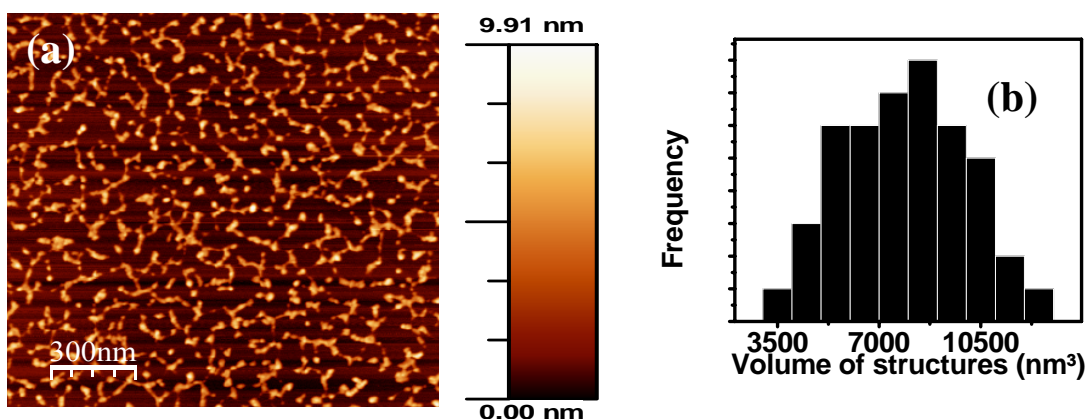
Figure 4.9: (a) An exemplary AFM scan of a sample which is 0.3 g/L in NaPA with a Sr^{2+} concentration of 3.40 mM and total positive ion concentration of 0.1 M (b) Volume histogram shows a mean volume of 7857 nm³ indicating dimers have formed on the surface. Scattering data does not show dimers.
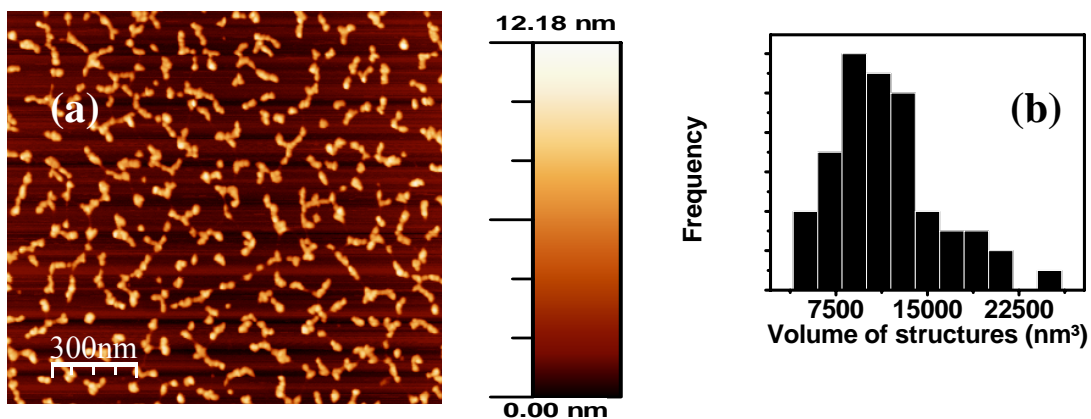
Figure 4.10: (a) An exemplary AFM scan of a sample which is 0.5 g/L in NaPA with a Sr^{2+} concentration of 3.40 mM and total positive ion concentration of 0.1 M (b) Volume histogram shows a mean volume of 11561 nm³ indicating trimers have formed on the surface. Scattering data does not show trimers.

The volume histograms in fig. 4.9b and fig. 4.10b respectively for structures visible on the AFM scans of samples F and G indicate that dimers or trimers have been formed. The mean volume of structures seen on scans of sample F is calculated to be 7857 nm³ indicating, most probably, the formation of dimers as the molecules coalesce together during adsorption. On similar lines, the mean volume of structures seen on scans of sample G is calculated to be 11561 nm³ indicating the formation of trimers during adsorption. As such, we have surpassed the boundary limits within which reasonable comparisons can be made between AFM and scattering data. Scattering data does not indicate the formation of dimers or trimers.

Investigation of sodium polyacrylate-lead phase boundary

5.1 Introduction

In this Chapter, we investigate the on-surface collapse behavior of NaPA induced by Pb^{2+} as specifically binding ions and compare it with the corresponding behavior in solution. In comparison to Chapter 4, the current Chapter holds some new and important aspects. First, Pb^{2+} is a p-block element and its study was crucial as its bonding with the polyacrylate might be different in its chemical nature than alkaline earth cations. Second, an advantage of using small bivalent cations (like Pb^{2+}) for studying collapse transitions is that small sized chains can also be studied. Third, small size of the chains in turn implies that higher concentration regimes of NaPA can be probed for collapse transitions without the risk of inter-particle correlations. While the aforementioned represents a good scenario for SLS/SAXS/ASAXS, it makes the task of single molecular AFM imaging that much more difficult. Small size of coils might further inhibit strong adsorption on mica surfaces, given that polyacrylates already represent a class of polyelectrolytes which are non bulky and anionic, whose adsorption on (negative) mica surfaces is weak in the first place. Likewise, there is a limit upto which an AFM experimentalist can probe higher concentration regimes while still within the ambit of single molecular resolution. This limit may be quite low on surfaces as compared to a similar limit in solution. We saw an example in Chapter 4, section 4.3.4 where dimers and trimers were formed on surface (samples F and G) while scattering data did not indicate any such structures in solution.

Under the conditions described above, it was thought most appropriate to chemically modify mica surfaces using 3-aminopropyl dimethyl ethoxy silane as discussed in

Chapter 3, section 3.2.2. The reference sample (A), i.e., the sample without any Pb^{2+} ions contained 0.1M of inert salt, $NaNO_3$. Its weight averaged molecular weight was found to be only 456,000 g/mole by means of SLS. The concentration of NaPA used was 1.00 g/L. At the phase boundary, we were able to identify seven more samples (B, C, D, E, F, G and H) which showed a very drastic decrease in coil dimensions (investigated by combined SLS and DLS) upon subtle variations in Pb^{2+} ion concentration. These samples represented intermediate states along the coil to globule transition of NaPA induced by Pb^{2+} ions. Hence they were analysed in detail using SLS and SAXS/ASAXS in solution and AFM on surfaces. The pH of all samples was set to 9.

Our aim in this Chapter would be more or less the same as in Chapter 4, i.e., how much do the AFM images succeed in evaluating the essential features of polyelectrolyte coils on surfaces which the very coils exhibit in solution?

The concentrations of NaPA and Pb^{2+} ions in samples A-H are tabulated in Table 5.1. The total positive ion concentration was the same in all the samples, at 0.1 M.

Sample	A	B	C	D	E	F	G	H
[NaPA] g/L	1.00	0.67	0.60	0.58	0.54	0.45	0.38	0.36
[Pb^{2+}] mM	0.00	1.65	1.65	1.65	1.65	1.25	1.00	1.00

Table 5.1:The concentrations of NaPA and Pb^{2+} ions in samples A-H. A is the reference sample while samples B-H are very close to the phase boundary.

5.2 Solution behavior analysed by scattering

As in Chapter 4, sample A, our reference sample, showed a marked contrast compared to samples at the precipitation threshold (phase boundary). Combined SLS and DLS experiments did not reveal any kind of sectional collapse associated with the reference

sample and the coils were well extended, as expected at a pH of 9 for a low molecular weight polyanion. For samples B-H which were close to the phase boundary, combined SLS and DLS revealed a drastic reduction in coil dimensions. Thus, further SAXS/ASAXS analysis was carried out on these samples. The results indicated presence of partially collapsed coils with sub-domains which could be interpreted in terms of a pearl-necklace structure. The radii of gyration values for samples B-H (evaluated by SLS) are mentioned in Table 5.2.

Sample	[NaPA] g/L	[Pb^{2+}] mM	R$_g$ (SLS) nm
B	0.67	1.65	28.02
C	0.60	1.65	26.70
D	0.58	1.65	23.75
E	0.54	1.65	29.43
F	0.45	1.25	30.34
G	0.38	1.00	30.30
H	0.36	1.00	24.78

Table 5.2: The radius of gyration values in samples B-H as evaluated by SLS (courtesy of Lages, S. and Huber, K). These samples were very close to the phase boundary and were investigated for intermediate states along the coil to globule transition.

5.3 Surface behavior analysed by AFM

We shall divide this section into two parts. The first part, section 5.3.1, will describe AFM images of the reference sample. It is the second part, section 5.3.2, which is at the core of this Chapter. It deals with AFM images of samples at the phase boundary.

5.3.1 Surface behavior of reference samples without any lead

Fig. 5.1a shows an exemplary AFM scan of the reference sample A adsorbed onto chemically modified mica surface. It is clear that the molecules are largely extended with no sectional collapse, despite the fact that 0.1 M $NaNO_3$ is present as an inert salt in the reference sample. This is line with what is observed in solution and is a major difference between the reference sample and the samples near the phase boundary.
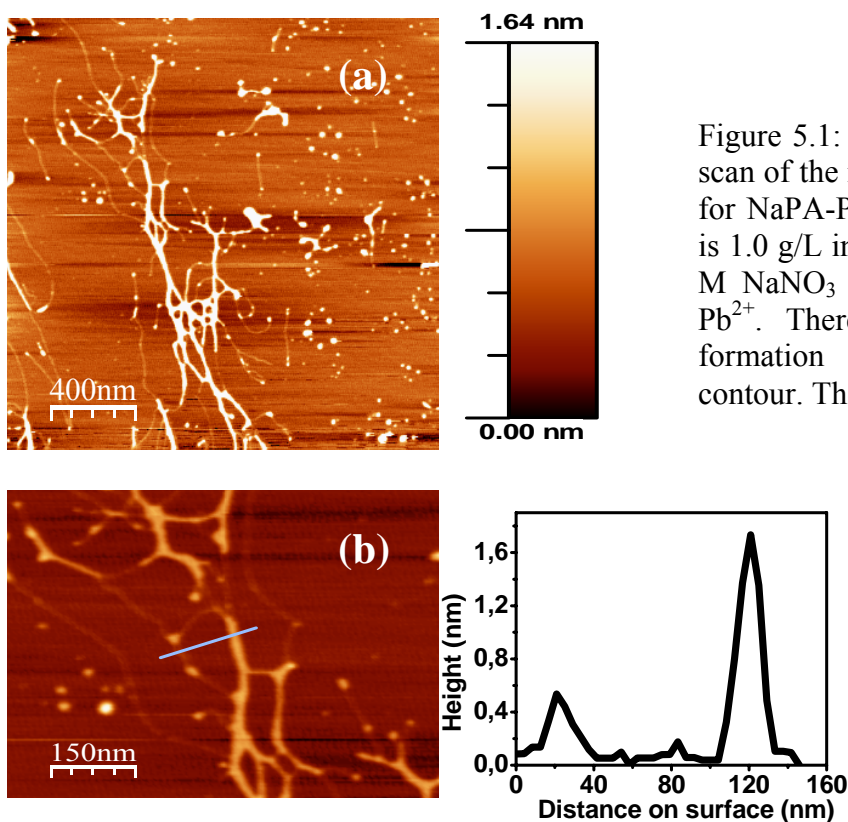
Figure 5.1: (a) An exemplary AFM scan of the reference sample chosen for NaPA-Pb^{2+} system. The sample is 1.0 g/L in NaPA and contains 0.1 M $NaNO_3$ as an inert salt but no Pb^{2+}. There is no distinct pearl formation along the molecular contour. The coils are well extended

(b) Coelescence of extended coils due to shear fields created upon flux drying of samples result in „fiber" formation with a height profile two to three times larger than single molecular height profile.

It is noteworthy that despite chemical modification which smoothens the mica surface, noise levels during AFM scanning of extended coils remain a problem. This can be seen in the presence of very small globules which are actually sections of an extended coil, a larger part of which has remained invisible to an AFM scan. The latter can be verified by the fact that the volume of these globules is significantly lower than the single molecular volume of 1600 nm³ expected for a coil of 456,000 g/mole assuming its dry state density

to be 1g/cc (Appendix A, section A2.3.1.1). The presence of shear field on the smoothened surface is also evident. This shear field, created during drying procedures, may have resulted in the coalescence of a number of extended coils into some kind of "fiber". As shown in fig. 5.1b, the height profile of these fibers is approximately two to three times larger than the single molecular height profile.

5.3.2 Investigations at the phase boundary

The situation at the phase boundary is represented by the samples B-H. Combined SLS and DLS data reveals a drastic collapse of coils in these samples. Hence these represent the intermediate states in solution along the coil to globule transition of polyacrylate coils. The very same samples were adsorbed on chemically modified mica substrates and subdued to AFM imaging. Sectional collapse begins in these samples. Pearl formation in these samples on surfaces is completely in agreement with scattering data for solution behavior. Firstly, all AFM scans of these samples were checked for absence of shear forces and inter-particle correlations using reciprocal space analysis (Appendix A, section A2.3.2.1). These were found to be absent. The situation on the surface was similar to the one described by fig. A7 in Appendix A, section A2.3.2.1. Any statistical treatment was done after confirming that molecules adsorbed on the surface were single molecules and not clusters. Thus, volume histograms were the first to be evaluated (Appendix A, section A2.3.1.1). The theoretically predicted volume of a single molecule of molecular weight 456,000 g/mole (approx.) assuming the dry state density as 1g/cc comes out to be 1600 nm^3. Within statistical error, the mean volumes shown by our histograms are slightly higher. Deconvolution to account for the geometry of the tip should bring the experimental values close to the ones theoretically anticipated. The absence of shear,

inter-particle correlations and aggregates highlights the utility of chemical modification of surfaces while trying to image single molecules at higher concentrations in the weak adsorption limit. We shall have more to say on that in Chapter 6.

Fig. 5.2a-g shows, respectively, exemplary AFM scans of the samples B, C, D, E, F, G and H. A look at these AFM scans brings out the essential features which the intermediate states exhibit on the surface. The presence of specifically binding ion, Pb^{2+}, at a fixed total positive ion concentration of 0.1 M shrinks the polyacrylate. In all the samples, the number of pearls per molecule shows a broad distribution of one to five. This points to the fact that molecules with different number of pearls coexist at the same time representing a cascade. These observations are in line with theoretical predictions we discussed in Chapter 2, section 2.2.2.

Figure 5.2: Exemplary AFM scans for (a) Sample B (b) Sample C (c) Sample D (d) Sample E (e) Sample F (f) Sample G (g) Sample H. Please refer Table 5.2 for details of the samples.
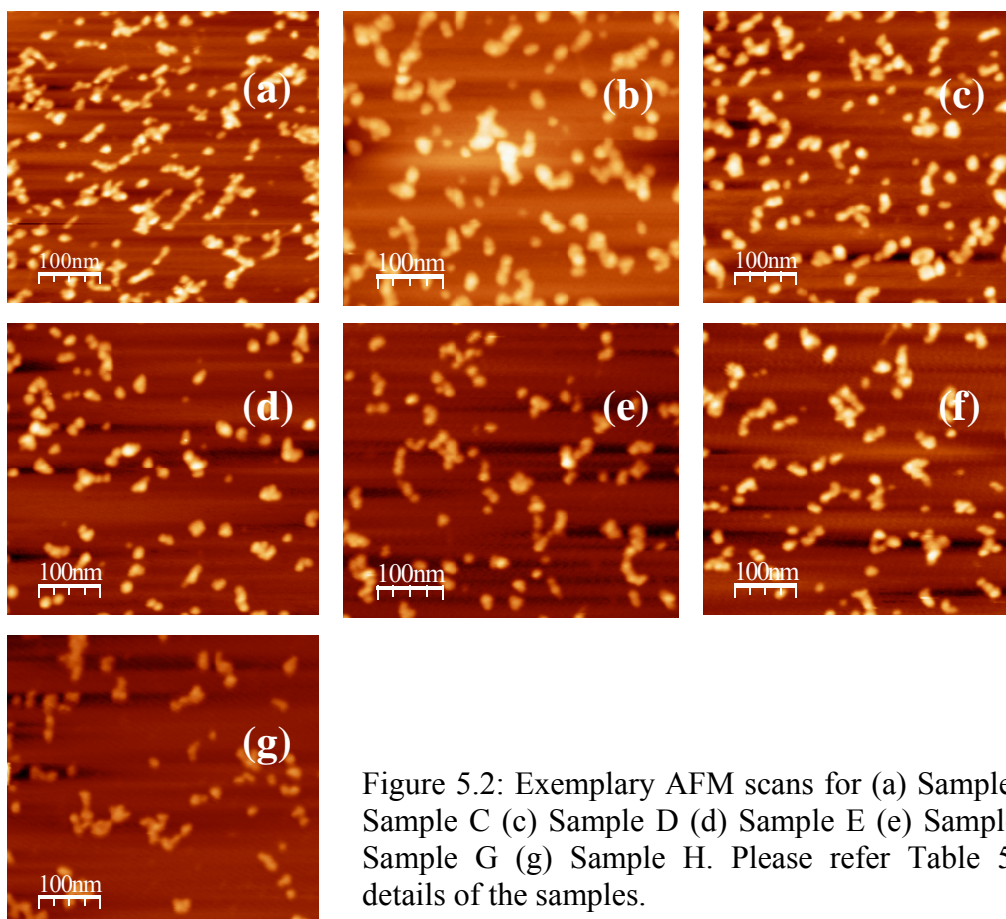
Finally, a 3D shape parameter on the surface, R_g(AFM), is evaluated for the samples (Appendix A, section A2.3.1.2). It is this parameter which is directly compared to R_g(SLS) and conclusions have been drawn.

We present here quantitative comparison for one of the samples at the phase boundary, lets say sample D. Fig. 5.3a-c shows respectively, an exemplary AFM scan, volume histogram and radius of gyration histogram for sample D.
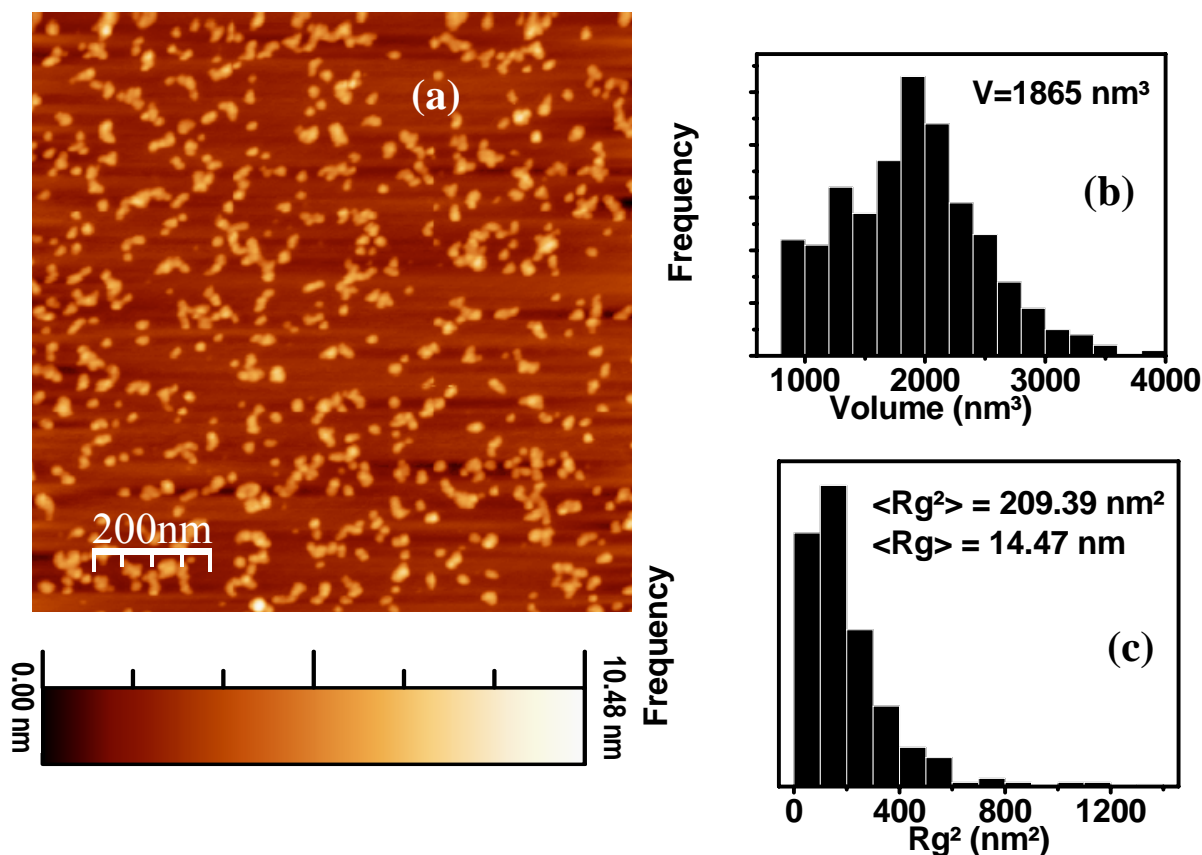
Figure 5.3: (a) An exemplary AFM scan of a sample which is 0.58 g/L in NaPA and contains 1.65 mM Pb^{2+} at a total positive ion concentration of 0.1M. (b) Histogram for single molecular volume (for original scan, not deconvoluted to account for geometry of the tip) (c) Histogram for single molecular radius of gyration

We notice that the ratio R_g(AFM)/R_g(SLS) for this sample is nearly 0.6. But first, lets look deeper into this ratio. The ratio R_g(AFM)/R_g(SLS) contains information about

sample history, i.e., the effects of substrate-sample interactions and capillary action during solvent removal (Chapter 2, section 2.4.1). The results indicate that, for the particular system under investigation, R_g values on surfaces may decrease by 40% as compared to R_g values in solution. The fact that AFM evaluates the square root of number averaged while SLS evaluates the square root of z-averaged mean squared radius of gyration, alone cannot explain this low value. We believe that the electrostatic repulsive forces acting at the substrate-sample interface drastically reduces the R_g component parallel to the surface as the negatively charged polyelectrolyte adsorbs on to mica. In other words, the adsorption of the polyacrylate is not flat, but rather isotropic. Capillary forces associated with flux drying cause further compaction parallel to the surface. The R_g component perpendicular to the surface might also undergo a collapse due to solvent evaporation even when adsorption forces remain weak to cause a z collapse on their own. The sample history becomes important here (compare with Chapter 4, for example) because of low mol wt. of the NaPA coil being imaged.

Our arguments are in line with the results of Molecular Dynamics simulations made recently by Yethiraj et al.[133] for polyelectrolyte adsorption from solution on to oppositely charged surfaces while fully incorporating the effects of solvent quality, surface charge density and co-ions (opposite in charge to the surface and used to balance the surface charge). For a given solvent quality, the authors observed a nonmonotonic dependence of the parallel component of R_g on surface charge density. In their study, the drastic decrease in the parallel component of R_g was attributed to repulsions between the polyelectrolyte and similarly charged co-ions on the surface which inhibited a flat extended adsorption of the polyelectrolyte. It was in contrast to preceding simulations for

polyelectrolyte adsorption which did not incorporate the effects of these electrostatic repulsions and hence, either observed a monotonically increasing dependence of parallel component of R_g on surface charge density[134-135] or reported it to be insensitive towards surface charge density.[136] All the mentioned simulation studies[133-136] however agree on a monotonically decreasing dependence of perpendicular component of R_g on surface charge density indicating stronger adsorption forces are required to cause sufficient z collapse. This is summarized in fig. 5.4.
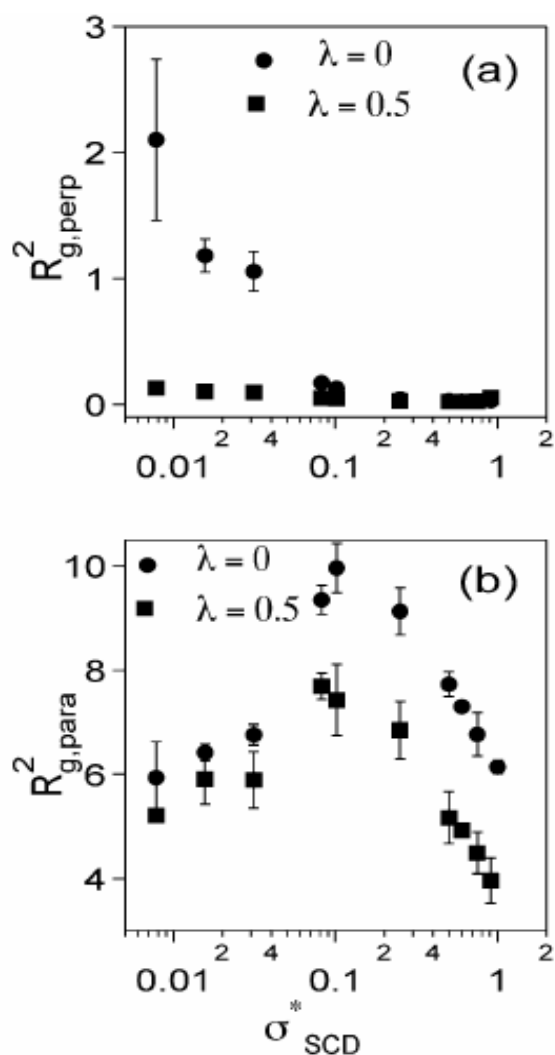
By comparing R_g values on surfaces and in solution, we have added information to the kind of ratios expected when adsorption forces are weak. This marks a departure from similar studies made earlier when adsorption forces were rather strong (Chapter 2, section 2.4.4 and the refs. 116, 118 cited therein). In these studies, the expected values of ratios were much larger.

Figure 5.4: The variation of (a) perpendicular and (b) parallel component of radius of gyration with surface charge density for adsorption from good ($\lambda=0$) and poor ($\lambda=0.5$) solvents. (adopted from ref. [133])

Before we leave this section, it is interesting to make comparisons with another existing simulation model, that of annealed polyelectrolytes under θ solvent conditions, as done in Chapter 4, by quoting Uyaver and Seidel (refs. 60 and 61 cited in Chapter 2, section 2.2.2.1.) This is because ours is an example of an annealed polyelectrolyte which is predicted to show charge inhomogeneities, especially during adsorption on surfaces, a point clearly stated in Chapter 2, section 2.1.5. Also, since we do not observe a first order phase transition between a collapsed globule and an extended chain (refer fig. 2.10), either by AFM or by scattering, we may rule out the possibility of the polyacrylate chain being enough hydrophobic, even when decorated with stoichiometric amounts of Pb^{2+} ions, so that water starts to act as a poor solvent at constant pH of 9. Instead, our situation is more similar to close to θ solvent conditions where necklace-like intermediate states are predicted to be stable, albeit in a narrow window (refer fig. 2.11).

In the simulation model proposed by Uyaver and Seidel,[61] the θ conditions are reached either by reducing the coupling strength ($u=\lambda_B/b$) or by reducing the reduced temperature ($\tau=(\theta-T)/\theta$). While under θ conditions, the coupling strength (the strength with which monomers along the chain interact with each other) is a very important parameter. The coupling strength decides the number of pearls in the intermediate stable state. The relatively high number of pearls (as compared to Chapter 4) in the AFM scans of sample D indicates that coupling strength may be treated as moderate. This may be due to the smaller size of Pb^{2+} ion as compared to the large size of Sr^{2+} ion dealt with in Chapter 4. Before we compare typical configurations of necklace-like intermediate states carved out of the AFM scans of sample D by putting them alongside typical simulation snapshots

obtained by Uyaver and Seidel[61] for an annealed polyelectrolyte close to θ conditions and

interacting with moderate coupling strength, we must add a few words of caution.
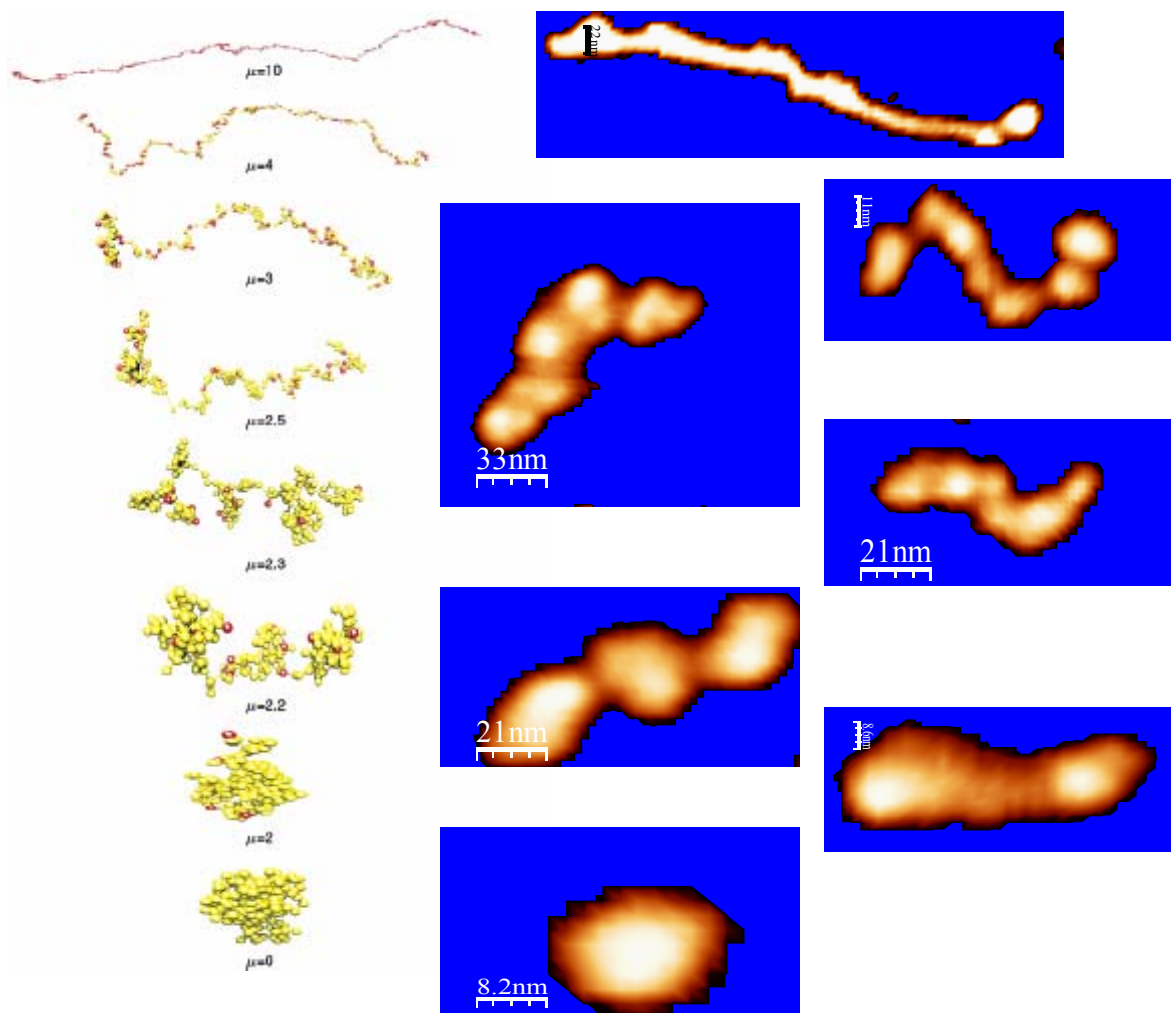
Figure 5.5: Some typical configurations of necklace-like intermediate states carved out of an AFM scan of sample D (0.58 g/L NaPA, 1.65 mM Pb^{2+}, 0.1 M total salt conc.) as compared to Monte Carlo simulation snapshots[61] of an annealed polyelectrolyte chain in close to θ solvent conditions ($\tau = 0.07$) and moderate coupling strength ($u_0 = \lambda_B/b$). Charged monomers are colored red. The chemical potential of the chain is represented by the μ.

First, we must emphasize that we are dealing with a specific chemical entity, a NaPA-

Pb^{2+} complex formed very near to the precipitation threshold.   We have already

commented upon this aspect in Chapter 2, section 2.3. We then must be extremely

cautious while extending results developed for monovalent charges to complex chemical

bonds, as stated in Chapter 2, section 2.2.3. It must also be recognized that the specifically binding cation for discharging the polyelectrolyte chain is unarguably H^+ ion in the study of Uyaver and Seidel.[61] In our case, the specifically binding ion is Pb^{2+} which is much larger and may therefore be assumed to decouple the charges more strongly. Besides, an extra inert salt, $NaNO_3$, is present in the solution which also screens the charges as outlined in Chapter 2, section 2.3 and ref. 90 cited therein. Thus, we anticipate, at best, only a qualitative match with the quoted simulation results. Even in doing so, we are ignoring the (very important) chemical effects of Pb^{2+} ions.

More representative scans can be found in Appendix C2.

Temperature induced collapse of sodium polyacrylate in presence of calcium

6.1 Introduction

In 2004, Antonietti et al.[137] made a startling new observation. They performed a thermodynamic investigation of the interaction of Ca^{2+} ions with anionic polyacrylate chains by means of calorimetric titration. The authors titrated a dilute solution of NaPA with a $CaCl_2$ solution and observed an endothermal process. The results indicated that the formation of calcium polyacrylate is entropic in nature. These findings were unexpected at first sight because a considerable enthalpy gain was suspected due to a strong attraction between bivalent Ca^{2+} and the COO^- residues along the chain backbone. The amount of enthalpy consumed by the process could successfully be attributed to the liberation of 10 water molecules and 2 Na^+ ions per Ca^{2+} ion bound to PA. In 2005, Molnar and Rieger published a Molecular Dynamics simulation[138] of the interaction of NaPA oligomers with Ca^{2+} cations. They found an abrupt increase of free Na^+ ions if more than 3 Ca^{2+} cations have been added to the simulated cubic solution box. Along with this Na^+ "evaporation" the averaged distance between C atoms of two different oligomers decreased. The latter effect was denoted as "like charge attraction" and is attributed to an increased degree of hydrophobicity of the increasingly discharged PA backbone chain. Then in 2007, Huber et al.[103] used light scattering to note the entropic nature of coil collapse in solution as the equilibration temperature of NaPA-Ca^{2+} system was raised. This coil collapse was completely reversible, i.e., original dimensions of the coil could be accessed simply by lowering the temperature.

We decided to pick up this interesting phenomenon for answering three important questions. First, whether this reversible entropic coil collapse passes through a necklace

like intermediate state? Second, is it possible to observe this reversible entropic coil collapse directly on surfaces using AFM imaging? Lastly, if the answer to the second proposed question is yes, how much do the AFM images of intermediate states reflect the respective conformation in solution?

Two samples, which we shall name SASE and SASH, both of which were close to the NaPA-Ca^{2+} phase boundary and both of which exhibited considerable coil shrinking (revealed by combined SLS and DLS) as the equilibration temperature of the system was raised from 15°C to 30°C, were suitably identified and characterized using SLS at both the equilibration temperatures. Further analysis was carried out on these two samples and at both the equilibration temperatures using SANS to study the internal structure of coils. SASE was 0.2346 g/L NaPA solution in D_2O containing 1.00 mM Ca^{2+} and 8.00 mM Na^+ while SASH was 0.1300 g/L NaPA solution in D_2O containing 0.65 mM Ca^{2+} and 8.70 mM Na^+. The total positive ion concentration in either of the samples can be identified to be 0.01 M. This is an order of a magnitude lower than what we have hitherto seen. We discussed this in Chapter 2, section 2.3.6. Apart, two reference samples, referred to as REFE and REFH, were Ca^{2+} free analogues of SASE and SASH respectively. The samples REFE and REFH had the same total positive ion concentration, i.e., 0.01 M, yet without any $CaCl_2$. SLS preformed at room temperature revealed that the NaPA in the reference samples had a weight averaged molar mass of 783,000 g/mole in dilute aqueous solution in the presence of 0.01 M NaCl as an inert electrolyte. A pH of 9 was maintained for all the sample solutions.

Reference samples REFE and REFH were imaged at room temperature using $LaCl_3$ pre-treated mica surfaces as discussed in Chapter 3, section 3.2.1. Samples SASE and SASH

were imaged on both $LaCl_3$ pre-treated mica surfaces (Chapter 3, section 3.2.1) as well as mica surfaces chemically modified with 3-aminopropyl dimethyl ethoxy silane (Chapter 3, section 3.2.2) and at both the equilibration temperatures of 15°C and 30°C (Chapter 3, section 3.2.3).

The concentrations of NaPA and Ca^{2+} in samples REFE, SASE, REFH and SASH are tabulated in Table 6.1. The total concentration of positive charges was the same in all the samples, 0.01 M.

Sample	REFE	SASE	REFH	SASH
[NaPA] g/L	0.2346	0.2346	0.1300	0.1300
[Ca^{2+}] mM	0.00	1.00	0.00	0.65

Table 6.1: The concentrations of NaPA and Ca^{2+} in samples REFE, SASE, REFH and SASH. The reference samples REFE and REFH were analysed at room temperature. The samples SASE and SASH are close to the NaPA-Ca^{2+} phase boundary and were analysed at equilibration temperatures of 15°C and 30°C.

6.2 Solution behavior analysed by scattering

The reference samples, REFE and REFH, analysed at room temperature showed extended conformation of molecules. No sectional collapse could be identified by combined SLS and DLS. Samples SASE and SASH equilibrated at 15°C showed partially collapsed chains. However, SANS did not reveal any sub-domain formation in these samples. At the equilibration temperature of 30°C, SASE and SASH exhibited far greater collapse as compared to the equilibration temperature of 15°C. SANS clearly indicated pearl formation at the equilibration temperature of 30°C. The structure could be interpreted in terms of a pearl-necklace with low amount of pearls per molecule. The pearl-pearl separation distance was found to be 80.0 nm in both SASE-30°C and SASH-30°C by

means of SANS. Table 6.2 summarizes the radius of gyration values of samples SASE-15°C, SASE-30°C, SASH-15°C and SASH-30°C as measured by SLS as well as quotes the pearl-pearl separation distance in samples SASE-30°C and SASH-30°C as evaluated by SANS.

Sample	[NaPA] g/L	[Ca^{2+}] mM	R_g(SLS) nm	Pearl-pearl separation distance (SANS) nm
SASE-15°C	0.2346	1.00	38.3	No pearls identified
SASE-30°C	0.2346	1.00	25.6	80.0
SASH-15°C	0.1300	0.65	52.8	No pearls identified
SASH-30°C	0.1300	0.65	32.8	80.0

Table 6.2: The radius of gyration and pearl-pearl separation distance values, as evaluated by SLS and SANS respectively, in samples SASE and SASH equilibrated at both 15°C and 30°C (courtesy of Lages, S. and Huber, K). These samples were very close to the phase boundary and were investigated for intermediate states along the coil to globule transition.

6.3 Surface behavior analysed by AFM

We will divide this section into three parts. The first part, section 6.3.1, will discuss AFM images of reference samples analysed at room temperature. The second and third parts, sections 6.3.2 and 6.3.3, will analyse AFM images of both SASE and SASH at both the equilibration temperatures of 15°C and 30°C, the former section being devoted to radii of gyration evaluation while the latter section will discuss evaluation of the 2D form factor. The R_g(AFM) values will be compared to R_g(SLS) values while the correlation distances revealed by peaks in the 2D form factor will be compared to the pearl-pearl separation distance revealed by SANS.

6.3.1 Surface behavior of reference samples without any calcium

Fig. 6.1a-c and Figure 6.1d-f show exemplary AFM scans for REFE and REFH respectively along with their height profiles. The images show extended worm like chains with height profiles close to the single molecular range (1-3 nm). The extended worm like shape of the chains is in line with scattering experiments.
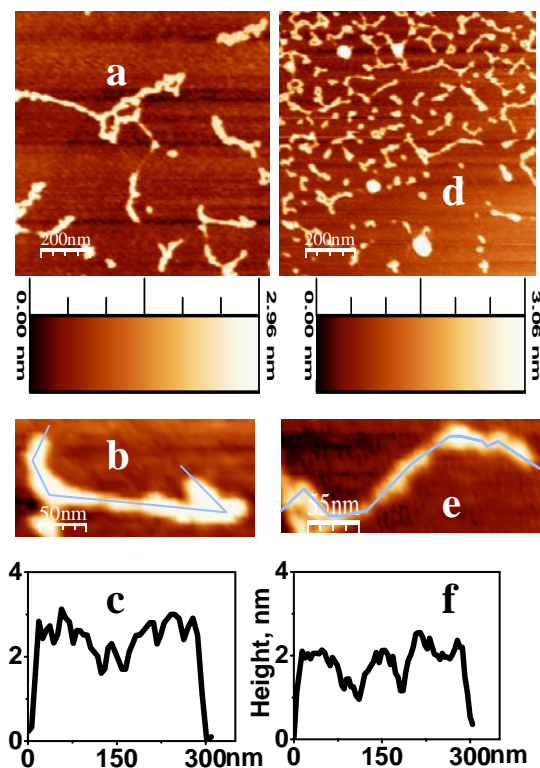
Figure 6.1: Reference samples REFE and REFH measured at room temperature. The reference samples are free of $CaCl_2$ but have the same NaPA concentrations as sample SASE and SASH respectively, with c = 0.2346 g/L (REFE) and c = 0.1300 g/L (REFH) and [NaCl] = 0.01 M. In either case, polyacrylates appear as extended worm-like chains and do not show any collapsed sub-domains. (a) AFM topography image for REFE; (b) zoom of the image A; (c) height profile taken along a single chain as shown by the line in the zoom image B; (d) AFM topography image for REFH; (e) zoom of the image D; (f) height profile taken along a single chain as shown by the line in the zoom image E.

Further resolution of these randomly coiled structures to a statistically significant amount of isolated single molecules was not possible. It was observed that the lack of a specifically binding ion in the sample inhibits strong adsorption of the (negatively charged) polyacrylate coils on (negative) mica surfaces. We suspect that even after treating mica surfaces with 0.01 g/L $LaCl_3$ solution, the surface is slightly undercharged for strong trapping of the reference samples. Such a scenario does not exclude the possibility of shear fields created during drying procedures making visualization of

isolated single molecules difficult. However, a visual comparison of these images with those of SASE and SASH shown in Figs. 6.2-6.5 immediately brings out two important differences. The polyacrylates without any Ca^{2+} ions show greater extension and a complete absence of collapsed sub-domains along the contour. On the other hand, the presence of Ca^{2+} ions shrinks the coils drastically and sections within the chain begin to collapse into sub-domains. These findings correspond well with the findings in solution.

6.3.2 Investigations at the phase boundary in real space

The situation at the phase boundary is represented by samples SASE and SASH. These represent intermediate states along the coil to globule transition and were analysed in detail. Firstly, all AFM scans of these samples were checked for absence of shear forces and inter-particle correlations using reciprocal space analysis (Appendix A, section A2.3.2.1). These were found to be absent. The situation on the surface was similar to the one described by fig. A7 in Appendix A, section A2.3.2.1. Any statistical treatment was done after confirming that molecules adsorbed on the surface were single molecules and not clusters. Thus, volume histograms were the first to be evaluated (Appendix A, section A2.3.1.1). The theoretically predicted volume of a single molecule of molecular weight 783,000 g/mole assuming the dry state density as 1g/cc comes out to be 1700 nm³. Within statistical error, the mean volumes shown by our histograms are slightly higher. Deconvolution to account for the geometry of the tip should bring the experimental values close to the ones theoretically anticipated.

Fig. 6.2a-e and fig. 6.3a-e show exemplary AFM scans for SASE equilibrated at 15°C and 30°C respectively along with their height profiles, volumes and radii of gyration.

Figure 6.2: Adsorption of sample SASE equilibrated at 15°C onto freshly cleaved mica, treated with a solution of 0.01 g/L LaCl$_3$. Presence of Ca^{2+} ions drastically reduces the size of coils and sections within the chain begin to collapse into sub-domains (compare with fig. 6.1a). (a) AFM topography image (b) zoom of the image (c) height profile taken along a well resolved single chain as shown by the line in the zoom image (d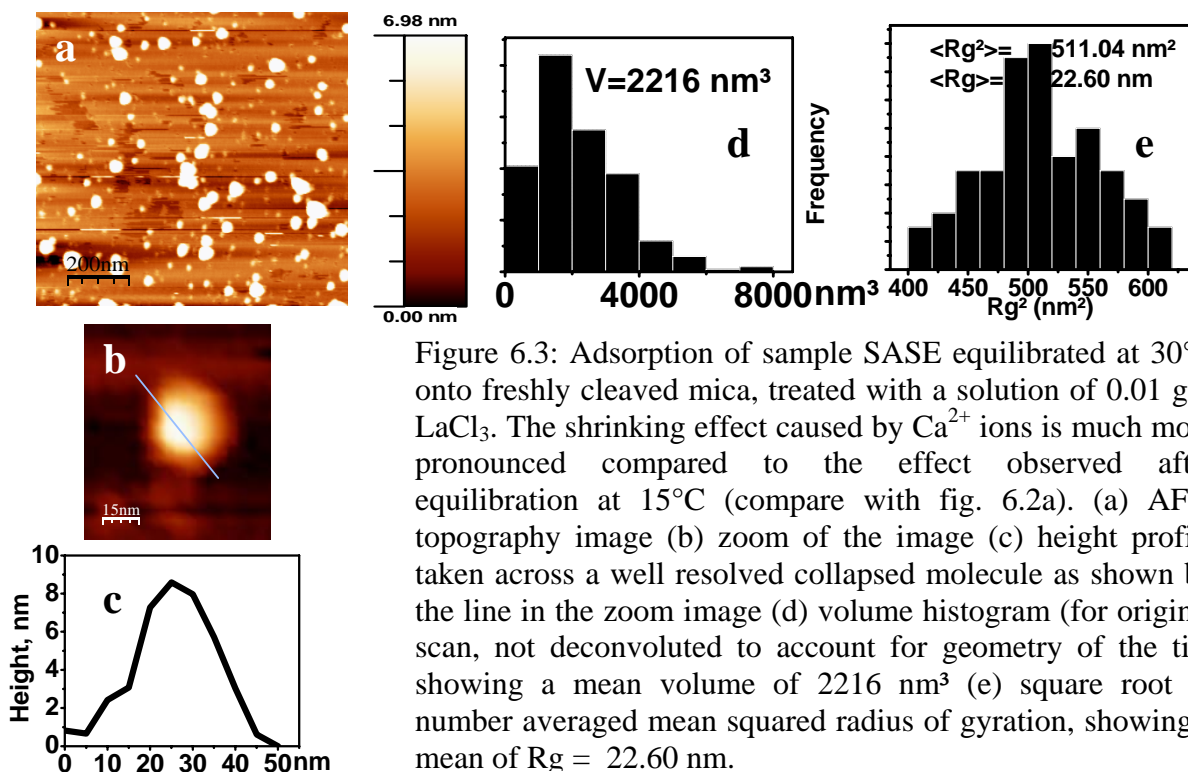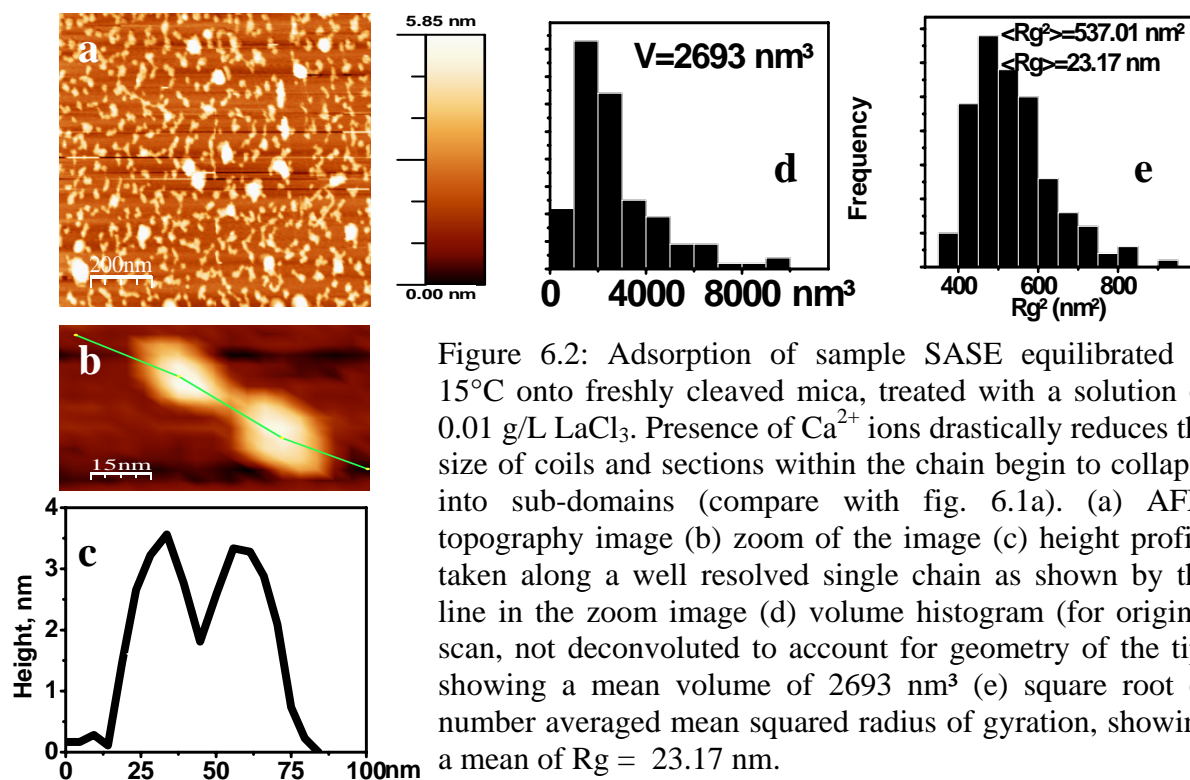) volume histogram (for original scan, not deconvoluted to account for geometry of the tip) showing a mean volume of 2693 nm³ (e) square root of number averaged mean squared radius of gyration, showing a mean of Rg = 23.17 nm.

Figure 6.3: Adsorption of sample SASE equilibrated at 30°C onto freshly cleaved mica, treated with a solution of 0.01 g/L LaCl$_3$. The shrinking effect caused by Ca^{2+} ions is much more pronounced compared to the effect observed after equilibration at 15°C (compare with fig. 6.2a). (a) AFM topography image (b) zoom of the image (c) height profile taken across a well resolved collapsed molecule as shown by the line in the zoom image (d) volume histogram (for original scan, not deconvoluted to account for geometry of the tip) showing a mean volume of 2216 nm³ (e) square root of number averaged mean squared radius of gyration, showing a mean of Rg = 22.60 nm.

Figure 6.4: Adsorption of sample SASH equilibrated at 15°C freshly cleaved mica, treated with a solution of 0.01 g/L LaCl$_3$. Presence of Ca^{2+} ions drastically reduces the size of coils and sections within the chain begin to collapse into sub-domains (compare with fig. 6.1d). (a) AFM topography image (b) zoom of the image (c) height profile taken along a single chain as shown by the line in the zoom image (d) volume histogram (for original scan, not deconvoluted to account for geometry of the tip) showing a mean volume of 2010 nm³ (e) square root of number averaged mean squared radius of gyration, showing a mean of Rg = 25.00 nm.
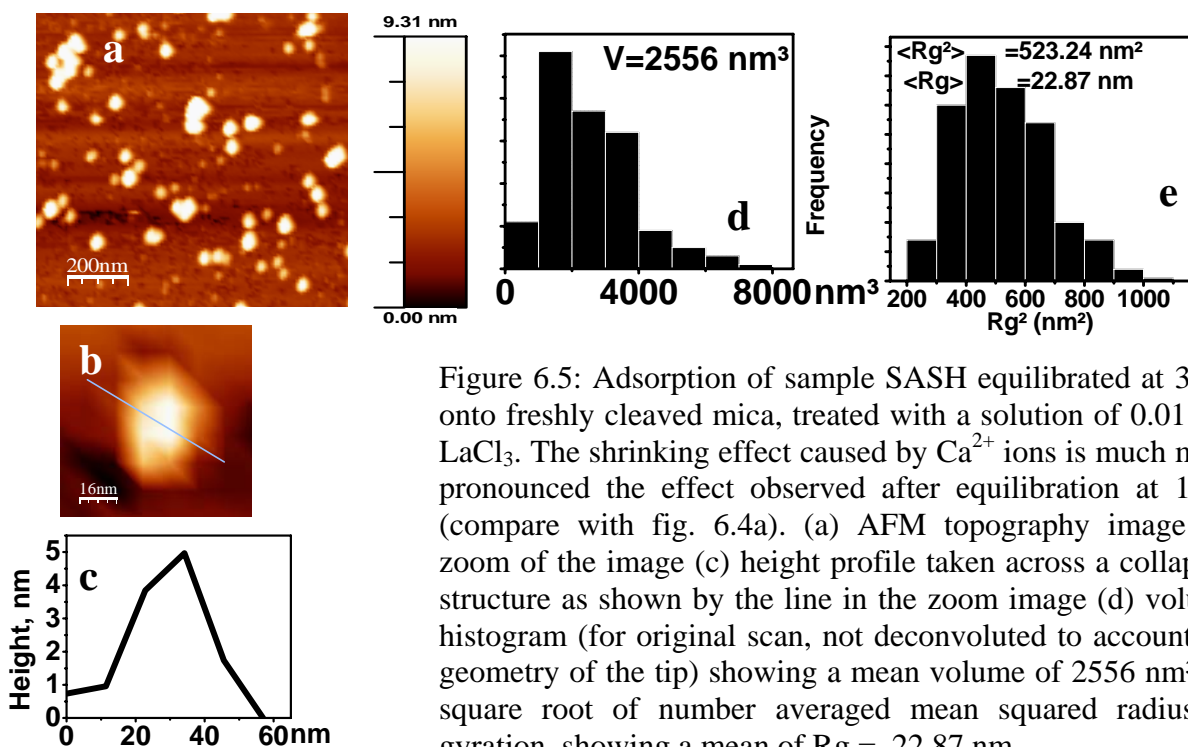
Figure 6.5: Adsorption of sample SASH equilibrated at 30°C onto freshly cleaved mica, treated with a solution of 0.01 g/L LaCl$_3$. The shrinking effect caused by Ca^{2+} ions is much more pronounced the effect observed after equilibration at 15°C (compare with fig. 6.4a). (a) AFM topography image (b) zoom of the image (c) height profile taken across a collapsed structure as shown by the line in the zoom image (d) volume histogram (for original scan, not deconvoluted to account for geometry of the tip) showing a mean volume of 2556 nm³ (e) square root of number averaged mean squared radius of gyration, showing a mean of Rg = 22.87 nm.

It is evident that at the higher equilibration temperature, the collapse shown by a polyacrylate coil is much more pronounced. The same trend is observed for SASH as the equilibration temperature goes from 15°C to 30°C. The exemplary AFM scans for SASH equilibrated at 15°C and 30°C along with their height profiles, volumes and radii of gyration are shown in fig. 6.4a-e (15°C) and fig. 6.5a-e (30°C).
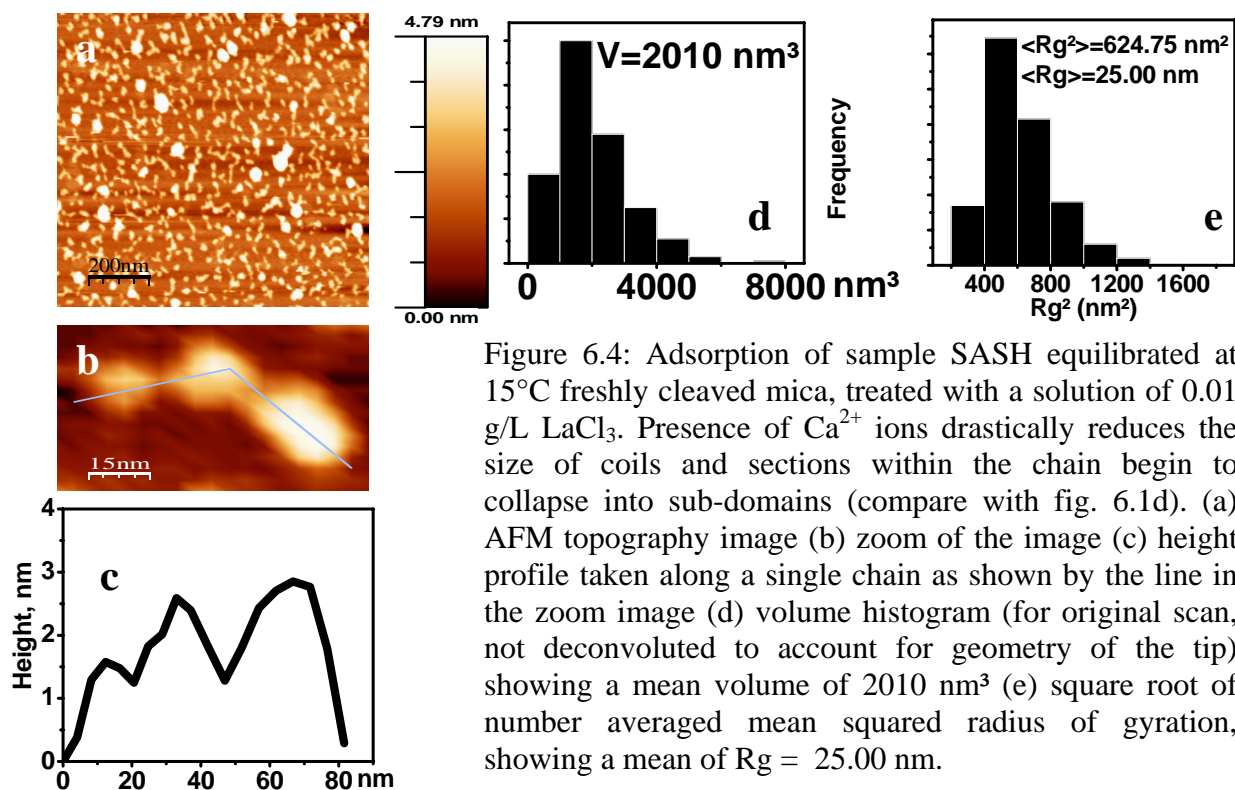
We shall take up the statistical analysis shortly, before which we should address the question of artifacts. AFM scans at the equilibration temperature of 15°C (Fig. 6.2a for SASE and Fig. 6.4a for SASH) show small globules and large clusters of polyacrylate chains in addition to partially collapsed polyacrylate coils. Similarly, both the AFM scans at the equilibration temperature of 30°C (Fig. 6.3a for SASE and Fig. 6.5a for SASH) show some clusters. It is believed that flux drying of surfaces, and the resulting capillary forces, may cause compaction of some coils into globules especially in case of weak polyelectrolytes.[119] This compaction further deteriorates the quality of adsorption on the surface and promotes coalescence of globules to clusters. The clusters were not included in our statistical analysis.

At this point, we would like to compare corresponding AFM scans of polyacrylates adsorbed on salt pre-treated mica surfaces and chemically modified mica surfaces. Fig. 6.6a-d shows exemplary AFM scans for SASE (15°C), SASE (30°C), SASH (15°C) and SASH (30°C), respectively, as adsorbed on chemically modified mica. Again, partially collapsed NaPA-Ca^{2+} chains further collapse with increase of equilibration temperature. What is noteworthy however is, that with the exception of SASE (15°C), very large structures are missing, indicating that this procedure inhibits aggregation upon drying of samples. This is true for both the equilibration temperatures. The clusters seen in SASE

(15°C) are very likely condensation products which result from silanization (refer Chapter 3, section 3.2.2). SASH (15°C), for example, does not show most of these large structures, giving credence to this speculation. Our observations regarding adsorption of weak polyelectrolytes on chemically modified mica surfaces are very much in line with similar observations made by Borkovec et al.[119]
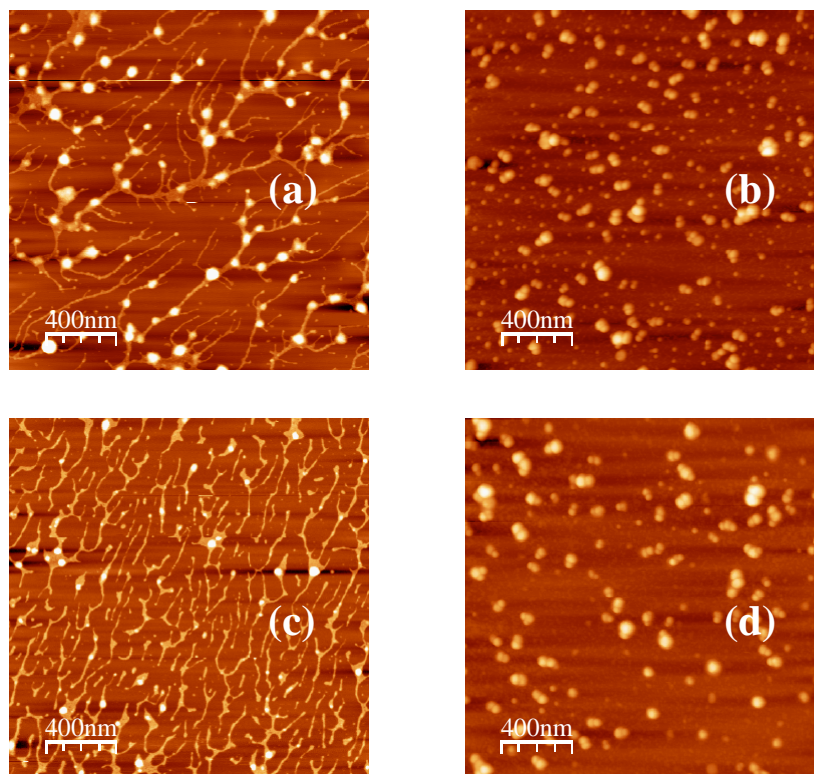
Figure 6.6: Adsorption of Ca-PA onto mica surface chemically modified using APDMES: (a) SASE equilibrated at 15°C; (b) SASE equilibrated at 30°C; (c) SASH equilibrated at 15°C; (d) SASH equilibrated at 30°C. Samples equilibrated at 30°C are considerably more collapsed than the samples equilibrated at 15°C. No pearl formation is observed at equilibration temperature of 15°C (SASE-15°C likely shows condensation products. Refer text.). Dumbbells dominate at equilibration temperature of 30°C.

We shall now return to Fig.6.2-6.5 for comparing surface and solution behaviors of NaPA-Ca^{2+} coils at both the equilibration temperatures. First of all, qualitatively, the picture can be described thus: when the conformation in solution is that of a random coil

(equilibration temperature of 15°C), the conformation on surface already begins to show signs of pearl growth. When the conformation in solution shows a pearl-necklace structure (equilibration temperature of 30°C), the conformation on surface is that of a tightly packed globule. It appears that there is a pre-emption of formation of intermediate states on the surface while the response in solution is a bit delayed. Nevertheless, it should be noted that an inevitable effect during AFM imaging of structures showing dense pattern of collapsed sub-domains is that it is extremely difficult to probe vertical features.[139] The well known tip broadening effect further accentuates the situation. Since at the equilibration temperature of 30°C, both SASE and SASH exhibit a far more pronounced collapse than at 15°C, it is possible that closely spaced spherical sub-domains at 30°C appear as completely collapsed globules on the AFM scan. We will pursue this point further in the next section. Although substrate-sample interactions are not very well understood,[127,129,140-142] they might have an important role to play in the observed pre-emption in the formation of intermediate states on surfaces, at least in this particular case. We have seen this pre-emption in a similar study earlier. It might be intriguing to draw parallels with fig. 2.25 in Chapter 2, section 2.4.4 and ref. 117 cited therein. But we would like to stop short of speculations.

Meanwhile, note that in the AFM scans of SASE and SASH equilibrated at 15°C (Fig. 6.6a and 6.6c respectively) which were adsorbed on chemically modified mica and flux dried, no distinct pearls along molecular contour are visible, thereby resembling the corresponding conformation in solution more closely. Similarly, AFM scans of SASE and SASH equilibrated at 30°C (Fig. 6.6b and 6.6d respectively) which were adsorbed on chemically modified mica show a large majority of dumbbells instead of tightly packed

globules, again resembling the corresponding conformation in solution more closely. However, the images shown in fig. 6.6a-d were not analysed quantitatively. One reason for this was our inability to isolate single molecules in images with samples equilibrated at 15 °C.

Similarly, we obtained single molecular root mean square radii of gyration which were slightly lower at the equilibration temperature of 30°C than at 15°C for both SASE and SASH. A comparison of R_g values obtained for SASE and SASH at the equilibration temperatures of 15°C and 30°C, from light scattering and AFM is given in Table 6.3.

Sample	[PA] g/L	[Ca^{2+}] mM	Volume nm^3	R_g (AFM) nm	R_g (SLS) nm	R_g(AFM)/ R_g(SLS)
SASE-15°C	0.2346	1.00	2693	23.17	38.3	~0.6
SASE-30°C	0.2346	1.00	2216	22.60	25.6	~0.9
SASH-15°C	0.1300	0.65	2010	25.00	52.8	~0.5
SASH-30°C	0.1300	0.65	2556	22.87	32.8	~0.7

Table 6.3: The radii of gyration calculated from AFM and light scattering show the same trends. The ratio R_g(AFM)/ R_g(SLS) is good for samples equilibrated at 30°C but is rather low for samples equilibrated at 15°C. This is explained in the text.

Exactly the same trends can be observed for both techniques. The ratio R_g(AFM)/R_g(SLS) (given that AFM evaluates the square root of number averaged mean squared while SLS evaluates the square root of z-averaged mean squared values) is good for samples equilibrated at 30°C but is rather low for samples equilibrated at 15°C. This discrepancy can be explained on two grounds: 1)We believe that at the noise levels at which experiments were done, a fully extended chain may largely remain invisible to an AFM scan. This will drastically reduce the average value of radius of gyration on

surfaces. Increased noise levels are expected due to H-D exchange at the surface 2) We would like to think of it as an advantage of AFM that the statistician can make an informed choice of ignoring aggregates during any evaluation. If these aggregates are also present in solution, though in very minute amounts, it will drastically increase the value of radius of gyration evaluated from SLS.

Finally, it is very relevant to mention that the observed coil collapse on surfaces was completely reversible, i.e., the drastic increase of the degree of collapse on increasing the temperature could be recovered by simply equilibrating the solutions prior to adsorption on equilibrated substrates.

6.3.3 Investigations at the phase boundary in reciprocal space

In order to probe deeper into the observed pre-emption in the formation of intermediate states on surfaces, we decided to do on the surface what scatterers do in solution. We have discussed in detail the evaluation of 2D form factor curve in Appendix A, section A2.3.2.2. Only confirmed single molecules were included in this analysis, irrespective of their shape. The criterion to qualify as a single molecule was chosen to be a case-by-case volume analysis of the structures visible on the AFM scan. Any structure with a significantly larger volume than the theoretically anticipated one was deemed to be an aggregate.[119] Likewise, any structure with a significantly lower volume was deemed to be a section of a coil, a large part of which has remained invisible to the AFM scan given the noise levels at which experiments were performed.[119] Fig. 6.7a-b show the 2D form factor curves for SASE and SASH equilibrated at 15°C and 30°C respectively. The curves have been shifted along the y axis for the purpose of clarity.
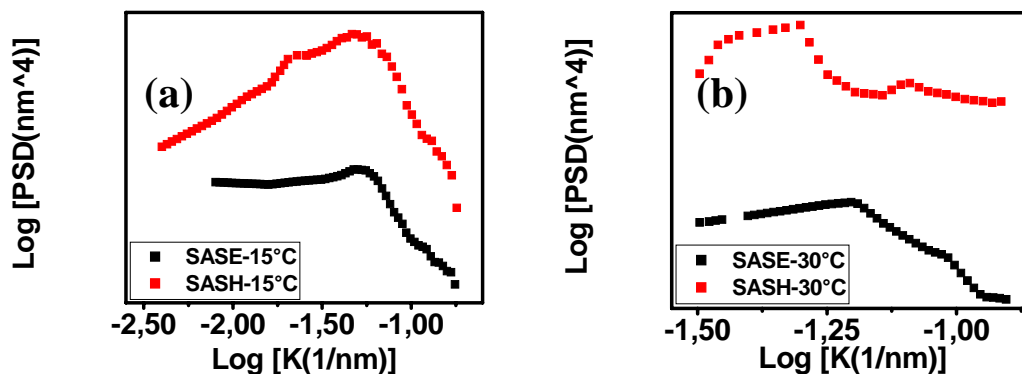
Figure 6.7: 2D form factor curves for (a) SASE and SASH equilibrated at 15°C. (b) SASE and SASH equilibrated at 30°C. Curves are shifted along the y axis for the purpose of clarity.

In lieu of an analytical or theoretical curve against which the generated 2D form factor curve can be fitted, relating the 2D form factor curve to the structure of the molecule is a challenging task. Fig. 6.7a shows 2D form factor curves for SASE and SASH equilibrated at 15°C. The curves have been shifted along the y axis for greater clarity. SASE shows only one characteristic correlational peak at Log K = -1.32 corresponding to a length scale of 20.89 nm. SASH exhibits two correlational peaks- a higher intensity peak at Log K= -1.33 corresponding to a length scale of 21.38 nm as well as appearance of a low intensity peak at Log K = -1.64 corresponding to a length scale of 43.65 nm. We have interpreted these length scales to be reflective of the average separation between pearls[143] which begin to form along the molecule as it adsorbs on the substrate. At 0.01 M total salt concentration, the coil has enough counterions in its proximity. When such a coil from solution is deposited on the surface, the loss of one degree of freedom causes a rapid confinement of the polymer backbone. This creates sections within the molecule having a very high density of counterions. It is these sections which interact very strongly with recharged mica surface and are sensed by the 2D form factor. The presence of the

first length scale at around 21 nm is exhibited in adsorbed molecules from both SASE and SASH. However, it is the presence of a quite distinguishable second length scale at 43.65 nm in SASH which is striking. An explanation for this observation may lie in the non uniform distribution of charge along the chain in solution, especially in case of annealed polyelectrolytes like polyacrylic acid. As discussed in Chapter 2, section 2.1.5, it is predicted that a finite polyelectrolyte chain in dilute aqueous solution will incur an accumulation of charge towards its ends and a slight depletion of charge in its middle. The logic behind this predicted end effect is that a charge has lesser neighboring charges towards the ends of the chain than in its middle. Thus, electrostatic potential energy of a charge is minimized more towards the ends. Since an excess charge tends to accumulate towards the chain ends, the farther a section of the chain is from the middle, the stronger its interaction would be with recharged mica substrate during adsorption. This results in formation of larger pearls as one moves farther from the middle of the chain. The 2D form factor is able to sense this minute detail in case of SASH but not in case of SASE. This can happen if SASH, in general, adopts a more extended conformation of molecules on the surface as compared to SASE since it is only when a molecule is extended that electrostatic potential energy at different locations of the chain would be different. On similar lines, we may speculate that greater the extension exhibited by an adsorbed molecule, larger the number of low frequency peaks which appear in the 2D form factor curve. Not only should the number of low frequency peaks increase with increasing extension of the adsorbed molecule, but also the intensity of such peaks. This follows from the predicted increase of charge accumulation as one moves farther from the middle of the chain. In a nearly rigid rod conformation, the lowest frequency peak in the 2D form

factor curve would be quite intense and correspond to the end to end distance of the adsorbed molecule. However, we have not experimentally verified our predictions regarding the response of 2D form factor curve to increasing extension of adsorbed molecules. Such a study may be conducted using a large number of samples with known solution conformations ranging from randomly coiled to nearly rigid rod and then analyzing the 2D form factor curve for each sample.

SANS results for sample solutions equilibrated at 15°C indicate a randomly coiled behavior for SASE and a rather extended behavior for SASH. Note that this subtle difference between two samples is reflected even on the surface as observed in their respective 2D form factor curves and explained above. Pearl formation begins on the surface which is not identifiable in solution. We can therefore argue that interactions associated with sample history have pre-empted the formation of an intermediate coil to globule state on the surface.

Fig. 6.7b shows 2D form factor curves for SASE and SASH equilibrated at 30°C. As before, the curves have been shifted along the y axis for greater clarity. We can immediately observe two noticeable differences between the 2D form factor curves evaluated at equilibration temperature of 30°C and the corresponding curves at equilibration temperature of 15°C. First, the correlation peaks at equilibration temperature of 30°C have shifted to a higher frequency range. This would mean a temperature induced collapse of molecules. Second, we observe that the low frequency correlation peaks at equilibration temperature of 30°C are much sharper than the peaks at equilibration temperature of 15°C. This can be interpreted to mean that there is a great degree of uniformity in the lateral structures adopted by different molecules adsorbed on

the surface. If this would not have been the case, the averaging process would have broadened the peaks as seen in the 2D form factor curves evaluated at equilibration temperature of 15°C.

SANS results for sample solutions equilibrated at 30°C also indicate pearls of SASE and SASH with an average separation of 80.0 nm. The situation on surface, as summarized in Table 6.4, is as follows.

15°C		30°C	
SASE	SASH	SASE	SASH
Log K = -1.32 (20.89 nm)	Log K = -1.33 (21.38 nm)	Log K = -1.20 (15.85 nm) R = 0.20	Log K = -1.30 (19.95 nm) R = 0.20
	Log K = -1.64 (43.65 nm)	Log K = -1.01 (10.23 nm) R = 0.12	Log K = -1.09 (12.30 nm) R = 0.15

Table 6.4: Data table showing the frequencies at which correlation maxima are observed. The respective correlational lengths are mentioned within brackets. SASE and SASH at equilibration temperature of 30°C show the presence of pearls in solution (as analysed through SANS) with separation between pearls at 80.0 nm. The ratio between on-surface correlation lengths and separation between pearls in solution is indicated by the symbol "R".

Two correlation maxima can be observed for both SASE and SASH. The high intensity peak occurs at low frequency (Log K = -1.20 in SASE and Log K = -1.30 in SASH) in either of the samples. The corresponding correlational lengths are 15.85 nm and 19.95 nm respectively. The second correlation maxima is weak in both the samples and is in fact, almost completely smeared out in SASE. The frequencies Log K = -1.01 for SASE and Log K = -1.09 for SASH correspond to length scales of 10.23 nm and 12.30 nm respectively. We interpret the observed length scales to represent the average separation between pearls formed on the surface. Since the situation on surface shows two, not just

one, correlation length scales for either sample, we may speculate that there are two kinds of pearls observed on the surface.

The coils of both SASE and SASH show the existence of a pearl necklace structure in solution. Since it is the pearls which carry most of the charge in a pearl necklace structure, we anticipate that when this pearl necklace moves closer to the recharged substrate, the pearls interact more strongly with the surface than the intervening strings. As such, it may be safe to assume that the strongest intensity peak observed in the 2D form factor is related to the existence of pearls in solution. In this case, a nearly constant ratio of 0.2 between pearl separation distance on surface and the corresponding separation distance in solution is observed in both SASE and SASH A five fold decrease of pearl separation distance upon adsorption is remarkable. It points to isotropic adsorption (rather than a flat one) under weak adsorption forces. On similar lines, we find that the second correlation length scale, in both SASE and SASH, also bears a constant ratio of 0.12-0.15 with the pearl separation distance in solution. Although preliminary, most likely, it points to the following picture. As the pearl necklace structure moves from solution to surface, the pearls interact strongly with recharged substrate. As such, they form the first points of adsorption and give rise to strong peaks in the 2D form factor curve. The remaining lateral packing arrangement of the molecule is strongly dictated by these fixed adsorption points. Electrostatic interactions between the molecule and the surface give rise to formation of more pearls whose locations are ultimately governed by the fixed adsorption points.

Summary and outlook

Specifically binding ions induce the transition of anionic polyacrylate coils from extended conformation to collapsed globules passing through a cascade of intermediate states when solution conditions approach the L-type precipitation threshold. It is the conformation of these intermediate states on surfaces and in solution which is at the focus of this thesis. In comparing the surface and solution conformations of intermediate states, we were able to qualitatively and quantitatively underline the effects of sample history. Two types of quantitative comparisons have been emphasized. In real space, the radius of gyration values of adsorbed molecules have been evaluated incorporating fully the x, y and z axes. These values have been compared with radius of gyration values of the very same sample solution obtained using SLS. In reciprocal space, a novel image processing protocol has been used to generate the 2D form factor curve wherein the correlation maxima have been compared with corresponding maxima obtained for the very same sample solution using small angle scattering techniques like the SANS.

The influence of bivalent ions, respectively, Strontium, Lead and Calcium, on the shape of polyacrylate coils is studied. In the last case, temperature has been introduced as a secondary parameter to shed further light on the mechanism by which polyelectrolyte-bivalent ion complexation takes place. Both scattering and AFM experiments reveal formation of necklace-like structures as intermediates for NaPA-Sr^{2+} system. Since the mol. wt. of the NaPA coils used was relatively large in this case, adsorption on mica surfaces was strong. Under such conditions, the molecules undergo a z collapse upon flux drying but do not get altered in x and y directions. The ratio $R_g(AFM)/R_g(SLS)$ was found to be in the range 0.7-0.9. The remaining (insignificant) differences in the R_g

values arise due to the fact that AFM gives the square root of number averaged mean squared radius of gyration while SLS gives the square root of z-averaged mean squared radius of gyration. The differences in radius of gyration values observed in solution and on surfaces were more prominent for NaPA-Pb^{2+} system. Again, although both scattering and AFM reveal necklace-like structures as intermediates, the ratio R_g(AFM)/R_g(SLS) was now found to be nearly 0.6. The fact that R_g(AFM) is the square root of number averaged and R_g(SLS) is the square root of z-averaged mean squared radius of gyration, alone cannot explain this low value. Since the mol. wt. of NaPA coils used in this case was quite low, adsorption on mica surfaces was weak. Under such conditions, the molecule does not only undergo a z collapse upon flux drying, but also shrinks in the x and y directions due to capillary forces. Finally, with NaPA-Ca^{2+} system, the picture did not show a one-to-one correspondence between solution and surface conformations at all. In fact, it showed a one-step-ahead correspondence. As already stated, the coil to globule transition was induced by increasing the equilibration temperature from 15°C to 30°C in this case. SANS could not identify any necklace-like intermediates in solution at the equilibration temperature of 15°C while AFM scans at this temperature showed the beginning of formation of pearls. Likewise, at the equilibration temperature of 30°C, SANS could identify necklace-like intermediates in solution with a large majority of dumbbells while AFM scans at this temperature showed a mix of dumbbells, sausage-like structures and globules. Indeed, we were witnessing an accelerated coil to globule transition on surfaces as compared to the situation in solution resulting in a pre-emption in the formation of intermediate states on surfaces. Since the ratio R_g(AFM)/R_g(SLS) (given the square root of number averaged and the square root of z-averaged mean

squared values respectively) at the equilibration temperature of 30°C showed a range of 0.7-0.9 indicating strong adsorption of the relatively high mol. wt. NaPA coil on mica surfaces, our suspect were the substrate-sample interaction forces. The AFM scans were therefore analysed with 2D form factor curves, a better protocol when no assumptions about the shape of adsorbed molecules are made a priori, to trace the effects of sample history.

The thesis establishes the general utility of AFM to capture the essential features of a collapsing coil which the very coil exhibits in solution. The shape of the coil on surface and in solution may not be exactly the same, yet reveal the same characteristics. The comparative advantages and disadvantages of salt pre-treated mica surfaces and chemically modified mica surfaces have been brought out. Finally, a definitive new insight is gained as regards the mechanism of coil collapse induced by specifically binding ions. The entropic nature of the process as well as the visualized shape of the collapsing intermediates does not support a mechanism along an electrostatically driven shrinking with linear, rod-like arrays of pearls as intermediates. On a molecular level, it is the liberation of water molecules and Na^+ ions which promotes binding of bivalent ions to COO^- residues. This binding in turn increases the hydrophobicity of the polyacrylate chains. As a consequence, the chains shrink due to an increased propensity for polymer-polymer contacts (and finally precipitate).

Investigation of the coil shrinking mechanism is of major relevance to many processes in solution and at interfaces between solution and solid particles, both in nature and industry.[144-145] For example, often COO^- groups of proteins and polysaccharides form complex bonds to calcium ions, leading to distinct conformational changes. This in turn

modifies the biological activity of the polymers involved in such complex reactions as blood clotting and muscular contraction. The resulting adsorption of synthetic polyelectrolytes can also induce a variety of processes such as mineral separation,[146-147] flocculation,[148-149] retention,[150] strength-enhancing additives in paper production,[151] colloid stabilization[152-154] and coatings.[155-158] Polyelectrolyte gels which can instantly change their dimensions upon changing the environmental parameters are also of great interest. Due to their unique capability of reversible contraction they are used in practice as material for a variety of biomedical applications.[159-162] Consider, for example, the fascinating uses these polyelectrolytes have to offer as drug carriers and controlled release systems.

Besides, the study of shape of single adsorbed molecules using the 2D form factor curve can be of importance in a variety of fields including nano-optics,[163-164] nano-electronics,[165] micro-fluidics[166] and sensor technology.[167-169] Understanding the electrical, optical or mechanical properties of single molecules after they adsorb on a surface is central to advancements in these areas. These properties are very often governed by the surface morphology of the molecule including, but not limited to, its surface roughness. In such a scenario, Power Spectral Density (PSD) curves generated using Tapping Mode AFM can be a very useful new tool for precise analysis of surface morphologies, roughness and defect characterization of nano components.

The thesis is an apt background for research level academicians as well. Various interesting cases can be thought of. Polystyrene sulfonate, for example, is known to be a quenched polyelectrolyte (in contrast to polyacrylate which is annealed) which shows both a H-type precipitation (following the law of mass action) with ions like Ca^{2+} as well

as a L-type precipitation (chemical complexation different from the law of mass action) with ions like Al^{3+}. The question which needs to be probed here is whether the two different types of precipitation lead to the same structural single chain intermediates (Appendices C4 and C5). The AFM statistician can take some respite in the fact that polystyrene sulfonates, with their bulky backbones, have proven to be easy to image using mica surfaces modified with octylamine-chloroform solution (Appendix C3).

Polystyrene sulfonates containing specifically binding ions from the alkaline earth group also adsorb on pristine (untreated) mica surfaces. However, they show unidirectional stretching under the shear flow. This stretching is speculated to be cyclic, i.e., stretched and coiled conformations exist at the same time (Appendix C5). It might be very interesting to see if Brownian Dynamics simulations can rationalize this behavior observed experimentally through AFM.

This thesis describes the use of Sr^{2+}, Pb^{2+} and Ca^{2+} as specifically binding ions for polyacrylates. In the last case, temperature has been introduced as a secondary parameter. A natural corollary to this work would then be to investigate the collapse behavior of polyacrylates induced by a transition metal ion. The most interesting case that comes to our mind is presented by Ag^+. Silver ions are expected to exert specific interactions with COO^- residues while being monovalent and thus exhibiting electrostatic properties comparable to those of sodium ions. Huber et al.[170] have already analysed the solution behaviour of such complexes using scattering techniques. Only if the Ag^+ content was lowered to 1 - 2 Ag^+ ions per 100 COO^- residues could a precipitation be avoided and a noticeable shrinking of the PA coils be detected. If these solutions were exposed to UV-light for a definite time, the apparent molar mass in the respective samples increased

drastically while the size of the identified domains, originally attributed to single coils, further shrank. The solutions also revealed a plasmonic band characteristic for Ag-nanoparticles. Results could be interpreted as follows. The isolated anionic polyacrylate coils act as sinks for the Ag^+ cations, leading to high local Ag^+ concentrations. Exposition of these Ag-decorated PA chains with UV-light induced a reduction of Ag^+ to small metallic silver particles. Exposition of pure $AgNO_3$ solutions without NaPA did not cause any changes. Apparently, Ag^+ reduction does not only require UV-light but the coexistence of appropriately designed "clouds" of COO^- groups, which may be involved in this reduction. The results point to new and exciting applications of NaPA as a tool to control Ag-particle formation on a nanometer scale. Can this behaviour be trapped on surfaces and visualized using AFM?

Further experiments can be designed to develop morphological models for coil collapse. For example, sodium salt of PA-PEO-PA blockcopolymer with a neutral polyethyleneoxide block at the center and anionic polyacrylate blocks at the termini also interact with the same metal cations as used in this thesis. If the blockcopolymers occur as single chains, its limiting shape resulting from an M^{2+} induced shrinking process may be a dumbbell. In this case, the dumbbell structure will be revealed by appropriate ASAXS experiments focusing on the interacting M^{2+} cations and SANS experiments if suitably deuterated blockcopolymers are available. If the blockcopolymer has a strong propensity to aggregate, this process may lead to new controllable structures by the interaction with M^{2+}. In either case this model architecture may lead to interesting and new structures which would be extremely suitable to test the hypothesis that an AFM

experiment reveals the 3D structure of a dissolved species in solution and further, to understand the mechanism of coil collapse.

Finally, simulations can establish the link between AFM and light scattering data. A computer simulation performed using a model directly applicable to our case may be used to theoretically establish the transversal and lateral chain sizes of adsorbed molecules as a function of the degree of confinement, surface charge density and radial/tangential direction of shear fields created during drying procedures. The solution behavior of the same coils can also be analysed using computer simulations to arrive at a theoretical form factor curve. Comparisons of the three techniques- AFM, scattering and simulations, would be the most comprehensive picture that can be made available for understanding the mechanism of coil collapse.

Research techniques and data processing protocols

A1 The necessity for a holistic approach

Polyelectrolytes pass through a cascade of intermediate states along the coil to globule transition. These intermediate states are known to respond quite sensitively to parameters like amount of added salts, pH, temperature, solvent quality etc. While on one hand, this is quite promising for biological and material applications, on the other, important questions still remain to be answered. One major gap in efforts so far has been the perceptible lack of a complete picture encompassing both solution and surface behaviors of these intermediate states under exactly the same conditions of salt, pH, temperature and solvent quality. Thus, for example, light scatterers have used SLS, DLS, (A)SAXS, SANS etc. to study the stimulus-response of intermediate states in solution, microscopists have underscored the immense utility of AFM to study independently the stimulus-response on surfaces. How much does the solution and surface conformations of these intermediate states differ remains an open question. A holistic approach to the problem necessitates that intermediate states be first characterized in terms of shape and size in solution and then the very same samples be adsorbed on surfaces to study them through AFM. Differences can then be clearly brought out and established quantitatively. In what will follow, we first describe AFM and the various image analysis techniques used in this work. We shall also comment upon the scattering techniques used to study the solution behavior of intermediate states.

A2 Atomic Force Microscopy: Tapping Mode[171]

Any microscope which consists of a sharp physical probe scanning across a sample surface and monitors, in real time, some kind of probe-sample surface interaction is

classified as a Scanning Probe Microscope (SPM). This category can be subdivided into

Scanning Tunneling Microscopes (STM), Atomic Force Microscopes (AFM) (also

sometimes called Scanning Force Microscopes (SFM)), Magnetic Force Microscopes

(MFM) etc. AFM, the SPM used for this work, was developed in 1986 by Binning, Quate

and Gerber as a collaboration between IBM, Zurich and Stanford University.

There are three primary modes in which an AFM can operate. They are contact mode,

non-contact mode and tapping mode (TM). We shall confine ourselves to AFM-TM

(henceforth, just AFM) here because it was the mode of choice for all experiments in this

thesis. The reader is referred to ref 171 for an excellent overview of all the modes of

AFM.

A2.1 Principle

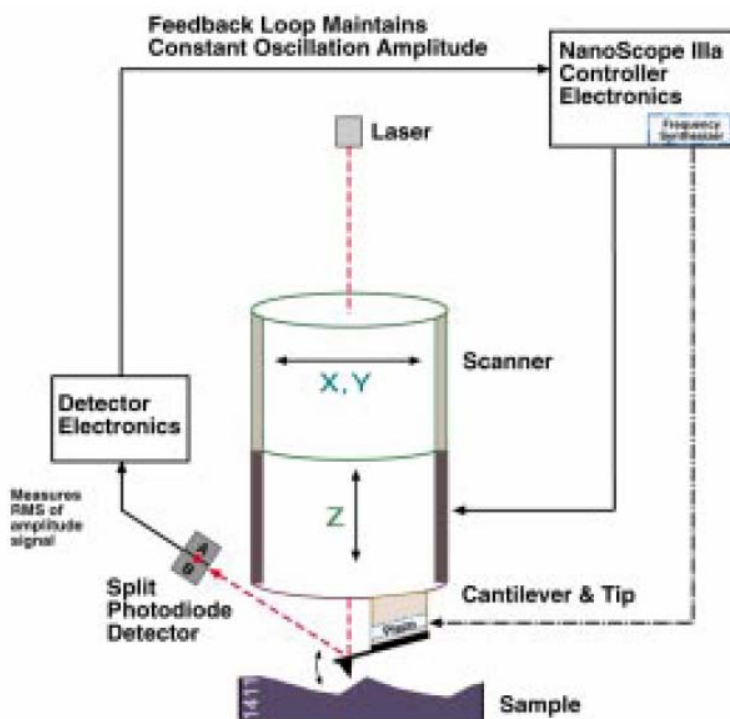Fig. A1 depicts the principle behind AFM-TM.

Figure A1: The principle of Tapping Mode Atomic Force Microscope (adopted from ref [171])

AFM-TM operates by scanning a tip attached to the end of an oscillating cantilever across the sample surface. The cantilever is oscillated at or near its resonance frequency with an amplitude ranging typically from 20 nm to 100 nm. The tip lightly "taps" on the sample surface during scanning, contacting the surface at the bottom of its swing. The feedback loop maintains a constant oscillation amplitude by maintaining a constant RMS of the oscillation signal obtained by the split photodiode detector. The vertical position of the scanner at each (x,y) data point in order to maintain a constant "setpoint" amplitude is stored by the computer to form the topographic image of the sample surface. By maintaining a constant oscillation amplitude, a constant tip-sample surface interaction is maintained during imaging. When imaging in air (i.e., flux drying the sample surface before imaging as is the case in this thesis), the typical amplitude of the oscillation allows the tip to contact the sample surface through the thin adsorbed solvent layer without getting stuck.

The AFM-TM offered us the following advantages as regards the current work.

1) Higher lateral resolution on most samples (upto 5 nm)

2) Lower forces and less damage to soft samples imaged in air

3) Lateral forces virtually eliminated, so there is no scraping

A2.2 Instrumentation

As can be seen from fig. A1, there are three most important parts of an AFM instrument which require some detailing- scanner, cantilever and tip and split photodiode detector. Lets pick them up one by one.

1) Scanner- AFM scanners are made of piezoelectric materials, hence the name piezoscanners. Piezoelectric materials expand or contract proportionally to an applied

voltage. Whether they expand or contract depends upon the polarity of the voltage applied.
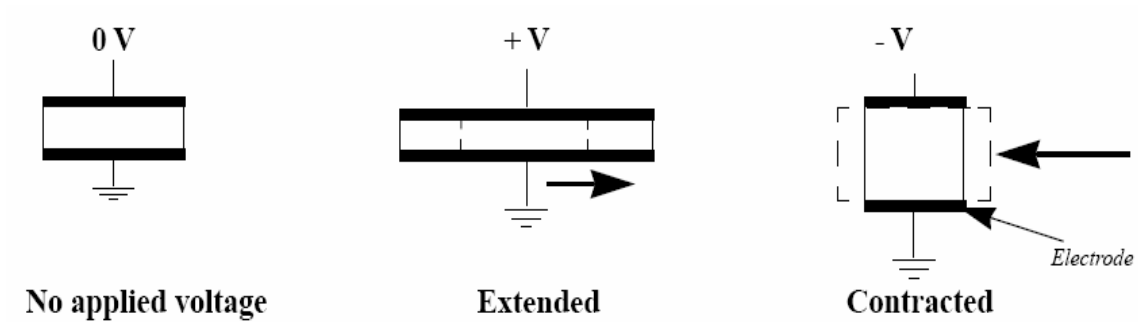

Figure A2: The effect of applied voltage on a piezo electrode (adopted from ref [171])

A piezoscanner is constructed by combining independently operated piezo electrodes, like the one shown in fig. A2, for X, Y and Z into a single tube, forming a scanner which can manipulate sample surfaces or probes with extreme precision in three dimensions. A graphical representation of a piezoscanner is shown in fig. A3.
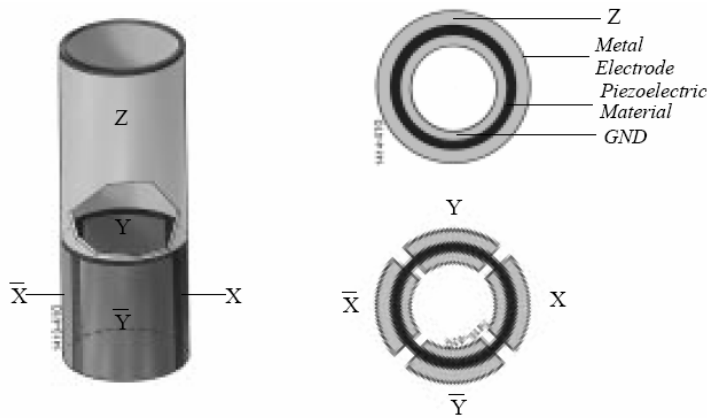

Figure A3: A typical piezoscanner and X,Y,Z configurations (adopted from ref [171])

AC voltages applied to different piezo electrodes of the scanner produce a raster motion of the latter in X and Y. Customarily, the slow scan axis is designated as the Y axis and

the fast scan axis is called the *X* axis. We have followed the same convention throughout

this thesis. The raster motion of a piezoscanner is represented in fig. A4.

Figure A4: Schematic of the raster motion of a piezoscanner (adopted from ref. [171])

2) Cantilever and tip- Silicon probes are primarily used in Tapping Mode AFM. The tip

and cantilever on which it is mounted are an integrated assembly of single crystal silicon,

produced by etching techniques. These probes can be much stiff resulting in large spring

constants and resonance frequencies. Fig A5 shows SEM image of a silicon cantilever

and tip and tabulates the most important characteristics.

Spring constant	Up to 100 N/m	
Resonance frequency	200-400 KHz	
Tip radius	5-15 nm	
Cantilever length	125 µm	
Cantilever configuration	Single beam	
Reflective coating	Uncoated usually (optional Al coating)	

Figure A5: Most important characteristics and SEM image of a silicon cantilever and tip (adopted from ref. [171])

3) Split Photodiode Detector- The split photodiode detector is the most commonly used form of cantilever deflection detection. Laser light from a solid state diode is reflected off the back of the cantilever and collected by a position sensitive detector consisting of two closely spaced photodiodes whose output signal is collected by a differential amplifier. Angular displacement of cantilever results in one photodiode collecting more light than the other photodiode, producing an output signal (the difference between the photodiode signals normalized by their sum) which is proportional to the deflection of the cantilever. The schematic is shown in fig. A6. In principle, cantilever deflections less than 1°A can be detected. Long beam path, of the order of several cm, amplifies changes in beam angle.
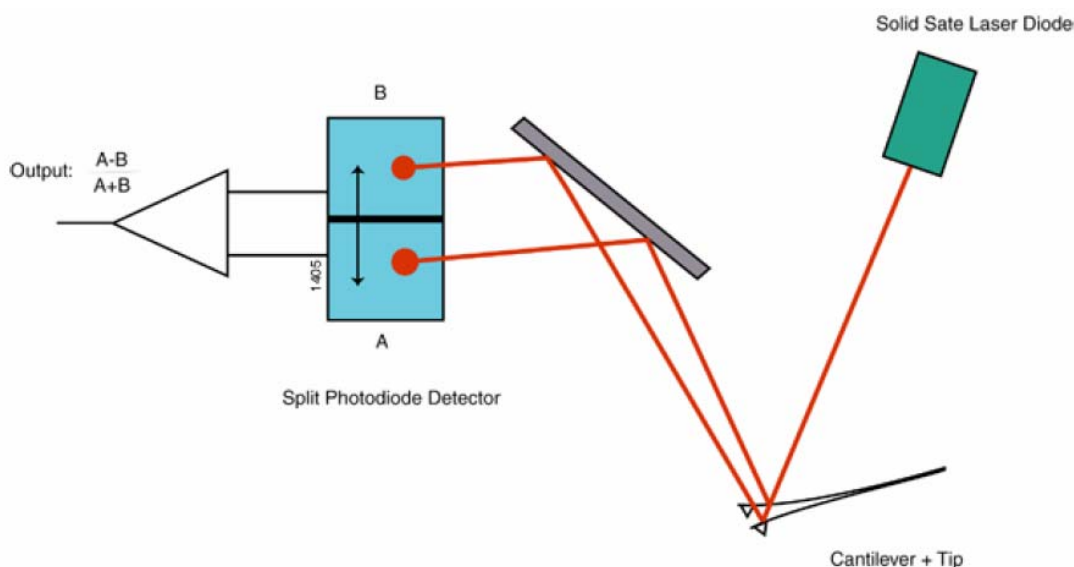

Figure A6: Schematic showing the working of a split photodiode detector (adopted from ref. [171])

A2.3 Analysis of AFM images

For quantitative analysis of AFM images, WSxM software suite,[172] MATLAB and OriginPro were used, as specified. AFM images were analysed both in real and reciprocal

space.

A2.3.1 Analysis in real space

A2.3.1.1 Single molecular volume

Our first emphasis was to prove that we have been indeed able to visualize single molecules and not clusters. This was made necessary because of the restriction to work with high polyelectrolyte concentrations. Recall that a good form factor analysis using scattering techniques requires a concentration of at least 0.1 g/L of the specie under investigation. This is two orders of magnitude higher than the concentration of 0.001 g/L usually recommended for single molecule studies on surfaces. Thus, the risk of agglomeration during adsorption was quite high and required a strong verification procedure. This was achieved by establishing volume histograms for the structures visible on the surface. If the calculated volumes were close to theoretically anticipated single molecular volumes, we could claim that the structures visible on the AFM scan were single molecules and not agglomerations.

The theoretical single molecular volume could be easily estimated as follows. Let the molecular weight of the polyacrylic acid under consideration be M a.m.u. The number of monomer units in a single molecule belonging to this polyacrylic acid would then be $\dfrac{M}{72}$, the denominator representing the a.m.u. weight of one monomer unit of polyacrylic acid. Now, let us calculate the volume of one monomer unit. Let the monomer unit be represented as -CH$_2$-CH(COOS)- where S is the specifically binding ion. The a.m.u. weight of this monomer unit is $71+(M_S/2)$ where M_S is the a.m.u. weight of the specifically binding ion, S. Note that only half its weight is included because the specifically binding ion is assumed to bond to at least two monomers. Assuming the dry

state density of the system to be 1g/cc, we can approximate the volume of one monomer

unit to be $\left(71+\dfrac{M_S}{2}\right)/N_A$ cc or $\left(71+\dfrac{M_S}{2}\right)10^{21}/N_A$ nm³ where N_A is the Avagadro's

number. The theoretical single molecular volume would then be

$$\left(\dfrac{71+\dfrac{M_S}{2}}{N_A}\right)\left(\dfrac{M}{72}\right)10^{21} \text{ nm}^3.$$

Volume histograms were generated using the built in "flooding" parameter of WSxM

software suite for each surface structure individually. This parameter allows the selection

of a minimum threshold height in close agreement with mica surface roughness and

evaluates the volume of the structure above the threshold. Similar methods have already

been used for size analysis of structures on AFM images.[173-174]

It is to be noted that mean volumes shown by volume histograms can be slightly higher

than the volume predicted theoretically. This is due to the well known tip broadening

effect. Deconvolution to account for the geometry of the tip should bring the

experimentally obtained mean volumes very close to those theoretically anticipated.

A2.3.1.2 Single molecular radius of gyration

Once volume histograms for the structures on the AFM scan proved that we have

obtained single molecules, other characteristics were evaluated. The most important of

these was the single molecular radius of gyration which gave us an idea of the shape of

the molecule in three dimensions.

Radius of gyration histograms were generated using ASCII data from AFM images and

evaluating eq A1 for each molecule individually. The same thresholding method was

used as applied for the volume histograms.

$$R_g^2\left(X,Y,Z\right)=\left\langle X^{\,2}\right\rangle+\left\langle Y^{\,2}\right\rangle-\left\langle X\right\rangle^2-\left\langle Y\right\rangle^2 \tag{A1}$$

where

$$\left\langle X^{\,2}\right\rangle=\sum_i X_i^{\,2}Z_i \Big/ \sum_i Z_i \text{ and } \left\langle X\right\rangle=\sum_i X_iZ_i \Big/ \sum_i Z_i$$

$$\left\langle Y^{\,2}\right\rangle=\sum_i Y_i^{\,2}Z_i \Big/ \sum_i Z_i \text{ and } \left\langle Y\right\rangle=\sum_i Y_iZ_i \Big/ \sum_i Z_i$$

Eq. A1 was evaluated using a home written MATLAB code, produced in Appendix B.

Note that the raw image produced by the AFM is an array of values $V_z(V_x, V_y)$ where V

denote voltages applied to the piezos responsible for motion in the X, Y and Z directions.

The generation of ASCII data, $Z(X,Y)$ from the raw AFM image, $V_z(V_x, V_y)$ usually

creates an error $\pm3\%$ for either of X, Y or Z axes assuming that the piezos are well

calibrated.[175] X_i, Y_i and Z_i in the relations cited above are the ith piezo displacement values

of X,Y and Z respectively obtained after thresholding. It must also be mentioned that the

sample height may not be necessarily equal to the Z piezo displacement. This happens

because the force experienced by the tip varies non linearly with tip-sample separation

distance. Since the amplitudes involved in the "light" tapping mode configuration are

rather large, complicated force vs. tip-sample separation curves may result. An error

analysis for this phenomenon may require numerical solutions and is neither within the

scope of this thesis, nor the purpose of this thesis.

The R_g values so evaluated are the best one parameter estimate of the 3D structure of the

molecule adsorbed on the surface. They however should not be thought of representing

the mass distribution inside the molecule.

A2.3.1.3 Other profile measurements for single molecules

Some other parameters were also evaluated in real space, as and when deemed necessary.

In Chapter 4, for example, we have established a comprehensive picture of the NaPA-Sr^{2+} system as we approach or depart the phase boundary. At the phase boundary, extensive investigations have been performed for the presence of intermediate states associated with the collapse transition. Several characteristics of these intermediate states have been tabulated like height of pearls, height of molecule between two pearls, number of pearls per molecule, separation between pearls and contour length.

A2.3.2 Analysis in reciprocal space

A2.3.2.1 The PSD master curve

Another important aspect which had to be emphasized was to prove beyond reasonable doubt that there were no shear fields and inter-particle correlations present on the surface. This stems from the fact that we were not only working with higher concentrations of polyelectrolytes (which could have lead to strong inter-particle correlations on the surface), but at the same time, we were trying to adsorb negatively charged polyelectrolytes on (negatively charged) mica surfaces (which made the presence of shear fields on the surfaces a real possibility). Mica, on the other hand, was not a replaceable choice of substrate for us because its unique atomic flatness allows single molecular resolution.[116-119, 176-177] As such, all AFM scans were analysed for absence of shear fields as well as inter-particle correlations before any further statistical treatment was carried out. Power Spectral Density (PSD) analysis was used to verify their absence.

A randomly rough sample surface scanned through a tapping physical probe shows the presence of many different spatial frequencies. This is quantitatively expressed by the PSD curve, giving the relative strength of each roughness component as a function of

spatial frequency. Mathematically, PSD is evaluated by squaring the magnitude of the Fourier Transform of a sample surface.

For an AFM scan, the Fourier Transform usually evaluated is the 2D-Fast Fourier Transform (2D-FFT). It is defined according to eq. A2 below[178]

$$2D-FFT(K_x, K_y) = \left(\frac{L}{N}\right)^2 \sum_{x=0}^{N-1}\sum_{y=0}^{N-1} z(x,y) \left[\cos\left\{2\pi\left(\frac{K_x x}{N} + \frac{K_y y}{N}\right)\right\} + i\sin\left\{2\pi\left(\frac{K_x x}{N} + \frac{K_y y}{N}\right)\right\}\right] \text{ (A2)}$$

where L is the size of the image, N is the number of pixels per line, $z(x,y)$ is the topographic height at the piezo displacement coordinates, (x,y) and (K_x, K_y) are the corresponding spatial frequency coordinates. Since only real numbers can be displayed, the magnitude of 2D-FFT calculated according to eq. A2 forms the spectral presentation of the Fourier Transform of an AFM scan. The 2D-FFT is converted into a PSD by an angular average using the radius in reciprocal space as the spatial frequency according to eq. A3 below[178]

$$PSD(K_\theta) = \left(\frac{1}{L}\right)^2 \sum_{n=0}^{N} \left|2D-FFT(K_x, K_y)\right|^2$$

where $\quad K_\theta^2 = K_x^2 + K_y^2$ $\hspace{6cm}$ (A3)

PSD then evidently carries the dimensions (length)[4]. In the derivation of eq. A3, PSD is normalized by the number of pixels of every K_θ. This is done because the number of pixels contributing to the averaging process increases as K_θ increases. In this way, we also make sure that intensities of correlation maxima, if any, occurring at different spatial frequencies can be compared and conclusions drawn.

We began by analyzing rotational isotropy in the spread of molecules on the surface and exclude the possibility of the presence of any shear field during drying procedures. Thus, 2D-FFTs of the scanned images were evaluated. An exemplary 2D-FFT is shown in fig. A7a. If a circular ring of intensity was visible in reciprocal space, it indicated rotational isotropy in the distribution of molecules. This would mean negligible or no presence of shear forces on the surface.

In the next step, PSD curves were evaluated for images of two different scan sizes (of the same sample surface) by angular averaging of the respective 2D-FFTs. These PSD curves were then merged into a master curve as exemplified in fig. A7b.
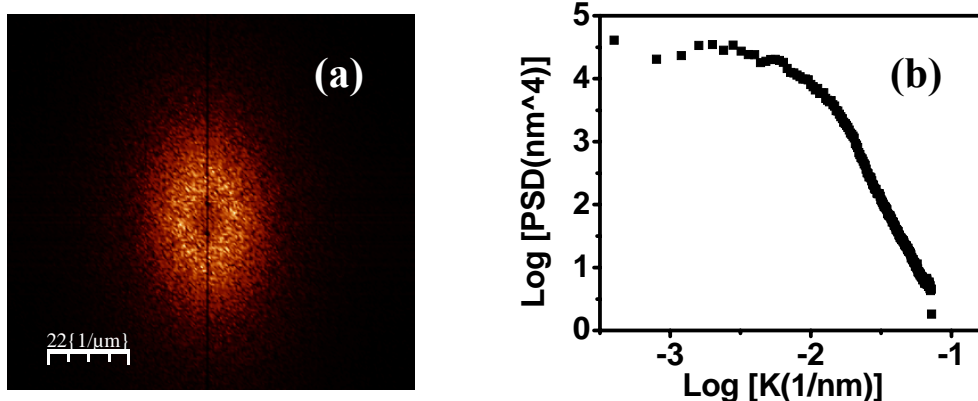

Figure A7 (a) An exemplary 2D-FFT of a scanned surface showing rotational isotropy, an indication of absence of shear fields. (b) A PSD master curve generated by angular averaging of the 2D-FFTs of images of two different scan sizes belonging to the same sample. It does not show a dominant in-plane correlational length scale.

The generation of such a master curve not only allowed us to investigate a wide dynamical range in reciprocal space but also validated that the AFM images describe the sample surface in a statistically significant manner.[179] If the master curve showed no prominent peak, it suggested the absence of a dominant in-plane correlational length scale.[180-181] Hence, it would be correct to assume the absence of inter-particle correlations

over a large spatial bandwidth. More importantly, this would mean that all subsequent results obtained for surface features arise only due to two reasons- loss of one degree of freedom as the molecule moves from 3D solution to 2D surface and of course, sample history. By comparing our results with (A)SAXS or SANS (as the case may be), it is essentially the extent of these two factors which we are measuring. Inter-particle correlations do not play a significant role and can be neglected.

A2.3.2.2 The 2D form factor curve

While radii of gyration (R_g) values are indicative of the average shape of the molecule, they fail to capture the exact structural correlations within it. In Chapter 6, we report on the progress made in realizing the usage of PSD curves at the single molecular level to provide us with a new characterization tool which is novel and sensitive to subtle changes in lateral distribution of molecular roughness. When properly interpreted, it makes available information inaccessible through R_g evaluation or through conventional profile measurements. In order to give statistical relevance to our work, we have evaluated the so called 2D form factor, an average of PSD curves generated for many isolated single molecules. The information retrieved through the 2D form factor conveys structural correlations within a single molecule after it adsorbs on the surface, just like SANS (the technique used in Chapter 6 for analysing solution conformation) does for the sample solution. A comparison of structural information of a single molecule revealed through these two methods gives us unique quantitative insight into the extent up to which a molecule changes its conformation as it moves from a 3D solution to a 2D surface and is inevitably affected by sample history.

Since a single molecule is almost never centro-symmetric, the risk in simply transferring the angular average protocol (described in section A2.3.2.1) to the single molecular level, is a smearing of correlation peaks. Central slice excision of the 2D-FFT can prevent this. However, central slice excision of the 2D-FFT was ruled out since such a procedure would miss a large number of "reflections" originating from the molecular morphology. Central slice excision of 2D-FFT has been followed by some authors[182] where the direction of anisotropy is known beforehand and correlations are required only along that direction. This was never our case. Hence, to observe the correlation peaks clearly, we followed a background subtraction procedure instead. This procedure worked remarkably well for our case. The background subtraction method used is similar to the one recently used in the PSD analysis of lateral packing arrangement of a single structural (capsid) protein inside a virus.[183]

Thus, PSD analysis was carried out on each completely isolated single molecule. The evaluation of a PSD curve for one molecule is shown in fig. A8a-b, respectively for a randomly extended and a collapsed molecule. A zoom-rectangular window having a single molecule was carved out of the AFM scan and was "flooded" to set all those pixel values to zero which represent a part of the mica substrate and not the molecule. "Flooding" is an inbuilt parameter of the WSxM software suite and has already been commented upon in section A2.3.1.1. Next, in order to perform 2D-FFT, and dictated by the algorithm of 2D-FFT, the zoom-rectangular window needed to be transformed so that the width and the height are an integer power of 2. This can be achieved in one of two ways, scale the image up to the nearest integer power of 2 or zero pad to the nearest integer power of 2. The second option was chosen here to maintain consistency with

"flooded" portion of the window. The PSD function was then measured for this "flooded" and zero padded window. Further, a background PSD function was evaluated. A simple way to define a background is to filter the image in such a way that all pixel heights above a certain threshold are excluded. This can be done using "equalize" filter of the WSxM software suite. The threshold can be chosen by extracting the baseline from lateral profile measurements. Once the background image has been generated, the background PSD function can be evaluated exactly in the same way as done for the original image. Finally, the background PSD function was subtracted from the total PSD function to give us a background-subtracted-PSD function of the molecule. A single molecular background-subtracted-PSD curve showed maxima suggesting structural correlations within the molecule. These maxima represent correlation lengths within the molecule and in no case, can be interpreted to be associated with the size parameters of the molecule like end to end distance (or major axis when ends are not decipherable) and width. This is because the correlation maxima for such parameters are present both in the PSD curve of the original image and the PSD curve of the background image. During subtraction, these peaks are removed.

Many single molecular background-subtracted-PSD curves belonging to different molecules of a sample were mathematically averaged to generate the 2D form factor curve for that sample. Note that only overlapping frequency ranges were included in the 2D form factor. Fluctuations at very low and very high frequencies were sliced off during averaging.
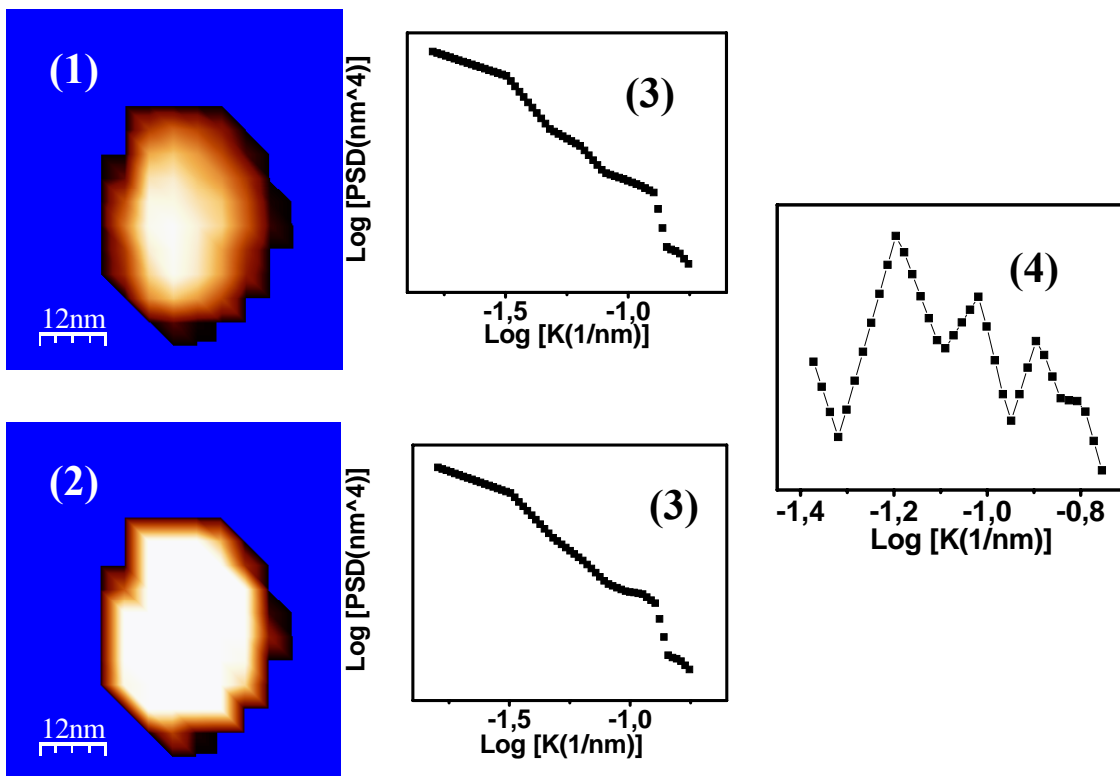
(a)
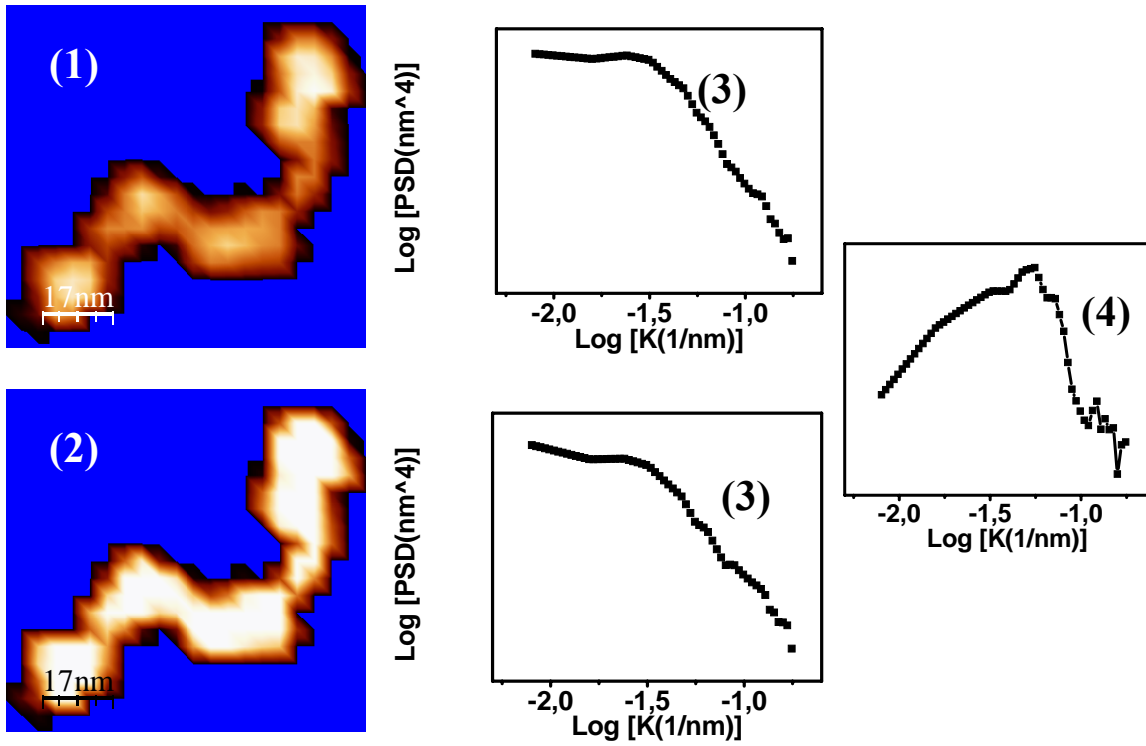
(b)

Figure A8: Image processing protocol for (a) a randomly extended molecule trapped on the surface (b) a collapsed molecule trapped on the surface. Step1- A single molecule is carved out of an AFM scan and subsequently, "flooded" and zero padded. Step2- The image is "equalized". Step3- Both the original and the "equalized" image are Fourier transformed and converted into PSD by an angular average. Step4- Background is removed by subtracting PSD of "equalized" image from PSD of original image.

The sudden fluctuation visible at very low frequencies is attributed to the application of "equalize" filter while generating the background image and has been reported by other authors[184-185] using similar filtering. Large deviations at very high frequencies occur due to aliasing effects caused by pixel resolution and small height differences between scan lines.[185] Any subtraction or averaging, whenever mentioned, was done after interpolation, using bicubic spline method, to first generate data sets with common abscissas.

It must be mentioned here that the image processing protocols used at the single molecular level, as detailed above, would remain unchanged even if global rotational isotropy is not found on the surface. The presence of global rotational isotropy is not a mandatory condition for evaluation of PSD curves at the single molecular level. In our case, its presence just helped us to neglect inter-particle correlations while interpreting our results.

Finally, an important precaution is to be followed regarding removal of artefacts. A spatial frequency bandpass filtering is often applied[185-185] in order to enhance contrast by "flattening" the image. The "flatten" filter of the WSxM software suite is a combination of two Gaussian filters- high pass, to remove long range topographic effects like bow and low pass, to suppress local noise. However, one should always check the signal on the original image first.[186]

Thus, PSD analysis for single molecules was done using carved out windows from the original scan on which no "flattening" filter was applied a priori. "Flattening" usually has only aesthetic importance anyway but in this case could have interfered with the anticipated peaks by cutting off the high and low frequencies even before the analysis had begun. In the rare case when the 2D-FFT of a carved out window containing a single molecule showed bow and/or noise, the artefacts were selectively removed on a case-by-case basis. Bow occurs due to drift of the piezoscanner along the Y axis (the slow scan axis) and shows up in the 2D-FFT as a bright line along the same axis. The entire line can be simply removed before the angular average is taken by using an appropriate cut filter. Noise, on the other hand, occurs due to acoustic vibrations during imaging and shows up in the 2D-FFT as two bright spots placed symmetrically opposite to each other. Noise too can be removed from the 2D-FFT by using a suitable cut filter before angular averaging.

A3 Static Light Scattering[187-188]

A very detailed survey of various scattering methods applied to polymer solutions is given in ref. 187 and 188. We shall describe SLS in relative detail and then briefly comment upon (A)SAXS and SANS (in the next sections) as the fundamentals remain the same.

SLS is a widely used characterization technique for polymer chains in solution. We can find the weight averaged molecular weight (M_w), the z-averaged radius of gyration (R_g) and the second virial coefficient (A_2). Fig A9a-c show the geometry of a typical SLS setup and the concepts of scattering vector and scattering volume respectively. Lets begin with fig. A9a. A cylindrical test tube containing a clear polymer solution is immersed in a glass vat filled with a fluid that has a refractive index close to that of glass. The fluid is

called an index-matching liquid and is thermostatted. A coherent, collimated beam of

laser enters the index-matching liquid through the vat and then into the test tube. Nearly

all of the incoming photons travel straight through the index-matching liquid and the

polymer solution forming a strong, unscattered (or forward scattered) beam. The polymer

molecules in the beam path scatter a tiny fraction of the photons in all directions. The

intensity of the scattered beam is detected by a photodetector, typically a photomultiplier,

placed horizontally at an angle θ (scattering angle) from the forward scattering direction.
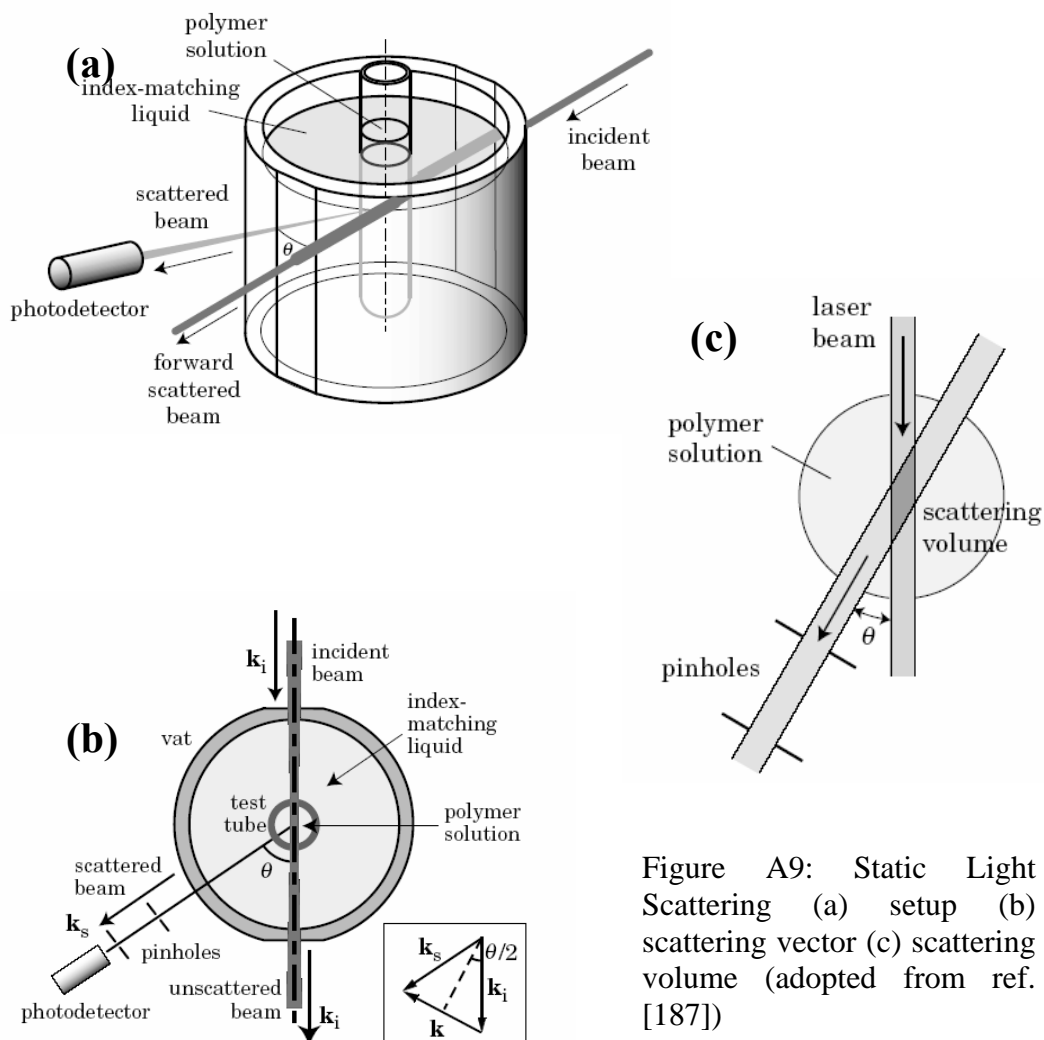
Figure A9: Static Light Scattering (a) setup (b) scattering vector (c) scattering volume (adopted from ref. [187])

Fig. A9b shows the concept of scattering vector. The incident beam has a wave vector K_i. The wave vector is parallel to the propagation direction of the beam and has a magnitude of $\dfrac{2\pi}{(\lambda/n)}$ where $\dfrac{\lambda}{n}$ is the wavelength of light in the solvent of refractive index n, with λ being the wavelength of light in vacuum. The wave vector K_s of the scattered beam has nearly the same magnitude as that of K_i so that $|K_i| = |K_s|$. The change in the wave vector upon scattering is called the scattering vector K and is defined as $K \equiv K_s - K_i$. The inset of fig. A9b allows the magnitude of $|K| = k$ to be conveniently calculated as

$$k = \frac{4\pi n}{\lambda}\sin\left(\frac{\theta}{2}\right) \tag{A4}$$

Fig. A9c shows the concept of scattering volume. Two pinholes or two vertical slits are placed along the path of the scattered beam to restrict the photons reaching the detector to those scattered by a small volume of the polymer solution called the scattering volume. The scattering volume is an intersection of the laser beam with the solid angle subtended by two pinholes.

Assume for a moment an isolated particle suspended in vacuum. An electromagnetic wave enters the isotropic particle to cause polarization in the direction of the electric field of the incident wave. The polarization is a displacement of the spatial average of the positively charged nuclei with respect to the negatively charged ions. The polarization, oscillating with the frequency of the radiation, serves as a broadcasting station that emits a weak radiation in all directions. The scattered radiation has the same frequency as that of the incident radiation. This mechanism of scattering is called Rayleigh scattering.
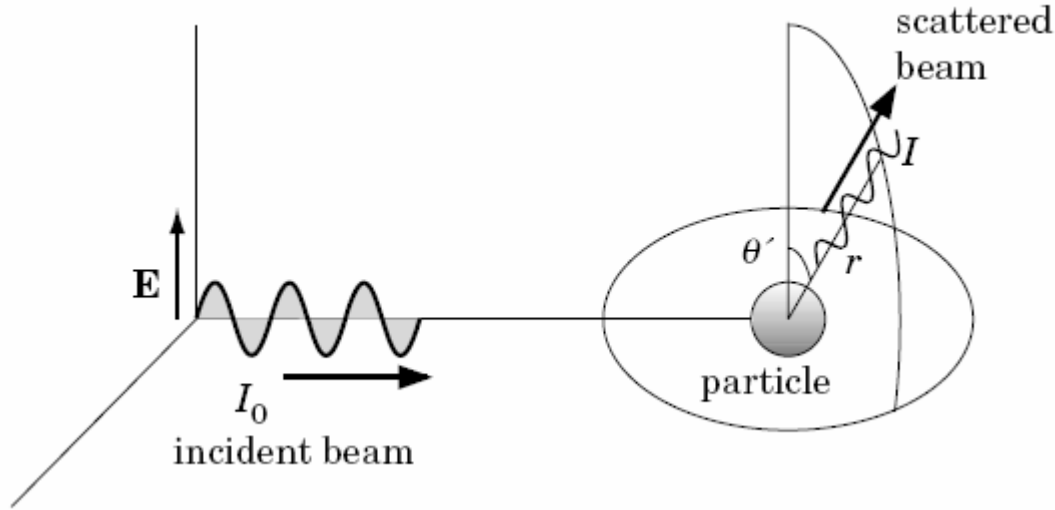
Figure A10: Vertically polarized beam causes polarization in the particle, which radiates into different directions. Angle θ' is defined as the angle between the electric field of the incident beam and the scattering direction. The particle size is drawn much larger than it is relative to the wavelength of light (adopted from ref. [187])

Fig. A10 shows the relationship between the vertically polarized incident beam of intensity I_0 and the radiation scattered by the vertically polarized particle. At a distance r from the particle and at an angle θ' from the vertical, the intensity I of the scattered light is given by eq. A5.

$$\frac{I}{I_0} = \frac{\pi^2}{\lambda^4} \frac{\alpha^2}{\varepsilon_0^2} \frac{\sin^2 \theta'}{r^2} \tag{A5}$$

where α is the polarizability of the particle and ε_0 is the permittivity of free space. Most measurement systems detect the light scattered horizontally and therefore, $\theta' = \frac{\pi}{2}$.

The scattering particle referred to in eq. A5 is assumed to be suspended in vacuum. In reality, it is inside a solvent, a continuous dielectric medium within the scattering volume. In a medium with refractive index n, the wavelength is $\frac{\lambda}{n}$ and the permittivity is $\varepsilon_0 n^2$.

The polarizability α is now written as α_{ex}, the excess polarizability of the suspended particle relative to the surrounding medium. Eq. A5 now changes to

$$\frac{I}{I_0} = \frac{\pi^2}{(\lambda/n)^4} \frac{\alpha_{ex}^2}{(\varepsilon_0 n^2)^2} \frac{\sin^2 \theta'}{r^2} = \frac{\pi^2}{\lambda^4} \frac{\alpha_{ex}^2}{\varepsilon_0^2} \frac{\sin^2 \theta'}{r^2} \tag{A6}$$

Eq. A6 refers to a particle inside a solvent. Scattering by a polymer molecule is larger because beams scattered by different parts of the molecule can interfere constructively. In fig. A11a, a beam path for the incoming light and a beam path for the scattered light are drawn for two monomers i and j at r_i and r_j on the chain. The difference in the path lengths is l_j-l_i. Fig. A11b shows the polarizations at monomers i and j as a function of time. The corresponding phase difference is $k_i l_j$ as per geometry shown.
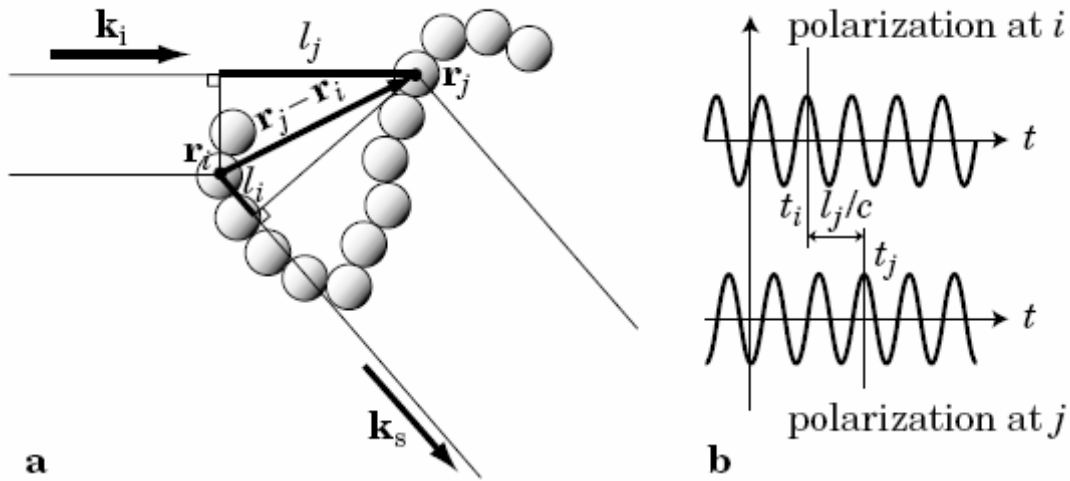

Figure A11: (a) beam path for incoming light and beam path for scattered light are drawn for two monomers i and j (b) polarizations of monomers i and j as a function of time (adopted from ref. [187])

If the monomers are isotropic particles with the same polarizability α_{ex} relative to the solvent, the total intensity I of horizontally scattered light (summing up the contributions from different monomers) can be shown to be (assuming $\theta' = \dfrac{\pi}{2}$ in eq. A6)

$$\frac{I}{I_0} = \frac{\pi^2}{\lambda^4} \frac{\alpha_{ex}^2}{\varepsilon_0^2} \frac{1}{r^2} \sum_{i,j=1}^{N} \exp\left[i\mathbf{K} \bullet \left(\mathbf{r}_i - \mathbf{r}_j\right)\right]$$ (A7)

where $\mathbf{K}$ is the scattering vector and N is the number of monomers in the polymer chain.

At low angles $\exp\left[i\mathbf{K} \bullet (\mathbf{r}_i - \mathbf{r}_j)\right] \approx 1$ and $\frac{I}{I_0}$ increases by a factor of N^2 compared with

single monomers. The constructive interference between photons scattered by different

parts of the polymer chain causes this N^2 dependence. It also shows why Small Angle

Scattering is often resorted to for better detection of scattered signals.

The quantity α_{ex} in eq. A7 is not fixed but constantly varies according to the changes in

permittivity of the scattering volume. The latter is caused because of density and

concentration fluctuations within the scattering volume. Since permittivity is related to

refractive index, we can define α_{ex} in terms of a more measurable quantity, the refractive

index. Any fluctuations in α_{ex} can also be put in terms of changes in refractive index. The

Clausius-Mossotti equation gives

$$d\alpha_{ex}\left(\mathbf{r}\right) = 2\varepsilon_0 n \Delta n\left(\mathbf{r}\right) dr$$ (A8)

where we have considered a small volume element dr at a distance r within the scattering

volume.

Eq. A7 accordingly can be shown to become

$$\frac{I}{I_0} = \frac{4\pi^2 n^2}{\lambda^4 r^2} \int d\mathbf{r}_1 \int d\mathbf{r}_2 \Delta n(\mathbf{r}_1)\Delta n(\mathbf{r}_2) \exp\left[i\mathbf{K} \bullet \left(\mathbf{r}_1 - \mathbf{r}_2\right)\right]$$ (A9)

where integration is over the scattering volume.

Scattering study of a polymer is usually carried out by first measuring the scattering

intensity I_{sol} of the pure solvent at different scattering angles θ and then repeating the

procedure on polymer solutions to obtain the scattering intensity I at different angles. The excess scattering is defined by $I_{ex} = I - I_{sol}$.

In eq. A9, $\Delta n(r)$ has two components: $\Delta n_d(r)$ and $\Delta n_c(r)$. The former is due to density fluctuations of the medium that appears also in I_{sol}. The latter is caused by concentration fluctuations of the polymer and is unique to the polymer solution. The excess scattering I_{ex} is due to $\Delta n_c(r)$. Eq. A9 then becomes

$$\frac{I_{ex}}{I_0} = \frac{4\pi^2 n^2}{\lambda^4 r^2} \int d\mathbf{r_1} \int d\mathbf{r_2} \langle \Delta n_c(\mathbf{r_1}) \Delta n_c(\mathbf{r_2}) \rangle \exp\left[i\mathbf{K} \bullet (\mathbf{r_1} - \mathbf{r_2}) \right] \tag{A10}$$

where again integration is over the scattering volume.

In real scattering experiments, the LHS of eq. A10 is represented in terms of Rayleigh ratio ΔR_θ. It is defined according to eq. A11.

$$\frac{I_{ex}}{I_0} = \frac{\Delta R_\theta V}{r^2} \tag{A11}$$

where V is the scattering volume and r is the detector-sample distance.

In an actual measurement system I_0 and V cannot be measured accurately. Therefore a pure solvent such as Benzene and Toluene is used as a calibration standard.

Eq. A10 now becomes

$$\frac{\Delta R_\theta V}{r^2} = \frac{4\pi^2 n^2}{\lambda^4 r^2} \int d\mathbf{r_1} \int d\mathbf{r_2} \langle \Delta n_c(\mathbf{r_1}) \Delta n_c(\mathbf{r_2}) \rangle \exp\left[i\mathbf{K} \bullet (\mathbf{r_1} - \mathbf{r_2}) \right] \tag{A12}$$

The quantity $\Delta n_c(r)$ in eq. A12 is related to the concentration fluctuation $\Delta c(r)$ by

$$\Delta n_c(\mathbf{r}) = \frac{dn}{dc} \Delta c(\mathbf{r}) \tag{A13}$$

where $\frac{dn}{dc}$ is called the differential refractive index or specific refractive index increment and is given roughly by

$$\frac{dn}{dc} \approx \left(n_{pol} - n_{sol}\right)\upsilon_{sp} \tag{A14}$$

In eq. A14 n_{pol} and n_{sol} are the refractive indices of the bulk polymer in amorphous state and of the solvent, respectively, and υ_{sp} is the specific volume of the polymer in the solution. A greater contrast between the refractive indices of polymer and solvent gives stronger scattering. When $\dfrac{dn}{dc}$ is near zero, the excess scattering is also almost zero resulting in the polymer being "invisible" to scattering (a condition called "index matching", i.e., the solvent is "isorefractive" with the polymer).

Eqs A12 and A13 can be rewritten as

$$\frac{\Delta R_\theta V}{r^2} = \frac{4\pi^2 n^2}{\lambda^4 r^2}\left(\frac{dn}{dc}\right)^2 \Psi_{cc}\left(\mathbf{K}\right) \tag{A15}$$

where $\Psi_{cc}(\mathbf{K})$ is the Fourier transform of the correlation function for the concentration fluctuations.

Using statistical mechanics, and for small scattering angles, low concentrations and monodispersed polymer solutions, we can show that eq. A15 reduces to

$$\frac{Hc}{\Delta R_\theta} = \frac{1}{M_w} + \frac{R_g^2 k^2}{3M_w} + A_2 c \tag{A16}$$

where H is called the contrast factor and is given by

$$H = \frac{4\pi^2}{\lambda^4 N_A}\left(n\frac{dn}{dc}\right)^2 \tag{A17}$$

In eqs. A16 and A17, A_2 is the second virial coefficient, N_A is the Avogadro's number, R_g is the z-averaged radius of gyration, M_w is the weight averaged molecular weight and other symbols have their usual meanings.

Zimm plot[189] is the most used method to extract M_w, R_g and A_2 from scattering data. The

excess scattering intensity is recorded at different scattering angles. The measurement is

repeated for several concentrations of the polymer at the same set of angles for a given

polymer solution. The intensity data are converted into $\dfrac{Hc}{\Delta R_\theta}$ and plotted as a function of

$\sin^2\left(\dfrac{\theta}{2}\right) + \text{constant} \times c$. The constant is arbitrary. The plot is called a Zimm plot. Open

circles in fig. A12 illustrate the ideal data. Each dashed line represents a series of

measurements at a constant angle. Each solid grey line is for those at constant

concentration. The data obtained at non zero angles and non zero concentrations is

extrapolated to $\theta = 0$ and $c = 0$, represented by two solid dark lines with a common

intercept. The intercept gives $\dfrac{1}{M_w}$. The slope of the $c = 0$ line is equal to $\dfrac{1}{3}\left(\dfrac{4\pi n}{\lambda}\right)^2 \dfrac{R_g^2}{M_w}$.

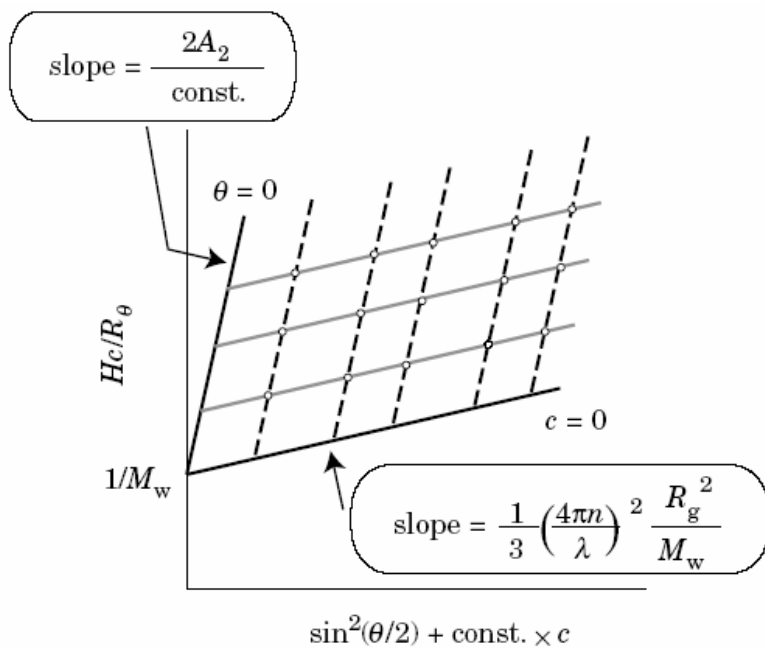The slope of the $\theta = 0$ line is $\dfrac{2A_2}{\text{constant}}$.

Figure A12: Schematic of the Zimm plot (adopted from ref. [187])

Note that if the concentration dependence, c of the polymer on the square of the magnitude of the scattering vector, k^2 is not linear (as was the case with some "reference samples" in this thesis), extrapolation to zero concentration is usually done according to Berry's approximation[190]

$$\sqrt{\frac{Hc}{\Delta R_{\theta=0}}} = \frac{1}{\sqrt{M_w}} + A_2 c\sqrt{M_w} \tag{A18}$$

Also note that when the sample contains a specifically binding ion, M^{2+}, extrapolation to zero concentration is not at all sensible. This is because any modification of concentration of polymer modifies the ratio $[M^{2+}]/[NaPA]$ (where we have used NaPA to indicate sodium polyacrylate, the polymer used in this thesis) leading to a completely different chemical specie. Hence, experiments now have to be analysed solely on the basis of extrapolation to zero scattering angle according to

$$\frac{Hc}{\Delta R_\theta} = \frac{1}{M_w} + \frac{R_g^2 k^2}{3M_w} + Bk^4 \tag{A19}$$

where k^4 term considers the bending of scattering curves.

A4 Small Angle X-ray Scattering and Anomalous SAXS[187-188]

The polarizability introduced in section A3 depends upon the volume of the particle. Thus larger particles are polarized more easily and scatter more detectable light than smaller particles for the same wavelength of incident radiation. In order to probe the smallest detail of the particles, we have to use incident radiation of very small wavelength as is evident by eq. A5. This is the basis of using X-rays as source radiations for probing the internal structure of single molecules.

The intensity of scattered X-ray is weak. Therefore, a synchrotron radiation source which provides a strong monochromatic beam is used. The magnitude of the scattering vector, now denoted by *q*, is given by

$$q = \frac{4\pi}{\lambda} \sin\left(\frac{\theta}{2}\right)$$

(A20)

where λ is the wavelength of the X-ray.

The range of scattering vector is typically 0.2 to 4 nm^{-1}. Thus, SAXS is able to study very precise details of molecules. Fig. A13 shows how a beamline at a synchrotron looks like.

Figure A13: The B1 beamline (now called JUSIFA) of the DORIS III synchrotron ring at HASYLAB, DESY, Hamburg, Germany (adopted from www.hasylab.desy.de/facilities/doris_iii/beamlines/b1 - Goerigk group)

X-rays are scattered by the electrons of atoms. Except for frequencies near to an electronic transition, the scattering occurs as if the electrons were ´free. Unlike SLS, where contrast variation comes from refractive index fluctuations, in SAXS, it comes from electron density fluctuations. The latter is defined as the difference between combined scattering lengths of polymer molecules and those of the solvent molecules per unit scattering volume. We can imagine scattering length to be the radius of a sphere which blocks the incident X-rays and scatters them in all directions. The scattering by a single electron (Thomson scattering) is described by a scattering length $b_0^x = 2.8 \times 10^{-15}$

m. The scattering length of jth atom or j^{th} molecule containing z electrons is given by

$b_j^x = zb_0^x$. The data handling is the same as in SLS.

Anomalous small-angle X-ray scattering (ASAXS) exploits the fact that close to an allowed electronic transition, an atom's scattering length varies with the frequency of radiation. Thus, for example, ASAXS is a suitable experimental technique which allows the structural characterization of the counterion distribution around the macroions by tuning the energy in the vicinity of the absorption edge of the ion in question. The distribution of the counterions is not accessible by conventional SAXS measurements, because the scattering contributions of the counterions and the macroions superimpose and cannot be distinguished.

A5 Small Angle Neutron Scattering[187-188]

Apart from SAXS, SANS may be used to probe structures of molecules and for very much the same basic advantage. Short de Broglie wavelengths of neutrons implies that small length scales can be probed.
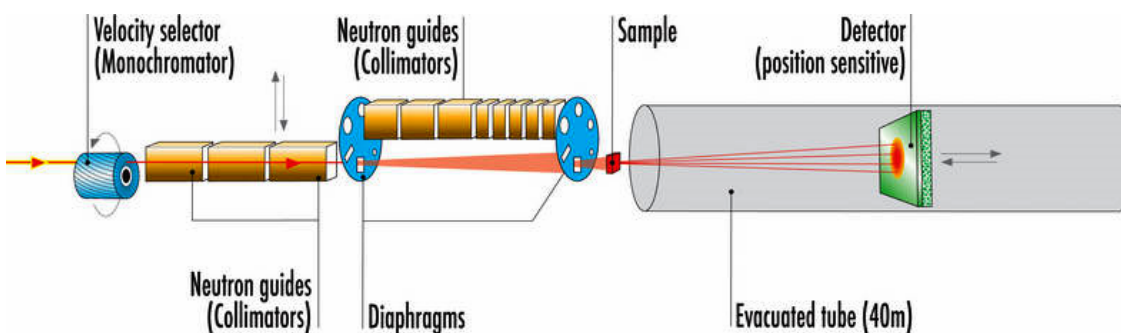

Figure A14: The layout of D11 SANS instrument used at Insitut Laue-Langevin (ILL) in Grenoble, France. (adopted from www.ill.eu/d11/ - Lindner, Schweins, Bowyer group)

Eq. A20 still gives the magnitude of the scattering vector, λ here being the de Broglie wavelength of neutrons.

The range of scattering vector is typically 0.02 to 3 nm^{-1}. Fig. A14 shows the layout of D11 SANS instrument used at Insitut Laue-Langevin (ILL) in Grenoble, France.

The nuclei of atoms or molecules are the scatterers in this case and the contrast comes from differences in scattering lengths, now abbreviated as b^N, per unit scattering volume. While the X-ray scattering lengths are proportional to the number of electrons in an atom or a molecule, the neutron scattering lengths vary irregularly with the type of nucleus. Furthermore, different isotopes of the same nucleus can have very different scattering lengths. For example, b^N for ^{1}H nucleus is -3.74 x 10^{-15} m while that for ^{2}H nucleus is +6.67 x 10^{-15} m. Thus, partial deuteration of the components of a sample leads to marked changes in its neutron scattering properties, frequently without seriously affecting its chemical and physical properties. It is possible by this means to 'highlight' different parts of a molecule and obtain very detailed structural information. The data handling is the same as in SLS.

MATLAB Codes

B1 MATLAB code for radii of gyration of adsorbed molecules

Fig. B1 shows the WSxM window where a single molecule is carved out of an AFM scan and subsequently "flooded". The "flooded" molecule is stored as an ASCII data file, in this case called 'm.txt'.
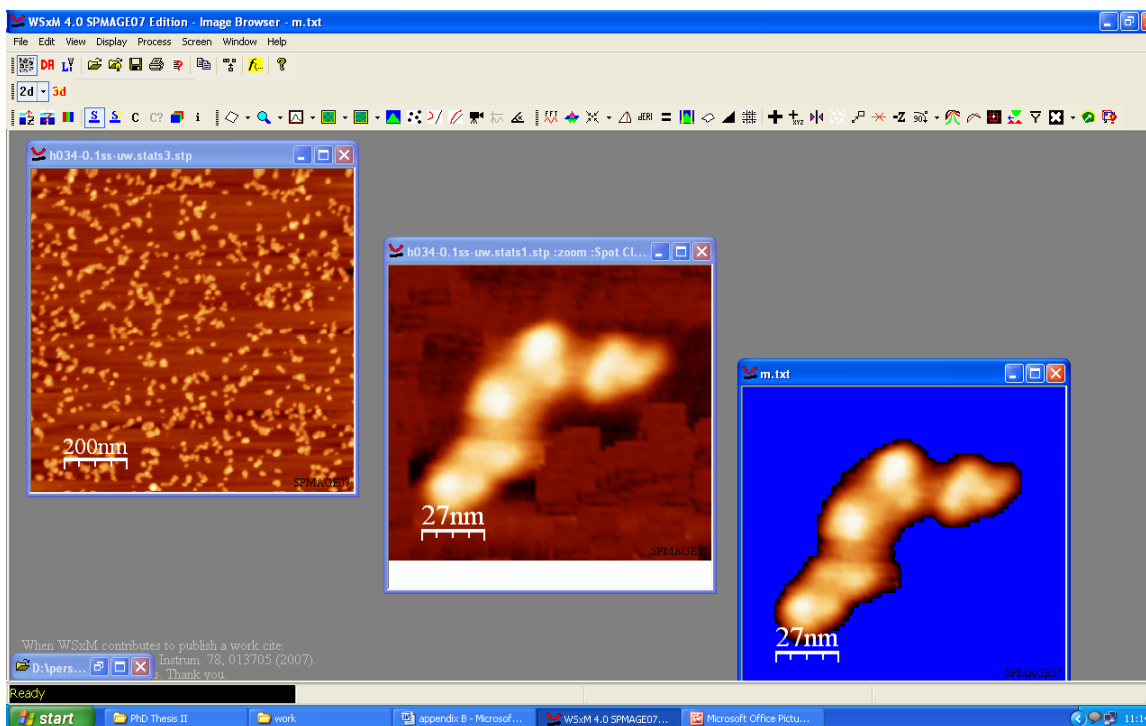

Figure B1: WSxM window- Creating the ASCII data file for a single molecule

The ASCII data file called 'm.txt' acts as an input file to a MATLAB code. The MATLAB editor window is shown in fig. B2. Note that lines 9,10 and 11 convert all x, y, z values to nm. The ASCII data file 'm.txt' generates x and y values in µm while z values in nm. For the particular molecule shown, our code gives $R_g{}^2$ value of 1006.9 nm² resulting in a R_g of 31.73 nm.

```
Editor - C:\MATLAB7\work\newprogram.m
File  Edit  Text  Cell  Tools  Debug  Desktop  Window  Help

 1 -    fid=fopen('m.txt');
 2 -    texxt = fgetl(fid);
 3 -    texxt = fgetl(fid);
 4 -    texxt = fgetl(fid);
 5 -    a=fscanf(fid,'%e');
 6 -    b=size(a);
 7 -    c=b(1)/3;
 8 -    for i=1:c
 9 -        xx(i)=a((i-1)*3 +1)*1000;
10 -        yy(i)=a((i-1)*3 +2)*1000;
11 -        zz(i)=a(3*i);
12 -    end
13 -    counter=1;
14 -    for i=1:c
15 -        if zz(i)>0
16 -            x(counter)=xx(i);
17 -            y(counter)=yy(i);
18 -            z(counter)=zz(i);
19 -            counter=counter+1;
20 -        end
21 -    end
22 -    sum_xz=0;
23 -    sum_x2z=0;
24 -    sum_yz=0;
25 -    sum_y2z=0;
26 -    sum_z=0;
27 -    for i=1:(counter-1)
28 -        sum_xz=sum_xz + x(i)*z(i);
29 -        sum_x2z=sum_x2z + x(i)*x(i)*z(i);
30 -        sum_yz=sum_yz + y(i)*z(i);
31 -        sum_y2z=sum_y2z + y(i)*y(i)*z(i);
32 -        sum_z=sum_z+z(i);
33 -    end
34 -    radius_sqrt=(sum_x2z + sum_y2z)/sum_z - (sum_xz/sum_z)^2 -(sum_yz/sum_z)^2
35 -    fclose(fid);
36
```

Figure B2: MATLAB editor window- The code converts 'm.txt' into $R_g{}^2$ value.

AFM Scans

C1 Necklace-like intermediate state for NaPA-Sr(II) on LaCl₃ treated mica

Some representative AFM scans of Sample D (0.1 g/L NaPA, 3.40 mM Sr^{2+}) and Sample

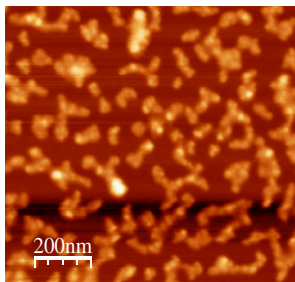E (0.1 g/L NaPA, 3.54 mM Sr^{2+}) referred in Chapter 4 are produced below.

Figure C1: Some representative AFM scans of Sample D (0.1 g/L NaPA, 3.40 mM Sr^{2+}) referred in Chapter 4.
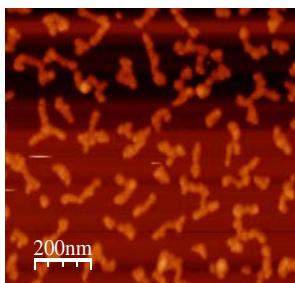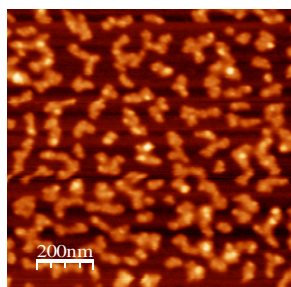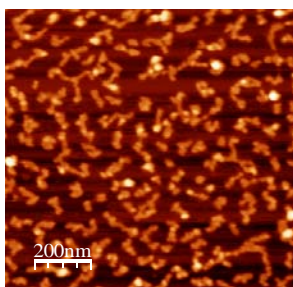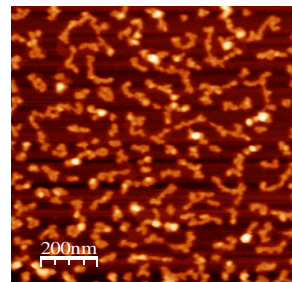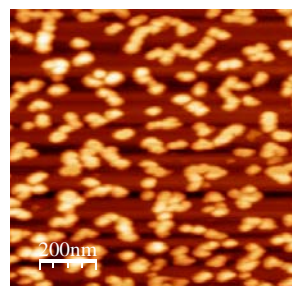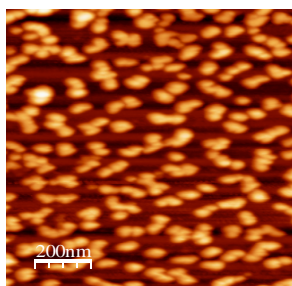

Figure C2: Some representative AFM scans of Sample E (0.1 g/L NaPA, 3.54 mM Sr^{2+}) referred in Chapter 4.
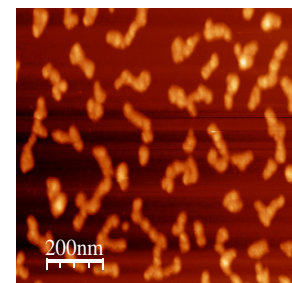
C2 Necklace-like intermediate state for NaPA-Pb(II) on chemically modified

(APDMES) mica

Some representative AFM scans of sample D (0.58 g/L NaPA, 1.65 mM Pb^{2+}) referred in
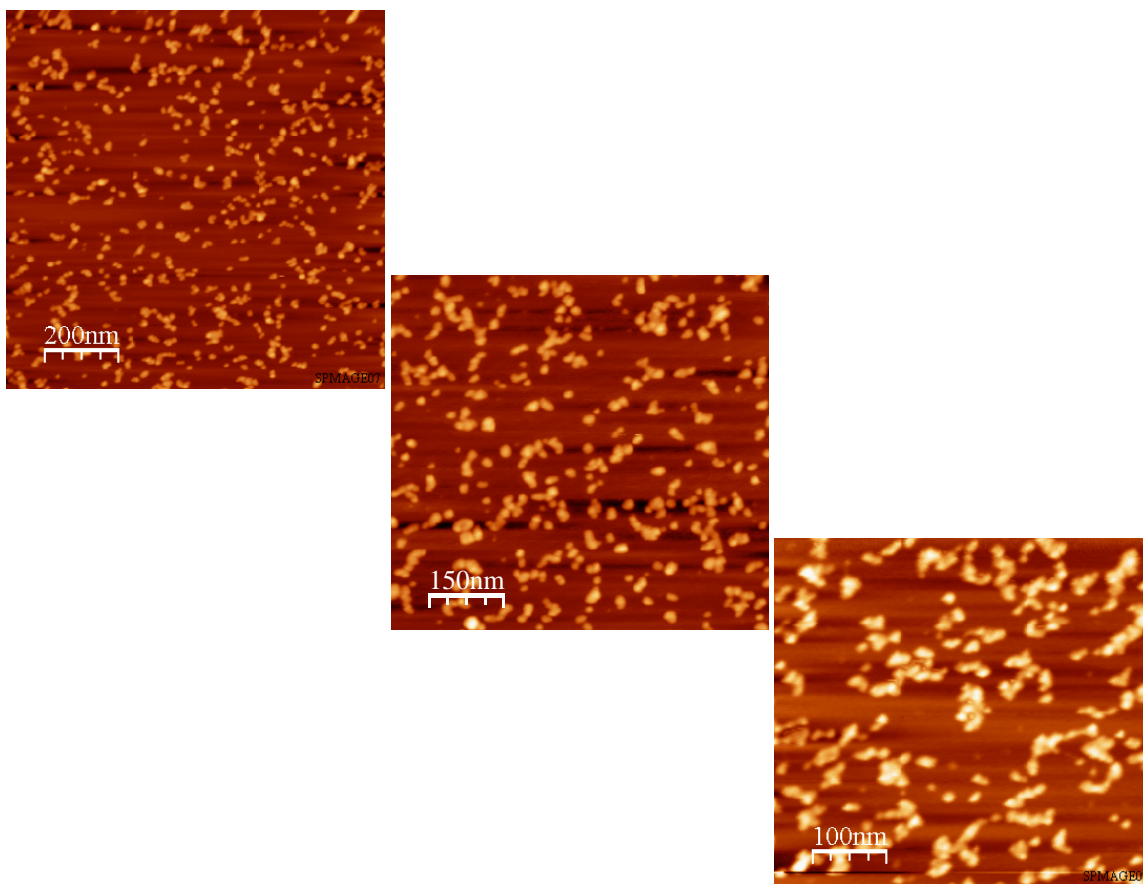
Chapter 5 are produced below.

Figure C3: Some representative AFM scans of Sample D (0.58 g/L NaPA, 1.65 mM Pb^{2+}) referred in Chapter 5.

C3 Naked NaPSSA on pristine mica and octylamine-chloroform treated mica

Naked NaPSSA molecules (salt free conditions) adsorbed on pristine mica surfaces at any concentration show a surprising tendency to form networks. The molecular contours are invariably broadened which makes us speculate that the molecules are not static but move during imaging. An exemplary AFM scan is shown in fig. C4. The best resolution is obtained when mica surfaces are treated with octylamine solution in chloroform. Individual chains of naked NaPSSA (salt free conditions) can now be resolved as exemplified in figs. C5 and C6. Note that the bulky polyelectrolyte backbone, as is the case here, proves much easy to image as compared to polyacrylates which have a fairly simple backbone.
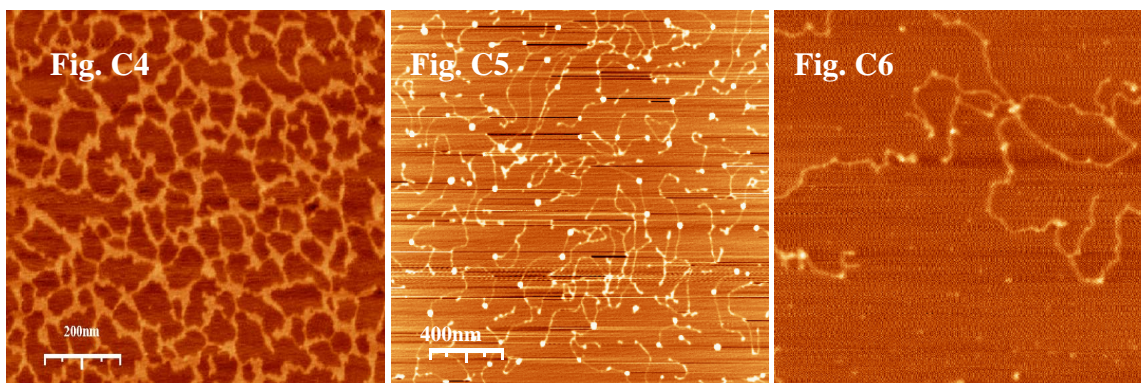
Figure C4-6: Naked NaPSSA chains on pristine mica (C4) and on mica treated with 10 g/L octylamine (sp. gr. 0.782)-chloroform solution (C5 and C6). The mol. wt. of NaPSSA used is 2.5 million Daltons. A concentration of 0.01 g/L was used. Adsorption time= 2-3 seconds.

C4 H-type precipitation behavior of NaPSSA with Ca^{2+} ions on pristine mica

Investigations of NaPSSA (0.01 g/L, mol. wt. 2.5 million Daltons) specifically bound by Ca^{2+} ions show anomalous behavior on pristine mica. AFM scans reveal that, unlike polyacrylates which possess a L-type precipitation threshold with Ca^{2+} ions(Chapter 6), polystyrene sulfonates only have a H-type precipitation threshold with the specifically

binding ion under consideration. No exotic intermediate state could be identified. However, before this H-type precipitation threshold, unidirectional cyclic stretching behavior is noticed under shear flow (section C5).
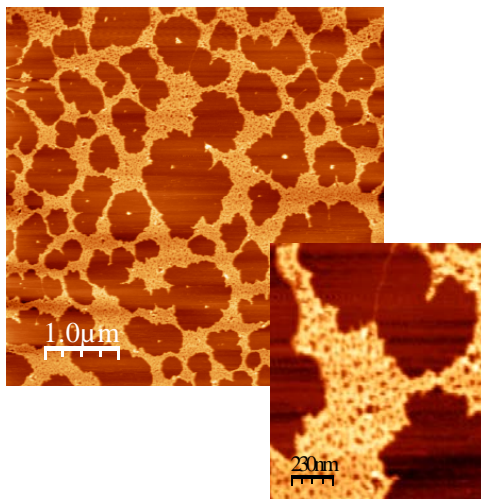
Figure C7: 0.01 g/L NaPSSA of mol. wt. 2.5 million Daltons in Millipore water was diluted from the stock solution concentration of 10 g/L using a buffer solution which was 5mM in $CaCl_2$. A drop was adsorbed on pristine mica for 2-3 seconds and blown off with N_2 flux. The chains have precipitated but no collapse can be seen.

C5 NaPSSA-Ca(II) on pristine mica – Effect of shear flow

Before the H-type precipitation threshold, NaPSSA molecules specifically bound by Ca^{2+} cations show unidirectional stretching under shear flow when adsorbed on pristine mica. This stretching behavior is speculated to be cyclic since coiled and extended conformations coexist.

Figure C8: Stretched and coiled states coexist when PSSA:Ca(II) charge ratio is 1:0.3. Mol wt. of NaPSSA was 2.5 million Daltons. Conc. was 0.01 g/L. Adsorption time was 2-3 seconds.

Bibliography

1. Kern, W. *Z. Phys. Chem. A,* **1938**, *181*, 249
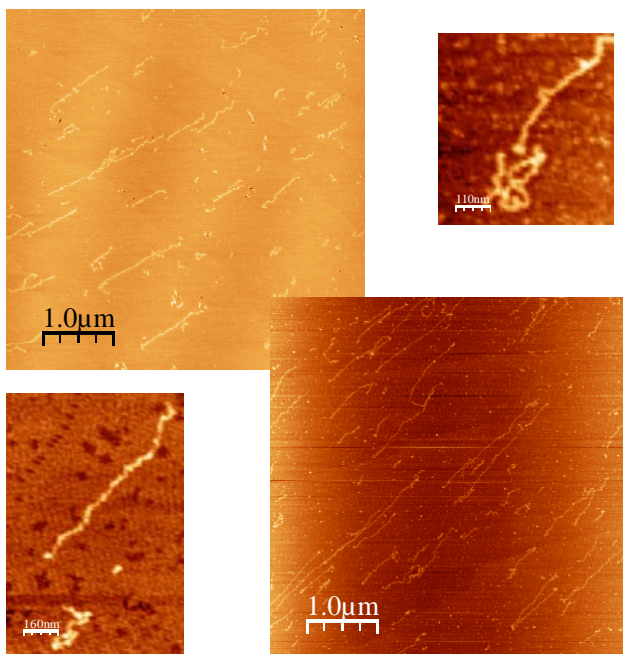
2. Kern, W. *Z. Phys. Chem. A,* **1938**, *181*, 283

3. Kern, W. *Z. Phys. Chem. A,* **1939**, *184*, 197

4. Kuhn, W.; Künzle, O.; Katchalsky, A. *Helv. Chim. Acta.*, **1948**, *31*, 1994

5. Katchalsky, A.; Künzle, O; Kuhn, W. *J. Polym. Sci.*, **1950**, *5*, 283

6. Alfrey, T.; Berg, P.W.; Morawetz, H. *J. Polym. Sci.*, **1951**, *7*, 543

7. Fuoss, R.M.; Katchalsky, A.; Lifson, S. *Proc. Natl. Acad. Sci. USA*, **1951**, *37*, 579

8. Gouy, G. *J. Phys. Radium* **1910**, *9*, 457

9. Chapman, D.L. *Phyl. Mag.* **1913**, *25*, 475

10. Imai, N.; Onishi, T. *J. Chem. Phys.,* **1959**, *30*, 1115

11 Onishi, T.; Imai, N.; Oosawa, F. *J. Phys. Soc. Japan*, **1960**, *15*, 896

12. Imai, N. *J. Phys. Soc. Japan*, **1961**, *16*, 746

13. MacGillivray, A.D.; Winkleman, J.J.Jr. *J. Chem. Phys.*, **1966**, *45*, 2184

14. Debye, P.; Hückel, E. *Physik Z.*, **1923**, *24*, 185

15. Kaplun, S.; Lagerstrom, P.A. *J. Math. Mech.*, **1957**, *6*, 585

16. Kaplun, S. *J. Math. Mech.*, **1957**, *6*, 595

17. Lagerstrom, P.A. *J. Math. Mech.*, **1957**, *6*, 605

18. Erdelyi, A. *Atti. Accad. Sci. Torino: Classe Sci. Fis. Mat. Nat.*, **1961**, *95*, 651

19. Erdelyi, A. *J. Soc. Ind. Appl. Math.*, **1963**, *11*, 105

20. Manning, G.S. *J. Chem. Phys.*, **1969**, *51*, 924

21. Jackson, J.L.; Coriell, S.R. *J. Chem. Phys.* **1964**, *40*, 1460

22. Gross, L.M.; Strauss, U.P. in *Chemical Physics of Ionic Solutions*, Conway, B.E.; Barradas, R.G., Eds.; John Wiley & Sons Inc., New York, **1966**, 347

23. Bjerrum, N. *Z. Electrochem.*, **1918**, *24*, 321

24. Odijk, T. *J. Polym. Sci.: Polym. Phys.*, **1977**, *15*, 477

25. Skolnick, J.; Fixman, M. *Macromolecules*, **1977**, *10*, 944

26. Barrat, J.L.; Joanny, J.F. *Europhys. Lett.*, **1993**, *24*, 333

27. de Gennes, P.G.; Pincus, P.; Velasco, R.M.; Brochard, F. *J. Phys. (Paris)*, **1976**, *37*, 1461

28. Khokhlov, A.R.; Khachaturian, K.A. *Polymer*, **1982**, *23*, 1742

29. Borue, V. Yu.; Erukhimovich, I. Ya. *Macromolecules*, **1988**, *21*, 3240

30. Joanny, J.F.; Leibler, L. *J. Phys. (Paris)*, **1990**, *51*, 545

31. Dobrynin, A.V.; Colby, R.H.; Rubinstein, M. *Macromolecules*, **1995**, *28*, 1859

32. Khokhlov, A.R. *J. Phys. A*, **1980**, *13*, 979

33. Pfeuty, P. *J. Phys. Collog.*, **1978**, *39*, C2-149

34. Muller, G.; Fenyo, J.C.; Braud, C.; Selegny, E. in *Polyelectrolytes and their Applications*, Rembaum, A.; Selegny, E., Eds.; Reidel, New York, **1975**, "Compact conformation of polyions stabilized by non-electrostatic short range interactions"

35. Dubin, P.L.; Strauss, U.P. in *Polyelectrolytes and their Applications*, Rembaum, A.; Selegny, E., Eds.; Reidel, New York, **1975**, "Hypercoiling in hydrophobic polyacids"

36. Berghold, G.; van der Schoot, P.; Seidel, C. *J. Chem. Phys.*, **1997**, *107*, 8083

37. Castelnovo, M.; Sens, P.; Joanny, J.F. *Eur. Phys. J. E*, **2000**, *1*, 115.

38. Zito, T.; Seidel, C. *Eur. Phys. J. E*, **2002**, *8*, 339

39. Borochov, N.; Eisenberg, H. *Macromolecules*, **1994**, *27*, 1440

40. Förster, S.; Schmidt, M.; Antonietti, M. *J. Phys. Chem.*, **1992**, *96*, 4008

41. Eisenberg, H.; Mohan, G.R. *J. Phys. Chem.*, **1959**, *63*, 671

42. Chu, P.; Marinsky, J.A. *J. Phys. Chem.*, **1967**, *71*, 4352

43. Quadrifoglio, F.; Crescenzi, V.; Delben, F. *Macromolecules*, **1973**, *6*, 301

44. Katchalsky, A.; Eisenberg, H. *J. Polym. Sci.*, **1951**, *6*, 145

45. Crescenzi, V.; Quadrifoglio, F. *J. Polym. Sci. A-2: Polym. Phys.*, **1972**, *10*, 367

46. Klooster, N.T.M.; van der Touw, F.; Mandel, M. *Macromolecules*, **1984**, *17*, 2070

47. Morawetz, H.; Wang, Y. *Macromolecules*, **1987**, *20*, 194

48. Rayleigh, L. *Philos. Mag.*, **1882**, *14*, 184

49. de Gennes, P.G. in *Scaling Concepts in Polymer Physics*, Cornell University Press: Ithaca, New York, **1985**

50. Hooper, H.H.; Beltran, S.; Sassi, A.P.; Blanch, H.W.; Prausnitz, J.M. *J. Chem. Phys.*, **1990**, *93*, 2715

51. Higgs, P.G.; Orland, H. *J. Chem. Phys.*, **1991**, *95*, 4506

52. Raphael, E.; Joanny, J.F. *Europhys. Lett.*, **1990**, *13*, 623

53. Higgs, P.G.; Raphael, E. *J. Phys. I*, **1991**, *1*, 1

54. Kantor, Y.; Kardar, M. *Europhys. Lett.*, **1994**, *27*, 643

55. Kantor, Y.; Kardar, M. *Phys. Rev. E*, **1995**, *51*, 1299

56. Dobrynin, A.V.; Rubinstein, M.; Obukhov, S.P. *Macromolecules*, **1996**, *29*, 2974

57. Solis, F.J.; Cruz, M. Olvera de la *Macromolecules*, **1998**, *31*, 5502

58. Migliorini, G.; Lee, N.; Rostiashvili, V.; Vilgis, T.A. *Eur. Phys. J. E*, **2001**, *6*, 259

59. Pickett, G.T.; Balazs, A.C. *Langmuir*, **2001**, *17*, 5111

60. Uyaver, S.; Seidel, C. *Europhys. Lett.*, **2003**, *64*, 536

61. Uyaver, S.; Seidel, C. *J. Phys. Chem. B*, **2004**, *108*, 18804

62. Lyulin, A.V.; Dünweg, B.; Borisov, O.V.; Darinskii, A.A. *Macromolecules*, **1999**, *32*, 3264

63. Chodanowski, P.; Stoll, S. *J. Chem. Phys.*, **1999**, *111*, 6069

64. Ulrich, S.; Laguecir, A.; Stoll, S. *J. Chem. Phys.*, **2005**, *122*, 094911-1

65. Dobrynin, A.V.; Rubinstein, M. *Macromolecules*, **1999**, *32*, 915

66. Dobrynin, A.V.; Rubinstein, M. *Macromolecules*, **2001**, *34*, 1964

67. Konieczny, M.; Likos, C.N.; Löwen, H. *J. Chem. Phys.*, **2004**, *121*, 4913

68. Deshkovski, A.; Obukhov, S.; Rubinstein, M. *Phys. Rev. Lett.*, **2001**, *86*, 2341

69. Liao, Q.; Dobrynin, A.V.; Rubinstein, M. *Macromolecules*, **2003**, *36*, 3386

70. Liao, Q.; Dobrynin, A.V.; Rubinstein, M. *Macromolecules*, **2003**, *36*, 3399

71. Micka, U.; Holm, C.; Kremer, K. *Langmuir*, **1999**, *15*, 4033

72. Micka, U.; Kremer, K. *Europhys. Lett.*, **2000**, *49*, 189

73. Limbach, H.J.; Holm, C.; Kremer, K. *Europhys. Lett.*, **2002**, *60*, 566

74. Limbach, H.J.; Holm, C. *Comput. Phys. Commun.*, **2002**, *147*, 321

75. Limbach, H.J.; Holm, C. *J. Phys. Chem. B*, **2003**, *107*, 8041

76. Limbach, H.J.; Holm, C.; Kremer, K. *Macromol. Symp.*, **2004**, *211*, 43

77. Schiessel, H.; Pincus, P. *Macromolecules*, **1998**, *31*, 7953

78. Schiessel, H. *Macromolecules*, **1999**, *32*, 5673

79. Liao, Q.; Dobrynin, A.V.; Rubinstein, M. *Macromolecules*, **2006**, *39*, 1920

80. Flory, P.J.; Osterheld, J.E. *J. Phys. Chem.*, **1954**, *58*, 653

81. Eisenberg, H.; Woodside, D. *J. Chem. Phys.*, **1962**, *36*, 1844

82. Takahashi, A.; Kato, T.; Nagasawa, M. *J. Phys. Chem.*, **1967**, *71*, 2001

83. Takahashi, A.; Yamori, S.; Kagawa, I. *Kogyo Kagaku Zasshi*, **1962**, *83*, 11

84. Takahashi, A.; Nagasawa, M. *J. Am. Chem. Soc.*, **1964**, *86*, 543

85. Eisenberg, H.; Mohan, G.R. *J. Phys. Chem.*, **1959**, *63*, 671

86. Eisenberg, H.; Casassa, E.F. *J. Polym. Sci.*, **1960**, *47*, 29

87. Igekami, A.; Imai, N. *J. Polym. Sci.*, **1962**, *56*, 133

88. Wall, F.T.; Drennan, J.W. *J. Polym. Sci.*, **1951**, *7*, 83

89. Michaeli, I. *J. Polym. Sci.*, **1960**, *48*, 291

90. Huber, K. *J. Phys. Chem.*, **1993**, *97*, 9825

91. Pochard, I.; Foissy, A.; Couchot, P. *Colloid Polym. Sci.*, **1999**, *277*, 818

92. Francois, J.; Truong, N.D.; Medjahdi, G.; Mestdagh, M.M. *Polymer*, **1997**, *38*, 6115

93. Sabbagh, I.; Delsanti, M.; Lesieur, P. *Eur. Phys. J. B*, **1999**, *12*, 253

94. Heitz, C.; Francois, J. *Polymer*, **1999**, *40*, 3331

95. Dubois, E.; Boue, F. *Macromolecules*, **2001**, *34*, 3684

96. Peng, S.; Wu, C. *Macromolecules*, **1999**, *32*, 585

97. Schweins, R.; Huber, K. *Eur. Phys. J. E*, **2001**, *5*, 117

98. Schweins, R.; Hollmann, J.; Huber, K. *Polymer*, **2003**, *44*, 7131

99. Schweins, R.; Lindner, P.; Huber, K. *Macromolecules*, **2003**, *36*, 9564

100. Goerigk, G.; Schweins, R.; Huber, K.; Ballauf, M. *Europhys. Lett.*, **2004**, *66*, 331

101. Schweins, R.; Goerigk, G.; Huber, K. *Eur. Phys. J. E*, **2006**, *21*, 99

102. Goerigk, G.; Huber, K.; Schweins, R. *J. Chem. Phys.*, **2007**, *127*, 154908-1

103. Lages, S.; Schweins, R.; Huber, K. *J. Phys. Chem. B*, **2007**, *111*, 10431

104. Narh, K.A.; Keller, A. *J. Polym. Sci. B: Polym. Phys.*, **1993**, *31*, 231

105. Cruz, M. Olvera de la; Belloni, L.; Delsanti, M.; Dalbiez, J.P.; Spalla, O.; Drifford, M. *J. Chem. Phys.*, **1995**, *103*, 5781

106. Wittmer, J.; Johner, A.; Joanny, J.F. *J. Phys. II France*, **1995**, *5*, 635

107. Lang, D.; Coates, P. *J. Mol. Biol.*, **1968**, *36*, 137

108. Dubas, S.T.; Schlenoff, J.B. *Macromolecules*, **1999**, *32*, 8153

109. Poptoshev, E.; Schoeler, B.; Caruso, F. *Langmuir*, **2004**, *20*, 829

110. Kotov, N. *Nanostruct. Mater.*, **1999**, *12*, 789

111. Andelman, D.; Joanny, J.F. *J. Phys. IV France*, **2000**, *1*, 1153

112. Borisov, O.; Zhulina, E.; Birhstein, T. *J. Phys. (France) II*, **1994**, *4*, 913

113. Wiegel, F. *J. Phys. A*, **1977**, *10*, 299

114. Netz, R.; Joanny, J.F. *Macromolecules*, **1999**, *32*, 9013

115. Dobrynin, A.V.; Rubinstein, M. *Prog. Polym. Sci.*, **2005**, *30*, 1049

116. Kiriy, A.; Gorodyska, G.; Minko, S.; Jaeger, W.; Stepanek, P.; Stamm, M. *J. Am. Chem. Soc.*, **2002**, *124*, 13454

117. Roiter, Y.; Jaeger, W.; Minko, S. *Polymer*, **2006**, *47*, 2493

118. Rivetti, C.; Guthold, M.; Bustamante, C. *J. Mol. Biol.*, **1996**, *264*, 919

119. Kirwan, L. J.; Papastavrou, G.; Borkovec, M.; Behrens, S. H. *Nano Letters* **2004**, *4*, 149

120. Hansma, H.G.; Bezanilla, M.; Zenhausern, F.; Adrian, M.; Sinsheimer, R.L. *Nucleic Acids Res.*, **1993**, *21*, 505

121. Lindsay, S.M.; Tao, N.J.; DeRose, J.A.; Oden, P.I.; Lyubchenko, Y.L.; Harrington, R.E.; Shlyakhtenko, L. *Biophys. J.*, **1992**, *61*, 1570

122. Lyubchenko, Y.L.; Jacobs, B.L.; Lindsay, S.M. *Nucleic Acids Res.*, **1992**, *20*, 3983

123. Guthold, M.; Bezanilla, M.; Erie, D.A.; Jenkins, B.; Hansma, H.G.; Bustamante, C. *Proc. Natl. Acad. Sci. U.S.A.*, **1994**, *91*, 12927

124. Bustamante, C.; Vesenka, J.; Tang, C.L.; Rees, W.; Guthold, M.; Keller, R. *Biochemistry*, **1992**, *31*, 22

125. Hansma, H.G.; Vesenka, J.; Siegerist, C.; Kelderman, G.; Morrett, H.; Sinsheimer, R.L.; Elings, V.; Bustamante, C.; Hansma, P.K. *Science*, **1992**, *256*, 1180

126. Vesenka, J.; Guthold, M.; Tang, C.L.; Keller, D.; Delaine, E.; Bustamante, C. *Ultramicroscopy*, **1992**, *42/44*, 1243

127. Berg, J.M.; Claesson, P.M.; Neuman, R.D. *J. Colloid Interface Sci.*, **1993**, *161*, 182

128. Malmsten, M.; Claesson, P.M.; Siegel, G. *Langmuir*, **1994**, *10*, 1274

129. Abraham, T.; Kumpulainen, A.; Xu, Z.; Rutland, M.; Claesson, P.M.; Masliyah, J. *Langmuir*, **2001**, *17*, 8321

130. You, H.X.; Lowe, C.R. *J. Colloid Interface Sci.*, **1996**, *182*, 586

131. Bezanilla, M.; Manne, S.; Laney, D.E.; Lyubchenko, Y.L.; Hansma, H.G. *Langmuir*, **1995**, *11*, 655

132. Lyubchenko, Y.L.; Oden, P.I.; Lampner, D.; Lindsay, S.M.; Dunker, K.A. *Nucleic Acids Res.*, **1993**, *21*, 1117

133. Reddy, G.; Chang, R.; Yethiraj, A. *J. Chem. Theory Comput.*, **2006**, *2(3)*, 630

134. Kong, C.; Muthukumar, M. *J. Chem. Phys.*, **1998**, *109*, 1522

135. Panwar, A.; Kumar, S. *J. Chem. Phys.*, **2005**, *122*, 154902

136. Beltran, S.; Hooper, H.; Blanch, H.; Prausnitz, J. *Macromolecules*, **1991**, *24*, 3178

137. Sinn, C.G.; Dimova, R.; Antonietti, M. *Macromolecules*, **2004**, *37*, 3444

138. Molnar, F.; Reiger, J. *Langmuir*, **2005**, *21*, 786

139. Watanabe, M.; Baba, S.; Nakata, T.; Morimoto, T.; Sekino, S. in *Metrology, Inspection and Process Control for Microlithography XXII*; Allgair, J.A., Raymond, C.J., Eds.; Proc. SPIE vol. 6922: San Jose, CA, USA, **2008**, 69220J-1-14

140. Guldberg-Pedersen, H.; Bergström, L. *Acta Mater*, **2000**, *48*, 4570

141. Guldberg-Pedersen, H.; Bergström, L. *J Am Ceram Soc*, **1999**, *82*, 1137

142. Laarz, E.; Meurk, A.; Yanez, J.A.; Bergström,L. *J Am Ceram Soc*, **2001**, *84*, 1675

143. Schweins, R.; Huber, K. *Macromol. Symp.* **2004**, *211*, 25

144. Dautzenberg, H.; Jaeger, W.; Kötz, B. P. J.; Seidel, C.; Stscherbina D. in *Polyelectroytes: Formation, characterization and application*, Hanser Publishers: Munich, Vienna, New York, **1994**.

145. Different authors in *Polyelectrolytes*, Hara, M., Ed.; Marcel Dekker: New York, **1993**.

146. Xu, Y.; Cymerman, G. in *Polymers in Mineral Processing*, Laskowski, J. S., Ed.; MET SOC: British Columbia, **2000**, 591.

147. Hesselink, T. T. *J. Colloid Interface Sci.*, **1977**, *60*, 448.

148. Fleer, G. J.; Lyklema, J. *J. Colloid Interface Sci.*, **1974**, *167*, 228.

149. Matsumoto, T.; Adachi, Y. *J. Colloid Interface Sci.*, **1998**, *204*, 328.

150. Horn, D., Linkart, F. in *Paper Chemistry*, Roberts, Ed.; Blackie Academic & Professional: Glasgow, **1996**, 64

151. Wagberg, L.; Kolar, K. *Ber. Bunsen-Ges. Phys. Chem.*, **1996**, *100*, 984.

152. Hunter, R. J. in *Foundations of Colloid Science*, Oxford University Press: Oxford, **1991**.

153. Dahlgren, M. A. G.; Claesson, P. M. *Prog. Colloid Polym. Sci.*, **1993**, *93*, 206.

154. Dahlgren, M. A. G.; Claesson, P. M.; Audebert, R. *J. Colloid Interface Sci.*, **1994**, *166*, 343.

155. Klein, J.; Luckham, P. F. *Colloids Surf.*, **1984**, *10*, 65.

156. Decher, G.; Hong, J. D. *Macromol. Chem. Macromol. Symp.*, **1991**, *46*, 321.

157. Decher, G. *Science*, **1997**, *277*, 1232 and references therein.

158. Donath, E.; Sukhorukov, G.; Caruso, F.; Davis, S.; Möhwald, H. *Angew. Chem., Int. Ed.*, **1998**, *37*, 2201.

159. Lindholm-Sethson, B. *Langmuir*, **1996**, *12*, 3305.

160. Wong, J. Y.; Majewski, J.; Seitz, M.; Park, C. K.; Israelachvili, Bustamante, C. *Science*, **1997**, *276*, 1112.

161. Tanaka, T. *Phys Rev. Lett.*, **1978**, *40*, 820

162. Osada, Y.; Gong, J. *Prog. Polym. Sci.*, **1993**, *18*, 187.

163. Dickson, R.M.; Cubitt, A.B.; Tsien, R.Y.; Moerner, W.E. *Nature*, **1997**, *388*, 355

164. Michler, P.; Kiraz, A.; Becher, C.; Schoenfeld, W.V.; Petroff, P.M.; Zhang, L.; Hu, E.; Imamoglu, A. *Science*, **2000**, *290*, 2282

165. Huang, Y.; Duan, X.; Cui, Y.; Lauhon, L.J.; Kim, K.H.; Lieber, C.M. *Science*, **2001**, *294*, 1313

166. Whitesides, G.M. *Nature*, **2006**, *442*, 368

167. Virji, S.; Huang, J.; Kaner, R.B.; Weiller, B.H. *Nano Lett.* **2004**, *4*, 491

168. Yang, H.H.; Zhang, S.Q.; Tan, F.; Zhuang, Z.X.; Wang, X.R. *J. Am. Chem. Soc.*, **2005**, *127*, 1378

169. Ramanathan, K.; Bangar, M.A.; Yun. M.; Chen, W.; Myung, N.V.; Mulchandani, A. *J. Am. Chem. Soc.*, **2005**, *127*, 496

170. Huber, K.; Witte, T.; Hollmann, J.; Keuker-Baumann, S.; *J.Am.Chem.Soc.* **2007**, *129*, 1089

171. Digital Instruments Veeco Metrology Group, Scanning Probe Microscopes, Training Notebook, Santa Barbara, CA, **1999**

172. I. Horcas et al., Rev. Sci. Instrum. 78, 013705, **2007**

173. Gorodyska, G.; Kiriy, A.; Minko, S.; Tsitsilianis, C.; Stamm, M. *NanoLett.* **2003**, *3(3)*, 365

174. Kiriy, A.; Gorodyska, G.; Minko, S.; Tsitsilianis, C.; Stamm, M. *Macromolecules* **2003**, *36*, 8704

175. Digital Instruments Veeco Metrology Group, MultiMode SPM Instruction Manual, Version 4.31ce, **1997**

176. Minko, S.; Kiriy, A.; Gorodyska, G.; Stamm, M. *J. Am. Chem. Soc.* **2002**, *124*, 3218

177. Kumaki, J.; Hashimoto, T. *J. Am. Chem. Soc.* **2003**, *125*, 4907

178. Fang, S.J.; Haplepete, S.; Chen, W.; Helms, C.R.; Edwards, H. *J. Appl. Phys.*, **1997**, *82*, 5891

179. Dumas, Ph.; Bouffakhreddine, B.; Amra, C.; Vatel, O.; Andre, E.; Galindo, R.; Salvan, F. *Europhys. Lett.*, **1993**, *22*, 717

180. Gutmann, J.S.; Müller-Buschbaum, P.; Stamm, M. *Faraday Discuss.*, **1999**, *112*, 285

181. Müller-Buschbaum, P.; Bauer, E.; Wunnicke, O.; Stamm, M. *J. Phys: Condens. Matter*, **2005**, *17*, S363

182. Carbone, D.; Alija, A.; Plantevin, O.; Gago, R.; Facsko, S.; Metzger, T.H. *Nanotechnology*, **2008**, *19*, 035304

183. Briggs, J.A.G.; Johnson, M.C.; Simon, M.N.; Fuller, S.D.; Vogt, V.M. *J. Mol. Biol.*, **2006**, *355*, 157

184. Ruppe, C.; Duparre, A. *Thin Solid Films*, **1996**, *288*, 8

185. Jiang, T.; Hall, N.; Ho, A.; Morin, S. *Thin Solid Films*, **2005**, *471*, 76

186. Haubruge, H.G.; Gallez, X.A.; Nysten, B.; Jonas, A.M. *J. Appl. Cryst.*, **2003**, *36*, 1019

187. Teraoka, I. in *Polymer Solutions: An introduction to Physical Properties*, John Wiley & Sons Inc., New York, **2002**

188. Different authors in *Neutrons, X-rays and Light: Scattering methods applied to soft condensed matter,* Lindner P.; Zemb, Th., Eds.; Elsevier Amsterdam, **2002**

189. Zimm, B.H. *J. Chem. Phys.*, **1948**, *16*, 1093

190. Berry, G.C. *J. Chem. Phys.*, **1966**, *44*, 4550

Curriculum Vitae

Prashant Sinha
(born on 14th September, 1978 in Lucknow, India)

2006-2009:	PhD student at the Leibniz-Institut für Polymerforschung Dresden e.V., Dresden, Germany. (Supervisor- Prof. Dr. Manfred Stamm)
2005-2006:	Research associate in the area of porphyrinogen chemistry at the Indian Institute of Technology, Kanpur, India. (Supervisor- Prof. Dr. S. Sarkar)
1998-2003:	Master of Science (5 year integrated programme) in Chemistry at the Indian Institute of Technology, Kanpur, India. (Masters Thesis Supervisor- Prof. Dr. P. Guptabhaya)
1997:	Indian School Certificate (Grade XII) from St. Francis'College, Lucknow, India.
1995:	Indian Certificate for Secondary Education (Grade X) from St. Paul's School, Lucknow, India.

Publications

1) Lages, S.; Lindner, P.; **Sinha, P.**; Kiriy, A.; Stamm, M.; Huber, K. 'Formation of Ca^{2+} induced intermediate necklace structures of polyacrylate chains', 2009, *Macromolecules*, 42, 4288-4299

2) **Sinha, P.**; Lages, S.; Kiriy, A.; Huber, K.; Stamm, M. 'Adsorption behaviour of partially collapsed polyacrylate coils on mica surfaces: A reciprocal space approach', 2009, *J. Polym. Sci. Part B: Polym. Phys.* (under review)

3) Lages, S.; **Sinha, P.**; Goerigk, G.; Kiriy, A.; Stamm, M.; Huber, K. 'Formation of Pb^{2+} induced intermediate necklace structures of short polyacrylate chains' (manuscript under preparation)

4) **Sinha, P.**; Kiriy, A.; Stamm, M.; Messina, R.; Löwen, H. 'Pinning, stretching and coiling behavior of polystyrene sulfonates under shear flow: AFM investigations and computer simulations' (manuscript under preparation)

Conferences

1) **Talk-** Intermediate states in bivalent ion induced shrinking of polyacrylate coils in solution and on surfaces: Sr^{2+}, Pb^{2+} and Ca^{2+}
Deutsche Physikalische Gesellschaft (DPG) spring meeting, 2009, Dresden, Germany.

2) **Talk-** Evaluating form factors in solution and on surfaces
9th European Summer School on Scattering Methods applied to Soft Condensed Matter, 2008, Bombannes, Gironde, France.

3) **Poster-** Entropically driven coil collapse in polyacrylate-Ca^{2+} systems: Comparative study using SANS and AFM
Deutsche Physikalische Gesellschaft (DPG) spring meeting, 2009, Dresden, Germany.

Versicherung

Hiermit versichere ich, dass ich die vorliegende Arbeit ohne unzulässige Hilfe Dritter und ohne Benutzung anderer als der angegebenen Hilfsmittel angefertigt habe; die aus fremden Quellen direkt oder indirekt übernommenen Gedanken sind als solche kenntlich gemacht. Die Arbeit wurde bisher weder im Inland noch im Ausland in gleicher oder ähnlicher Form einer anderen Prüfungsbehörde vorgelegt. Die vorliegende Arbeit wurde unter der wissenschaftlichen Betreuung von Prof. Dr. Manfred Stamm an dem Leibniz-Institut für Polymerforschung Dresden angefertigt. Keine frühere erfolglose Promotionsverfahren statt gefunden haben. Ich erkenne die Promotionsordnung der Technischen Universität Dresden der Fakultät Mathematik und Naturwissenschaft vom 16.04.2003 an.

Prashant Sinha

Dresden, Deutschland.